Report Documentation Page		Form Approved OMB No. 0704-0188

Public reporting burden for the collection of information is estimated to average 1 hour per response, including the time for reviewing instructions, searching existing data sources, gathering and maintaining the data needed, and completing and reviewing the collection of information. Send comments regarding this burden estimate or any other aspect of this collection of information, including suggestions for reducing this burden, to Washington Headquarters Services, Directorate for Information Operations and Reports, 1215 Jefferson Davis Highway, Suite 1204, Arlington VA 22202-4302. Respondents should be aware that notwithstanding any other provision of law, no person shall be subject to a penalty for failing to comply with a collection of information if it does not display a currently valid OMB control number.

1. REPORT DATE **1999**	2. REPORT TYPE	3. DATES COVERED **00-00-1999 to 00-00-1999**
4. TITLE AND SUBTITLE **Magnetomechanical Behavior of Terfenol-D Particulate Composites**		5a. CONTRACT NUMBER
		5b. GRANT NUMBER
		5c. PROGRAM ELEMENT NUMBER
6. AUTHOR(S)		5d. PROJECT NUMBER
		5e. TASK NUMBER
		5f. WORK UNIT NUMBER
7. PERFORMING ORGANIZATION NAME(S) AND ADDRESS(ES) **University of Illinois at Urbana-Champaign,Theoretical and Applied Mechanics,405 N. Mathews M/C 251 ,Urbana,IL,61801**		8. PERFORMING ORGANIZATION REPORT NUMBER
9. SPONSORING/MONITORING AGENCY NAME(S) AND ADDRESS(ES)		10. SPONSOR/MONITOR'S ACRONYM(S)
		11. SPONSOR/MONITOR'S REPORT NUMBER(S)

12. DISTRIBUTION/AVAILABILITY STATEMENT **Approved for public release; distribution unlimited**

13. SUPPLEMENTARY NOTES

14. ABSTRACT

15. SUBJECT TERMS

16. SECURITY CLASSIFICATION OF:			17. LIMITATION OF ABSTRACT	18. NUMBER OF PAGES	19a. NAME OF RESPONSIBLE PERSON
a. REPORT **unclassified**	b. ABSTRACT **unclassified**	c. THIS PAGE **unclassified**	**Same as Report (SAR)**	**156**	

MAGNETOMECHANICAL BEHAVIOR OF TERFENOL-D PARTICULATE COMPOSITES

BY

JENNIFER ANN HOMMEMA

B.S., University of Illinois, 1997

THESIS

Submitted in partial fulfillment of the requirements
for the degree of Master of Science in Theoretical and Applied Mechanics
in the Graduate College of the
University of Illinois at Urbana-Champaign, 1999

Urbana, Illinois

Acknowledgments

Table of Contents

List of Tables

List of Figures

ix

Chapter 1

Introduction

1.1 Structural health monitoring of composite materials

A structural composite is defined as a material consisting of two or more phases on a macroscopic scale. The properties of the composite material are improved from the properties of the constituent phases acting alone. Typically, a structural composite consists of a reinforcement phase, a matrix phase, and an interphase or interface. The reinforcement phase is usually stiffer and stronger and takes the form of particulates or fibers. The matrix could be a ceramic, a metal, or a polymer. One of the first documented uses of structural composites is straw–reinforced clay bricks in ancient Egypt [6]*.

More recently, in the twentieth century, structural polymer composites have found many applications in the aerospace, automotive, sporting goods, and medical industries. Structural polymer composites have high specific stiffness (modulus to density ratio) and high specific strength (strength to density ratio). Some polymer composites also have increased corrosion resistance, wear resistance, thermal stability, and/or fatigue life. Advanced manufacturing methods such as autoclave molding, filament winding, pultrusion, and resin transfer molding allow structural composites to be designed with complex geometries. One of the

---

*References are listed alphabetically by author at the end of the thesis, beginning on page 140.

disadvantages of polymer composites is their failure process. The most common matrices are thermosetting polymers such as epoxies and polyesters, which fail in a brittle manner. Brittle failure of structural polymer composites is often catastrophic and occurs with little warning. For example, when a multidirectional laminate experiences impact loading, delaminations and other damage occur beneath the surface of the composite. This damage can not be detected by visual inspection alone and could lead to unexpected failure [6].

New techniques are necessary to monitor the health of a structure. These techniques should detect damage and prevent failure, or at least anticipate it. There are many different ways to achieve structural health monitoring through nondestructive evaluation including visual inspection, ultrasonic C-scan, and x-ray radiography. A recently developed technique of interest for polymer composites is tagging, in which a smart material phase is added to the matrix of the composite as shown in Figure 1.1. The presence of the smart material allows the composite to be self-assessing. A self-assessing material is able to interrogate and assess its own state of health. The tagging phase could take the form of thin films, wires, or particles. Common classes of smart materials which could be used include piezoelectric, magnetostrictive, and shape-memory alloy.

Magnetostrictive tagging offers unique capabilities for self-assessment. Utilizing the so-called *inverse* effect, a magnetostrictive material develops or changes its magnetic field under the application of stresses. Thus, by measuring the magnetic fields surrounding a magnetostrictive material, a measure of the stresses on that material is obtained. If the stresses are elevated due to the presence of damage, the magnetic field will also be elevated. Self-assessment is achieved by incorporating magnetostrictive tags into a structural material and monitoring the magnetic field emanating from the material.

This thesis investigates the magnetomechanical behavior of Terfenol-D particulate composites. Terfenol-D is a magnetostrictive material. By grinding the material into small particles, the powder is easily mixed into a polymer resin during manufacture of the composite. Once the resin is cured, the composite material has self-assessing capabilities since

the magnetostrictive particles respond to changes in the stress state.

1.2   Magnetostriction

Magnetostriction is defined as the deformation of any substance due to the presence of magnetic fields. It occurs in ferromagnetic materials including iron, cobalt, and nickel and was first documented by Joule in 1842 in iron bars. The two types of magnetostriction are volume magnetostriction and Joule magnetostriction. Volume magnetostriction is an isotropic volume effect, while Joule magnetostriction is anisotropic. Referring to Figure 1.2, consider a magnetostrictive sphere in the absence of any magnetic field ($\mathbf{H}$). When a magnetic field is applied, the sphere elongates into an ellipsoid with the symmetry axis along the direction of the applied magnetic field. This process is called Joule magnetostriction. There is a limit to this induced strain, which is known as the saturation magnetostriction. The thought experiment above demonstrates the direct effect of magnetostriction, but an inverse effect also exists. In the inverse effect, mechanical stresses ($\mathbf{T}$) on a body affect its magnetic state [32]. These two effects are shown in Figure 1.2, where the top spheres show the mechanical deformation and the lower spheres show the magnetic orientation, as represented by arrows.

1.2.1   Ferromagnetic "Weiss" domain theory

Pierre Weiss defined a domain in a ferromagnetic material as a volume in which all the elementary magnetic moments are aligned in the same direction [32]. The moments are aligned with one of the "easy axes", which are defined by the crystal structure. Domains are separated by Bloch walls in which the magnetization rotates from one easy axis to another easy axis. In a demagnetized body, the net magnetization is zero as shown in (a) of Figure 1.3. The domains are labeled D_i and each has an arrow representing the direction of the magnetic moments or the magnetization. When a magnetic field is applied to the domains, several

3

different domain motions can occur. First, the domains rotate 180° to align with the applied field as shown in (b). Next, 90° domain wall displacement occurs. In each of these processes, Bloch walls disappear when the domains merge. Finally, the magnetization will rotate to the same direction as the applied field [32].

1.2.2 Piezomagnetism

In general, magnetostriction is a second-order, nonlinear effect, but it can be treated as a first-order, linear effect over a certain range of operation [22]. The linear magnetostrictive effect is called piezomagnetism and is described by the equations,

$$S_{ij} = s_{ijkl}^H T_{kl} + d_{kij} H_k \tag{1.1a}$$

$$B_i = d_{ikl}^H T_{kl} + \mu_{ik}^T H_k \tag{1.1b}$$

where T_{ij} is the stress tensor, S_{ij} is the strain tensor, B_i is the magnetic flux vector, and H_i is the magnetic field vector. The tensor, d_{ijk}, is composed of material properties known as piezomagnetic coefficients. The tensor equations can be simplified to the matrix equation

$$
\begin{bmatrix} S_1 \\ S_2 \\ S_3 \\ S_4 \\ S_5 \\ S_6 \\ B_1 \\ B_2 \\ B_3 \end{bmatrix} =
\begin{bmatrix}
s_{11}^H & s_{12}^H & s_{13}^H & s_{14}^H & s_{15}^H & s_{16}^H & d_{11} & d_{21} & d_{31} \\
s_{21}^H & s_{22}^H & s_{23}^H & s_{24}^H & s_{25}^H & s_{26}^H & d_{12} & d_{22} & d_{32} \\
s_{31}^H & s_{32}^H & s_{33}^H & s_{34}^H & s_{35}^H & s_{36}^H & d_{13} & d_{23} & d_{33} \\
s_{41}^H & s_{42}^H & s_{43}^H & s_{44}^H & s_{45}^H & s_{46}^H & d_{14} & d_{24} & d_{34} \\
s_{51}^H & s_{52}^H & s_{53}^H & s_{54}^H & s_{55}^H & s_{56}^H & d_{15} & d_{25} & d_{35} \\
s_{61}^H & s_{62}^H & s_{63}^H & s_{64}^H & s_{65}^H & s_{66}^H & d_{16} & d_{26} & d_{36} \\
d_{11} & d_{12} & d_{13} & d_{14} & d_{15} & d_{16} & \mu_{11}^T & \mu_{12}^T & \mu_{13}^T \\
d_{21} & d_{22} & d_{13} & d_{24} & d_{25} & d_{26} & \mu_{21}^T & \mu_{22}^T & \mu_{23}^T \\
d_{31} & d_{32} & d_{13} & d_{34} & d_{35} & d_{36} & \mu_{31}^T & \mu_{32}^T & \mu_{33}^T
\end{bmatrix}
\begin{bmatrix} T_1 \\ T_2 \\ T_3 \\ T_4 \\ T_5 \\ T_6 \\ H_1 \\ H_2 \\ H_3 \end{bmatrix} \tag{1.2}
$$

via the simplifications summarized in Table 1.1.

4

Table 1.1: Simplification of tensor notation to matrix form of piezomagnetic equations.

ij and kl (tensor indices)	11	22	33	23 and 32	31 and 13	12 and 21
p and q (matrix form)	1	2	3	4	5	6

1.2.3 Direct effect

The direct effect is very well documented in the literature. Much research has been conducted to optimize the properties of Terfenol-D for magnetostrictive transducers and actuators. Most of this transducer research uses one-dimensional piezomagnetic theory. The piezomagnetic coefficient, d_{33}, is reported to have a value between 1.0×10^{-8} and 2.5×10^{-8} m/A by Moffett *et al.* [20]. A similar transducer experiment yielded lower d_{33} values between 2.5×10^{-9} and 5.5×10^{-9} m/A [7].

1.2.4 Inverse effect

The inverse effect of magnetostriction is sometimes referred to as the Villari effect [32]. There is significantly less published work on the inverse effect than the direct effect. The Villari effect in ferrites has been proposed as a possible means of measuring stresses [1]. Steel and nickel samples were externally stressed, yielding changes in the magnetic field measured with a Permalloy magnetoresistor [17, 18].

Within the large published accounts of the direct effect, there is some discussion of the inverse effect in a very specialized application. Terfenol-D actuators are compressively prestressed before application of the driving magnetic field. This prestress increases the saturation magnetostriction and the piezomagnetic coefficient in the direction of the applied magnetic field [5]. It is hypothesized that the compressive prestress rotates the domains away from their initial poling axis along the length axis of the actuator rod. Then, the application of the magnetic field can rotate more domains into the direction of the field along the length axis, resulting in a higher magnetostrictive strain [32].

1.3 Terfenol-D

Terfenol-D is a ternary alloy of terbium, dysprosium, and iron with the chemical formula $Tb_{0.3}Dy_{0.7}Fe_{2.0}$. It is called a "giant magnetostrictive", since it is capable of a large saturation magnetostrictive strain. The saturation magnetostriction of Terfenol-D, as defined in Section 1.2 and denoted by λ_s, has been measured to have a value as high as 2.4×10^{-3}. This magnetostrictive strain is the largest known room temperature saturation magnetostriction [32]. Values for the saturation magnetostriction reported by the material manufacturer, Etrema Products, are between 1.5×10^{-3} and 2.0×10^{-3} [8]. For rods grown by the Bridgman technique and the free-standing-zone melt technique, λ_s values were 1.6×10^{-3} and 2.0×10^{-3}, respectively. For a single-crystal rod, λ_s was 2.4×10^{-3} [11].

The reported material properties of Terfenol-D vary widely. This variation is in part due to the dependence of the properties on the crystal structure and the magnetic and stress conditions under which the properties are measured [32]. For three Terfenol-D rods grown by the Bridgman, the free-standing-zone melt, and the single-crystal techniques, the Young's modulus was consistently 100 GPa [11]. Varying the magnitude of the magnetic flux on a rod from 0 to 4.5 kG caused the Young's modulus to increase from 44 GPa to 110 GPa [4]. In an article on a magnetostrictive finite element analysis, Kannan and Dasgupta selected 30 GPa and 0.444 for the Young's modulus and Poisson ratio, respectively [19]. Values for tensile and compressive strength are 28 and -700 MPa, respectively [32].

The piezoelectric properties of Terfenol-D have been measured for the direct effect with a one-dimensional model; therefore, only the d_{33} value is found in the literature. In a review article, reported d_{33} values were as small as 10×10^{-9} m/A or as large as 90×10^{-9} m/A depending on the magnitude of the magnetic field and prestress used in the actuator experiment [14]. For a Bridgman technique rod, d_{33} was 24×10^{-9} m/A and for a free-standing-zone melt, d_{33} was 57×10^{-9} m/A [32]. Variation of compressive prestress and magnetic bias field showed d_{33} decreasing from 25×10^{-9} to 4×10^{-9} m/A as the bias field

and prestress were increased [20].

The values for permeability of Terfenol-D are reported as relative values, where

$$\mu_{ij}^{\text{rel}} = \frac{\mu_{ij}}{\mu_0} \tag{1.3}$$

where μ_0 is the permeability of free space. A range of 4 to 17 was measured for the relative permeability as a function of frequency [9]. Etrema Products reported relative permeability values between 5 and 10 [32]. By variation of compressive prestress and magnetic bias field, relative permeability measured for a Terfenol-D rod was between 4 and 15, with the highest value corresponding to the lowest prestress and lowest magnetic bias field [20].

1.4 Magnetostrictive composites

Magnetostrictive composites have been studied and used in direct effect applications [30, 13]. Rod-shaped particulate composites with a nonmetallic insulating matrix were manufactured with 70–80% volume fraction of Terfenol-D [30]. In a transducer experiment, the rod was placed in a solenoid that provided a driving magnetic field. Strain gages were used to measure longitudinal strain and an induction pick-up coil measured the magnetization changes. One type of composite was isotropic, while the second type was anisotropic because the particles had been magnetically oriented. The anisotropic rods performed slightly better than the isotropic rods. The saturation magnetostrictions measured for the rods were approximately 40% of the saturation magnetostriction of pure Terfenol-D. The piezomagnetic constant, d_{33}, was measured to be between 3×10^{-9} and 6×10^{-9} m/A [30].

Using a similar experimental procedure, Hudson *et al.* investigated the dependence of magnetostrictive composite properties on particle size and volume fraction. Composites consisted of an epoxy matrix and particles which ranged in size from 106–710 μm. Only three volume fractions were tested: 55%, 62% and 70%. The first conclusion was that the

magnetomechanical coupling coefficient was independent of particle size and volume fraction. Elastic moduli were independent of particle size but dependent on volume fraction [13].

Jolly *et al.* studied the magnetostrictive direct effect with an application to elastomer composites [15]. Carbonyl iron particles were embedded in a polymer matrix. The particles were exposed to a strong magnetic field during cure which caused the particle to migrate into particle chains parallel with the applied field. When the elastomer composite was cured, it was tested in a double lap shear to determine how much the stiffness changed with variation of an applied magnetic field [15]. Metal matrix magnetostrictive composites were successfully fabricated by Pinkerton *et al.* [25]. The composites consisted of a matrix of either iron or aluminum and a 50% volume fraction of $SmFe_2$ ribbons. These composites exhibited large saturation magnetostrictive strains and good mechanical integrity.

1.5 Terfenol-D particulate composites

For the purpose of structural health monitoring, Terfenol-D particulate composites were first proposed by Rogers *et al.* [29]. These researchers were able to demonstrate elevated magnetic fields at the location of a delamination in a Terfenol-D tagged epoxy composite. They also investigated the magnetic fields measured in a composite consisting only of Terfenol-D and epoxy. A similar report was made by Jones and Liang [16]. Their paper also presented results showing that embedded Terfenol-D particles could be used to locate a delamination in a composite. Unfortunately, no information was included as to particle size, distribution, or manufacture of the specimen.

An initial study was conducted by White and Albers to determine the feasibility of using magnetostrictive Terfenol-D tags for structural health monitoring [36]. The chaining phenomenon documented by Jolly *et al.* [15] was observed in the polymer composites of White and Albers. They documented a definite, repeatable, measurable magnetic response under tensile loading for several different composites. They also showed that elevated magnetic

signals were seen at the site of a delamination [36].

This initial study was expanded by Brouwers [2], who conducted extensive mechanical testing on Terfenol-D/polyester composites with and without glass fiber reinforcement. His experimental work used a Hall probe to detect changes in magnetic flux as a composite was loaded in tension. He demonstrated that the application of a magnetic field during cure caused the chaining phenomenon and increased the magnetic response of the composites. He also introduced the concept of "magnetic annealing" to increase the magnetic response of the composites. Damage detection tests for the Terfenol-D/polyester composites were quite successful. Magnetic flux levels were elevated at the edge of a hole and also at the tip of a square notch. Similar tests on Terfenol-D/glass/polyester composites were inconclusive. Unfortunately, only a single component of the magnetic flux was reported in this work. Three-dimensional measurements of the magnetic flux were obtained later and reported [35]. The most significant result in this latter work is that the largest maximum magnetic response was in the direction of the curing and annealing magnetic fluxes. These responses were the largest ever reported for Terfenol-D particulate composites. The piezomagnetic coefficients measured were d_{33} equal to 7.97×10^{-11} m/A and d_{31} equal to 2.49×10^{-11} m/A [34]. Overviews of these magnetostrictive tagging results as they apply to structural health monitoring are given by Quattrone *et al.* and White [27, 33].

1.6 Project overview

The research in this thesis is divided into three distinct areas. First, the magnetomechanical behavior of pure Terfenol-D and Terfenol-D composites is studied in uniaxial compression in Chapter 2. The Terfenol-D composites tested consist of a polyester matrix and 2.2% volume fraction Terfenol-D particulates. The three-dimensional magnetic response is measured over the gage length of the specimens in uniaxial compression. Also, the piezomagnetic coefficients are predicted for the pure Terfenol-D specimen and the Terfenol-D composites. Cyclic testing

9

is presented, showing the stability of the response after multiple loading and unloading cycles. Different combinations of curing magnetic flux and annealing magnetic flux are compared. In Chapter 3, a modified Eshelby model is used to predict the residual stresses that develop during the manufacturing process of the Terfenol-D composites. Finally, a finite element analysis of a Terfenol-D rod embedded in a polyester cylinder is presented in Chapter 4.

composite material

+

smart material particulates

tagged composite material
with self-assessing abilities
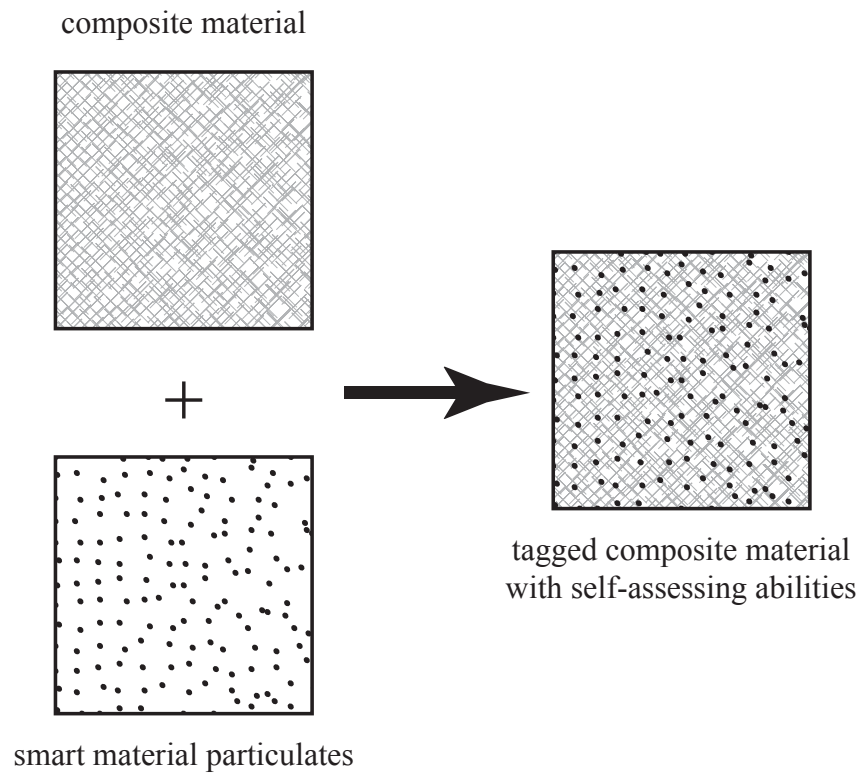
Figure 1.1: Schematic of tagging concept with magnetostrictive particulates.

$\mathbf{H}$

$\mathbf{T}$

$\mathbf{H} = 0$

$\mathbf{T} = 0$

Direct Effect (apply $\mathbf{H}$)

Inverse Effect (apply $\mathbf{T}$)
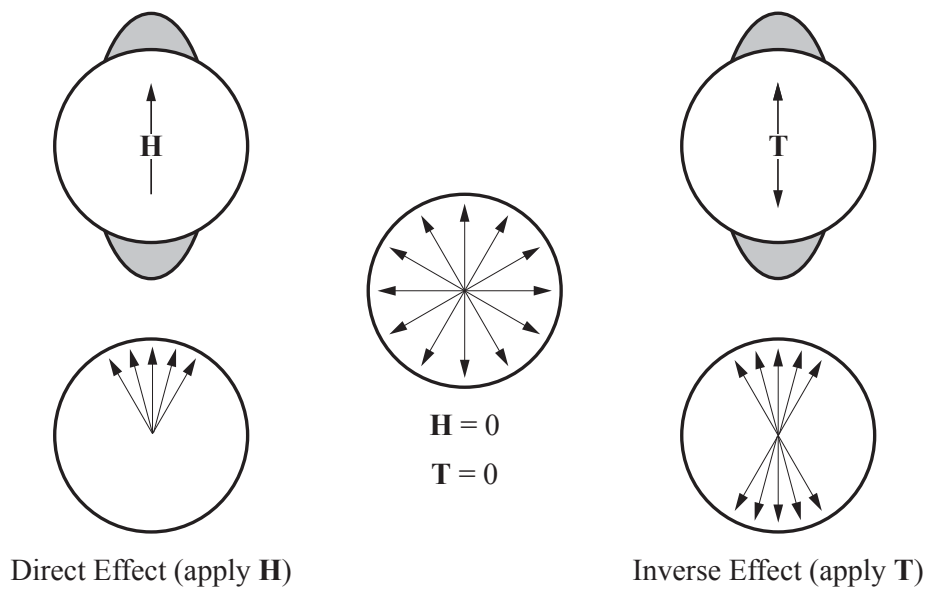
Figure 1.2: Direct and inverse effects of magnetostriction.
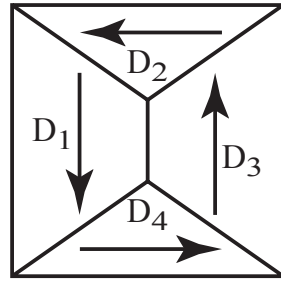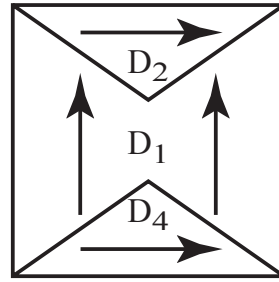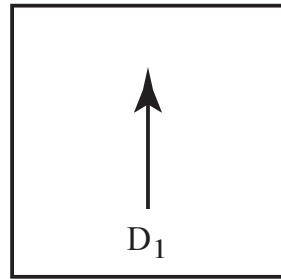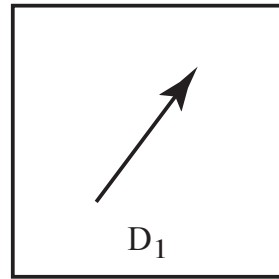
Figure 1.3: Domain evolution under applied magnetic field [32].

Chapter 2

Compression testing

2.1 Specimen manufacture

2.1.1 Preparation of Terfenol-D

One pure Terfenol-D specimen ($12.5 \times 12.5 \times 25$ mm) was purchased from Etrema Products, Inc. (Ames, IA). The specimen was machined from a near-single crystal rod with its growth axis in the 1-direction as shown in Figure 2.1.

To produce the Terfenol-D powder, amorphous Terfenol-D fingers were purchased from Etrema Products, Inc. (Ames, IA). These fingers were ground in an argon environment and screened to 30 mesh. Once the particles were all 30 mesh or smaller, they were stored under argon and sent to Union Process, Inc. (Akron, OH). At Union Process, the particles were ball milled under argon. Machine cutting oil was used to prevent the particles from sticking together. Particles that were milled without oil clumped together and exhibited less magnetostrictive behavior when tested compared with particles milled under oil; therefore only particles milled in oil were used for the composites in this study. The particles in oil were shipped back in an argon environment. Vacuum filtration with a silica frit was used to separate the powder from the oil. The procedure was executed under argon and hexane was used to wash the particles. The powder was repeatedly rinsed with hexane until no oil was present on the particles.

2.1.2 Terfenol-D composite manufacture

The Terfenol-D composites in this study consisted of a polyester matrix (Polylite 31610-05, Reichold Chemicals, Research Triangle Park, NC) and Terfenol-D particles prepared by the procedure described in Section 2.1.1. The first step of fabrication was to add two catalysts, cobalt naphthenate (0.1% by wt. resin) and N-N dimenthylaniline (0.1% by wt. resin), and an aerator, Byk-A 501 (0.1% by wt. resin), to the polyester resin. After each of these was added, the polyester was mixed and degassed in a vacuum oven. Next, 15% weight fraction (2.2% volume fraction) of Terfenol-D particles was mixed into the polyester resin and degassed. To initiate polymerization, methyl ethyl ketone peroxide (1.0% by wt. resin) was added. After the final mixing and degassing step, the resin mixture was poured into a silicon rubber mold. The mold was placed between two permanent magnets (Adams Magnetic Products Co., Melrose Park, IL) or in an electromagnet (Ogallala Electronics, Ogallala, NE) and allowed to cure at room temperature for 48 hours. The composite specimens were $12.5 \times 12.5 \times 25$ mm as shown in Figure 2.1.

2.1.3 Magnetic flux during cure and magnetic anneal after cure

Applying a magnetic flux to a composite specimen during cure causes the Terfenol-D particles to orient into chains in the direction of the flux. Each particle is made up of multiple magnetic domains of different orientation. The magnetic flux causes the particles to rotate, such that the majority of the magnetic domains in a particle are aligned with the magnetic flux, and agglomerate into chains. When the polyester gels, the particles are locked into this chained configuration. The composite specimens were either cured with a magnetic flux through their length or a magnetic flux through their width resulting in chaining in the direction of the applied magnetic flux as shown in Figures 2.2 and 2.3.

Applying a magnetic flux after the specimen is fully cured will be referred to in this thesis as "magnetic annealing". Magnetic annealing partially orients the magnetic domains

14

in the direction of the applied flux, but cannot rotate the entire particle, as the particles are locked into their position by the solidified polyester matrix. The specimens were magnetically annealed for 20 seconds either in the electromagnet or between the two permanent magnets and then tested immediately after the magnetic annealing.

2.2   Experimental procedure

All of the specimens were tested in uniaxial compression on an Instron 8500 testing machine (Canton, MA). LabView^{TM} was used to acquire the data from the load cell, linear variable displacement transducer (crosshead position), and Gaussmeter (magnetic flux). Loading and unloading was at a constant rate of 0.01 kN/s for each test. The specimen was centered on the bottom compression platen and then an initial compressive load of 1% of the maximum load was applied to align the specimen before commencing the test. A diagram of the experimental setup is shown in Figure 2.4.

The compression platens were designed specifically for this experiment. They are made entirely of 304 austenitic stainless steel, which is nonmagnetic. The total length of each fixture is 5 inches, to separate the specimen from the iron screws of the Instron machine. The bottom platen has a spherical seat which helps to eliminate bending and off-axis loading when the specimen is centered carefully.

The magnetic response was measured with a Hall probe and Gaussmeter (Model 450, Lake Shore Cryotronics, Westerville, OH). The Gaussmeter conditioned the signal from the Hall probe and output magnetic flux (**B**) readings. One limitation of the setup was that the Hall probe could measure only one direction of the magnetic flux at a time. To obtain all three components of the magnetic flux vector, the experiment had to be repeated three times. Due to the geometry of the probe as shown in Figure 2.5, the magnetic flux could not be measured at the same distance from the surface in all three directions. To measure a magnetic flux, the probe had to be oriented such that the magnetic flux went through the

sensing area (a circle of wire). For the B_3 measurement, the probe could be placed directly on the surface of the specimen and the sensing area was approximately half the probe thickness or 0.8 mm from the surface. For the B_1 and B_2 measurements, the probe sensing area was perpendicular to the surface and thus 3.8 mm from the surface.

2.3 Typical results and data reduction

For a typical test of a 2.2% Terfenol-D/polyester composite, one component of magnetic flux, B_i, is measured and plotted versus compressive stress as shown in Figure 2.6. The magnetic flux at zero load will be referred to as B_i^{init}. Since the loading response is more important than the unloading response, the change in magnetic flux from initial to maximum compressive stress is an important quantity and will be referred to as ΔB^{max}. In some instances, the magnetic flux values were zeroed by subtracting B_i^{init}. The magnetic flux is then referred to as the "zeroed magnetic flux" as shown in Figure 2.7.

For the composite specimens, a special nomenclature is used to denote the magnetic flux applied during cure, the annealing magnetic flux, and the loading direction. Each test on a specimen is labeled as follows: (a,b,c) where a = the direction of magnetic flux during cure, b = the direction of the annealing magnetic flux, and c = the loading direction. For example, a test with (3,3,1) indicates that both the magnetic flux during cure and the annealing magnetic flux were in the 3-direction while the loading was in the 1-direction. Further, the graph axis is labeled as to which component of magnetic flux (B_i) was measured in the experiment.

Since the measurements of B_1, B_2, and B_3 are taken at different distances from the surface of the specimen as discussed in Section 2.2, a study was conducted to determine the dependence of magnetic flux measurements on the distance of the probe sensing area from the surface of a specimen. A (3,3,1) Terfenol-D composite specimen was tested to a uniaxial compressive stress of -10 MPa and ΔB_3^{max} was measured at the midpoint of the specimen at

16

multiple distances up to 22 mm from the surface of the specimen. The annealing magnetic flux was -800 G for all tests. The results are shown in Figure 2.8. It is interesting to note that while the magnetic flux dropped quickly as the probe was moved away from the surface of the specimen, the magnetic flux did not exhibit a $1/d^3$ dependence. The magnetic flux of a magnetic dipole decays as $1/r^3$, so this trend was expected [10]. The dependence of the magnetic flux measurement on distance from the specimen has a detrimental effect on the results of all three-dimensional gage length characterizations, since the values of B_1 and B_2 were measured 3.8 mm from the surface while B_3 was measured 0.8 mm from the surface. The B_3 measurements will be larger in magnitude than the B_1 and B_2 measurements.

2.4 Gage length characterization

For the pure Terfenol-D specimen and the Terfenol-D composites, measurements of magnetic flux were taken over the gage length. The specimens were marked with a grid as shown in Figure 2.9. Then, magnetic flux measurements were taken along the middle of the specimen at 2 mm increments in the 1-direction along the front face perpendicular to the 3-direction. In some cases, the side face that is perpendicular to the -2-direction was used for measurements. Unless otherwise noted, magnetic flux was measured on the front face.

A typical result with the entire gage length compiled into one graph is shown in Figure 2.10. This graph shows the variations in initial magnetic flux as well as the shape and magnitude of the loading and unloading responses. To compare the magnetic response in a different way, the magnetic flux was zeroed by subtracting the magnetic flux at zero load, B_i^{init}, as shown in Figure 2.11. This subtraction process removes the ambient magnetic flux, B_i^{amb}, of the room as well as the initial magnetic flux from the specimen. To measure the ambient field, a polyester specimen (nonmagnetic) identical in geometry and size to the composite specimens was loaded into the grips and the three components of the magnetic flux along the gage length were measured. This ambient flux measurement procedure was

conducted before each day of testing, and a typical measurement is shown in Figure 2.12. When the specimen was loaded there was no change in the magnetic field. The standard deviation from the average magnetic flux was 0.001 G. The zeroed response indicates how much variation occurs in $\Delta B_i^{\max}$, but does not reveal the direction of the change. This information is important because it tells whether the number of magnetic domains in the direction of measurement is increasing or decreasing.

2.4.1 Pure Terfenol-D

The pure Terfenol-D specimen was tested with annealing magnetic flux in the 1-direction only. Annealing in any other direction was not possible as the specimen would rotate to align its length axis (1-direction) with the magnetic flux unless it was physically restrained from moving. The specimen was annealed with the permanent magnets at a magnetic flux of -800 G before each experiment. The specimen was loaded to -40 MPa and then unloaded. The results are included in Appendix A in Figures A.1–A.8. Measurements of B_2 were taken on both the front face and the side face. To compare the results, a plot of $\Delta B_i^{\max}$ versus gage length position is shown in Figure 2.13 for a uniaxial compressive stress of -40 MPa.

In Figure 2.13, the largest magnetic flux change that is constant across the gage length is $\Delta B_1^{\max}$. There is a slight decrease in the magnetic flux measurements that were taken closer to the ends of the specimen. This decrease is also seen clearly in Figure A.2. Initially, the values of B_1 are between 2 and 5 G, then the flux decreases during loading to approximately -0.6 G, which was the ambient magnetic flux, B_1^{amb}, measured on that day of testing. The majority of the decrease in magnetic flux is in the initial portion of the loading (up to -5 MPa). Then, the flux asymptotically approaches zero, indicating a saturation phenomenon. The loading curve behavior shows that the domains have rotated away from the 1-direction. At -40 MPa, the magnetic flux, B_1 is nearly zero denoting that very few domains remain in the 1-direction. In the unloading portion of the curve, no domains return to their original orientation as the B_1 values do not change appreciably. The same

18

type of saturation behavior is seen in the B_2 and B_3 responses. Most of the magnetic flux change is in the first 5 MPa of loading. After that change, the magnetic flux asymptotically approaches a value with very little change during unloading.

The changes in magnetic flux, $\Delta B_2^{\max}$ and $\Delta B_3^{\max}$, are not constant across the gage length like $\Delta B_1^{\max}$. Measurements on the front face (Figures A.3 and A.4) indicate that $\Delta B_2^{\max}$ is very small relative to the other components of magnetic flux, but on the side face (Figures A.5 and A.6), $\Delta B_2^{\max}$ is similar to $\Delta B_3^{\max}$ measured on the front face (Figures A.7 and A.8). These magnetic response values "fan" across the gage length with both curves passing through zero magnetic flux near the midpoint of the specimen. The difference in sign of the two responses can be explained by the orientation of the probe during measurement. If the response was measured in a cylindrical coordinate system where z was along the length of the specimen, the 2 and 3 axes would both correspond to the r-direction outward from the center of the specimen. In this coordinate system, the responses would be nearly identical as shown in Figure 2.14.

The "fanning phenomenon" can be explained by examining the magnetic flux lines of a uniformly magnetized cylinder shown in Figure 2.15. The Terfenol-D specimen has a nearly uniform magnetization initially. Most of the domains are oriented in the crystal growth direction and then the annealing magnetic flux orients even more domains in the 1-direction. The Terfenol-D specimen can be modeled by the uniformly magnetized cylinder shown in Figure 2.15. When the magnetic flux vector is decomposed into components at two different locations: one above the midpoint and one below the midpoint, the "fanning phenomenon" is observed. The B_1 values are the same above and below the midpoint, but the B_3 values are opposite.

2.4.2 Terfenol-D composites

Terfenol-D composites were created with two different magnetic flux orientations during cure. The curing magnetic flux was either through the thickness (3-direction) of the specimen, or

through the length (1-direction) of the specimen. The magnetic flux during cure produced composites with particle chains in the direction of the applied flux. The strength of the flux was -800 G for both orientations. Before each test, the specimen was annealed with a field of -800 G in the 1, 2, or 3-direction. The composites were then loaded to -10 MPa of uniaxial compressive stress and fully unloaded.

2.4.2.1   Terfenol-D composites with chaining in 1-direction

The gage length characterization results for a (1,1,1) Terfenol-D composite specimen are shown in Figures A.9–A.16. The same Terfenol-D composite specimen was also tested with an annealing magnetic flux in the 3-direction. These (1,3,1) Terfenol-D composite specimen results are given in Figures A.17–A.24. Similar to the pure Terfenol-D specimen tests, measurements of B_2 were taken on both the front face and the side face for both series of tests. To compare the magnetic response at maximum load, $\Delta B_i^{\max}$, versus gage length position is shown in Figures 2.16 and 2.17 for a uniaxial compressive stress of -10 MPa.

The magnetomechanical behavior of the (1,1,1) and (1,3,1) Terfenol-D composites is similar to the pure Terfenol-D specimen discussed in Section 2.4.1. The value of B_1 decreases toward zero during loading for both the composites and the pure specimen, but the magnitude of the magnetic response differs. The initial values of B_1 are smaller for the composites than the pure Terfenol-D specimen, indicating a difference in the number of domains. While the average $\Delta B_1^{\max}$ was -4.1 G for the pure Terfenol-D specimen, $\Delta B_1^{\max}$ averaged only -0.49 G for the (1,1,1) composite specimen. When the Terfenol-D composite was magnetically annealed in the 3-direction ((1,3,1) composite), the average $\Delta B_1^{\max}$ was even smaller, -0.17 G. This trend indicates that a larger B_1 response is seen when more domains are oriented along the compressive stress direction. The pure Terfenol-D specimen had the most magnetic domains that were oriented in the 1-direction due to both manufacturing and annealing. The composite had only a 2.2% volume fraction of Terfenol-D, so it had a smaller number of domains. When the domains were oriented in the 3-direction by annealing, the

response decreased even more because some of the domains were rotated away from the chaining direction to the direction of the annealing magnetic flux.

On the front face, $\Delta B_2^{\max}$ was nearly zero for both composites. The magnetic response in the 2 and 3-directions measured on the side and front faces, respectively, showed the "fanning" phenomenon seen in the pure Terfenol-D specimen. When the magnetic flux changes are converted to a cylindrical coordinate system, $\Delta B_2^{\max}$ and $\Delta B_3^{\max}$ are closer in magnitude for each composite as shown in Figure 2.18. An interesting detail is that when the specimen was annealed in the 3-direction, the curves shifted up and no longer passed through zero at the midpoint of the specimen as seen in the (1,1,1) composite and pure Terfenol-D specimens.

The unloading response of the composites does not indicate a saturation phenomenon. In Figure A.10 corresponding to the (1,1,1) composite, the final magnetic flux (B_1) after unloading is about 50% of $\Delta B_1^{\max}$. This type of change in magnetic flux upon unloading was seen in the (1,3,1) composite as well.

2.4.2.2 Terfenol-D composites with chaining in 3-direction

A Terfenol-D composite specimen was manufactured with a magnetic flux applied through its thickness (3-direction). This specimen was then tested under all three possible annealing directions. The gage length characterization results for the (3,1,1), (3,2,1) and (3,3,1) composite tests are given in Figures A.25–A.42.

The magnetomechanical behavior of the composite chained in the 3-direction varied greatly with the direction of the annealing magnetic flux. When the specimen was annealed in the 1-direction, as shown in Figure 2.19, the magnetic response was quite similar to the specimens discussed in Sections 2.4.1 and 2.4.2.1. The average value of $\Delta B_1^{\max}$, -0.078 G, for the (3,1,1) specimen was lower than the corresponding values for both the pure Terfenol-D specimen and the composite chained in the 1-direction. This decrease in magnitude is due to the initial alignment of domains in the 3-direction. Even with the annealing magnetic

21

flux in the 1-direction, not all of the domains are rotated to the 1-direction. The final two similarities are that one, the fanning phenomenon occurred in the B_3 response and two, $\Delta B_2^{\max}$ was approximately zero.

For both the (3,2,1) and the (3,3,1) Terfenol-D composites, the maximum magnetic flux change was in the direction of the annealing field as shown in Figures 2.20 and 2.21. The value of $\Delta B_3^{\max}$ was 0.42 G for the (3,3,1) specimen, while $\Delta B_2^{\max}$ was -0.096 G for the (3,2,1) specimen. The (3,3,1) response was the largest of all the specimens chained in the 3-direction. This behavior is similar to the specimens chained in the 1-direction. The responses are highest when the direction of chaining, annealing, and measurement is the same. This observation is further supported by swithcing the annealing magnetic flux from the 3-direction to the 2-direction and seeing the average $\Delta B_3^{\max}$ drop an order of magnitude from 0.42 G to 0.040 G.

The unloading responses of the specimen chained in the 3-direction were different for each annealing direction as well. In the (3,1,1) specimen, saturation did not occur and the final magnetic flux, B_1, was 75% of $\Delta B_1^{\max}$. Saturation did not appear to occur in the (3,2,1) or (3,3,1) specimens either, but each had a different unloading response. The final magnetic flux, B_2 of the (3,2,1) specimen was identical to $\Delta B_2^{\max}$ as seen in Figure A.34. In contrast, the final magnetic flux, B_3, of the (3,3,1) specimen was actually 20% higher than $\Delta B_3^{\max}$.

2.4.3 Determination of piezomagnetic coefficients

When magnetostriction is modeled as a first-order effect, it is called piezomagnetism, which is discussed in depth in Section 1.2.2. The governing equation for the compression experiments is

$$B_i = d_{ij}\sigma_j + \mu_{ij}^{\sigma}H_j \tag{2.1}$$

where B_i denotes the magnetic flux, σ_j denotes the stresses, and d_{ij} denotes the piezomagnetic coefficients. For the compression experiment, there are no shear stresses and no applied

magnetic fields, which simplifies the governing equation.

To determine the piezomagnetic coefficients of the compression specimens studied, the gage length results need to be transformed to the coordinate system used in the literature, where the poling or magnetization axis is always denoted 3. The Terfenol-D specimen has a magnetization axis along its length corresponding to its crystal growth axis. For the Terfenol-D composites, the direction of the curing field is designated as the poling axis. With these designations, there are two different cases to consider. In the first case, corresponding to the pure Terfenol-D rod and the (1,*,1) class of composites, the poling axis (3) is along the length of the specimen and the stress is also in this 3-direction. In the second case, corresponding to the (3,*,1) composites, the poling axis is perpendicular to the loading axis. Both of these geometries are shown in Figure 2.22.

In the Class I experiments, the only nonzero stress is σ_3. The magnetic flux components, given in the coordinate system used by the literature, are

$$B_1 = d_{13}\sigma_3 \tag{2.2a}$$

$$B_2 = d_{23}\sigma_3 \tag{2.2b}$$

$$B_3 = d_{33}\sigma_3 \tag{2.2c}$$

In the Class II experiments, the only nonzero stress is σ_1. The magnetic flux components, given in the coordinate system used by the literature, are

$$B_1 = d_{11}\sigma_1 \tag{2.3a}$$

$$B_2 = d_{21}\sigma_1 \tag{2.3b}$$

$$B_3 = d_{31}\sigma_1 \tag{2.3c}$$

The numerical values for the piezomagnetic coefficients were determined by plotting the zeroed magnetic flux versus stress for the loading portion of an experiment. The response

over the entire gage length was used in the linear curve fit. In the experiments where the magnetic flux exhibited the "fanning" phenomenon over the gage length, the average response was nearly zero, so no piezomagnetic coefficients were calculated.

2.4.3.1 Terfenol-D

The magnetic poling axis of the Terfenol-D specimen is along the length of the specimen since the specimen has a crystal growth axis along the length and the annealing magnetic flux was also along the length, so the geometry is Class I of Figure 2.22. The experimental data used for the curve fit are the initial part (up to -2.0 MPa) of the gage length characterization in Figure A.2. The d_{33} value, 1.48×10^{-10} m/A, is lower by two orders of magnitude than the d_{33} values reported for the direct effect in Section 1.2.3.

2.4.3.2 Terfenol-D composites

There were two types of composites tested: those poled in the direction of stress (Class I) and those poled perpendicular to the stress (Class II) by curing with a magnetic flux strength of 800 G. Within these two classes, the direction of the annealing field was varied, but its magnitude was always 800 G. Only the magnetic responses that were nearly constant across the gage length were fit to the piezomagnetic model. These gage length loading responses for the (1,1,1) and (1,3,1) specimens are presented in Figures 2.24 and 2.25 with the appropriate model predictions. Similarly, the (3,1,1), (3,2,1), and (3,3,1) specimen results are given in Figures 2.26, 2.27, and 2.28, respectively.

Table 2.1 gives a summary of the piezomagnetic coefficients determined for all of the Terfenol-D composites. The largest coefficient is $d_{33} = 7.86 \times 10^{-12}$ m/A for the (1,1,1) composite. When the annealing is perpendicular to the curing direction (the (1,3,1) composite), the value of d_{33} decreases by almost 80%. Also, a magnetic flux in the new annealing direction is measured and yields another piezomagnetic coefficient, d_{13}, which is even smaller and negative.

Table 2.1: Comparison of piezomagnetic coefficients for the different Terfenol-D composites discussed in Sections 2.4.2.1 and 2.4.2.2.

Type of composite	Geometry class	Piezomagnetic coefficients (m/A)
(1,1,1)	I	$d_{33} = 7.86 \times 10^{-12}$
(1,3,1)	I	$d_{33} = 1.73 \times 10^{-12}$ and $d_{13} = -5.48 \times 10^{-13}$
(3,1,1)	II	$d_{11} = 8.37 \times 10^{-13}$
(3,2,1)	II	$d_{31} = -4.73 \times 10^{-13}$ and $d_{21} = 1.07 \times 10^{-12}$
(3,3,1)	II	$d_{31} = -4.50 \times 10^{-12}$

The largest coefficient for the Class II composites is not as large as d_{33} for the (1,1,1) Terfenol-D composite, but it does correspond to the specimen where the curing and annealing directions are the same. The largest Class II piezomagnetic coefficient is d_{31} with a value of -4.50×10^{-12} m/A for the (3,3,1) composite. Similar to Class I phenomenon, when the annealing direction is perpendicular to the curing direction, the piezomagnetic coefficient is decreased in size and new additional piezomagnetic coefficients are measured.

2.5   Effect of magnetic flux on cyclic response

To study the effects of the magnitude of the curing and annealing magnetic fluxes on the Terfenol-D composites, specimens were manufactured with a curing flux of -2600 G using an electromagnet. One type of specimen was chained through its thickness and denoted (1,*,1) and one type was cured through its length and denoted (3,*,1). These composites were not tested for gage length characterization, but rather for cyclic response. Terfenol-D composites created with a curing magnetic flux of -800 G were also tested for cyclic response.

To characterize the cyclic response, a specimen was annealed in its chaining direction before testing in uniaxial compression. For this "cycle 1", the specimen was loaded to -10 MPa and then completely unloaded. For all following cycles, the loading regimen was the same, but the specimen was not annealed before testing. The magnetic flux was measured in the chaining direction at the midpoint of the front face for each test. A typical cyclic

response is shown in Figures 2.29 and 2.30. The graphs show that the initial cycle is different from all following cycles. There is negligible difference between the third cycle and the fiftieth cycle, so as few as 3 cycles were necessary to observe a stable response.

Results for the cyclic response of (1,1,1) Terfenol-D composites are shown in Figures B.1–B.8. Similar results for (3,3,1) Terfenol-D composites are given in Figures B.9–B.14. The curing flux and annealing flux were either −800 G or −2600 G for each test. One interesting trend in all the plots of nonzeroed magnetic flux is that the unloading response of cycle 1 is the same as the loading response of the following cycle. Then, the unloading of that cycle traces back the same unloading response as cycle 1. This is repeated in all later cycles, there is little difference between any cycles after the first. The trend shows that the annealing field aligns some domains in the direction of chaining, but these domains do not return to the chaining direction upon unloading. After the first cycle, the domains that were locked into position by the curing flux are solely responsible for the measured magnetic response. Even without any annealing, a repeatable measurable response is seen. The nonannealed response is smaller than the first cycle response with an annealing magnetic flux.

By varying the magnitude of the curing and annealing magnetic fluxes, the initial cycle response and final cycle response can be changed. Table 2.2 shows a comparison of $\Delta B_1^{\max}$ for (1,1,1) Terfenol-D composites. Increasing the curing magnetic flux from −800 G to −2600 G increased the values of $\Delta B_1^{\max}$ for both the first cycle and the final cycle. Increasing the annealing magnetic flux from −800 G to −2600 G increased the initial cycle response, but did not have a significant effect on the final cycle response.

The dependence of $\Delta B_3^{\max}$ on curing and annealing magnetic flux for (3,3,1) Terfenol-D composites presented in Table 2.3. In these composites, increasing the curing flux actually lowered the magnitude of $\Delta B_3^{\max}$ in the first cycle. Conversely, increasing the curing flux increased the final cycle response. As seen in the (1,1,1) composites, the annealing flux strength had very little effect on the final cycle response of the (3,3,1) composites.

Table 2.2: Comparison of ΔB_1^{max} for different combinations of curing and annealing magnetic fluxes for (1,1,1) Terfenol-D composites.

Curing magnetic flux (G)	Annealing magnetic flux (G)	ΔB_1^{max} (G)	
		First cycle	Final cycle
-800	-800	0.55	0.30
-800	-2600	0.68	0.34
-2600	-800	0.75	0.45
-2600	-2600	0.77	0.42

Table 2.3: Comparison of ΔB_3^{max} for different combinations of curing and annealing magnetic fluxes for (3,3,1) Terfenol-D composites.

Curing magnetic flux (G)	Annealing magnetic flux (G)	ΔB_3^{max} (G)	
		First cycle	Final cycle
-800	-800	0.44	-0.04
-2600	-800	-0.16	-0.82
-2600	-2600	-0.20	-0.89
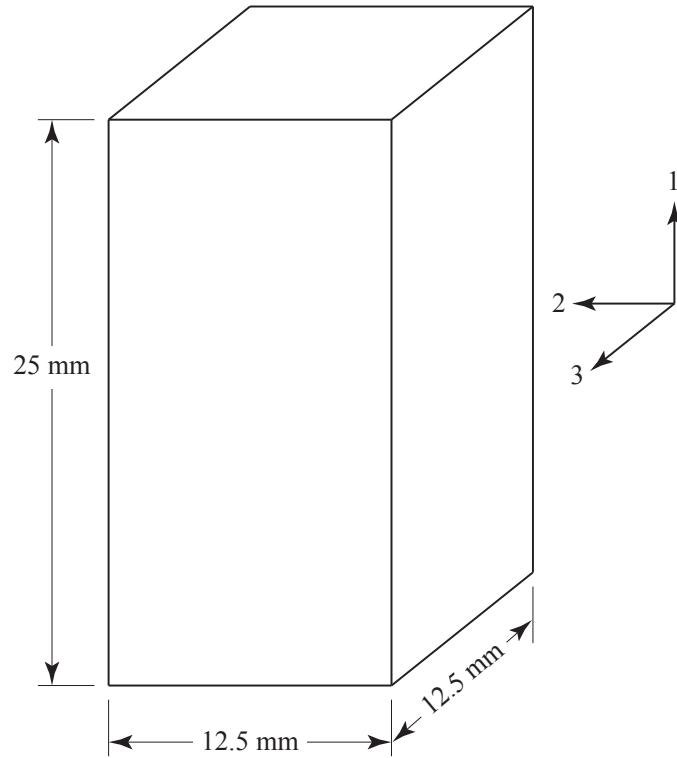
Figure 2.1: Geometry of uniaxial compression specimen.

Magnetic flux
applied during cure

Entire front face   Magnified image
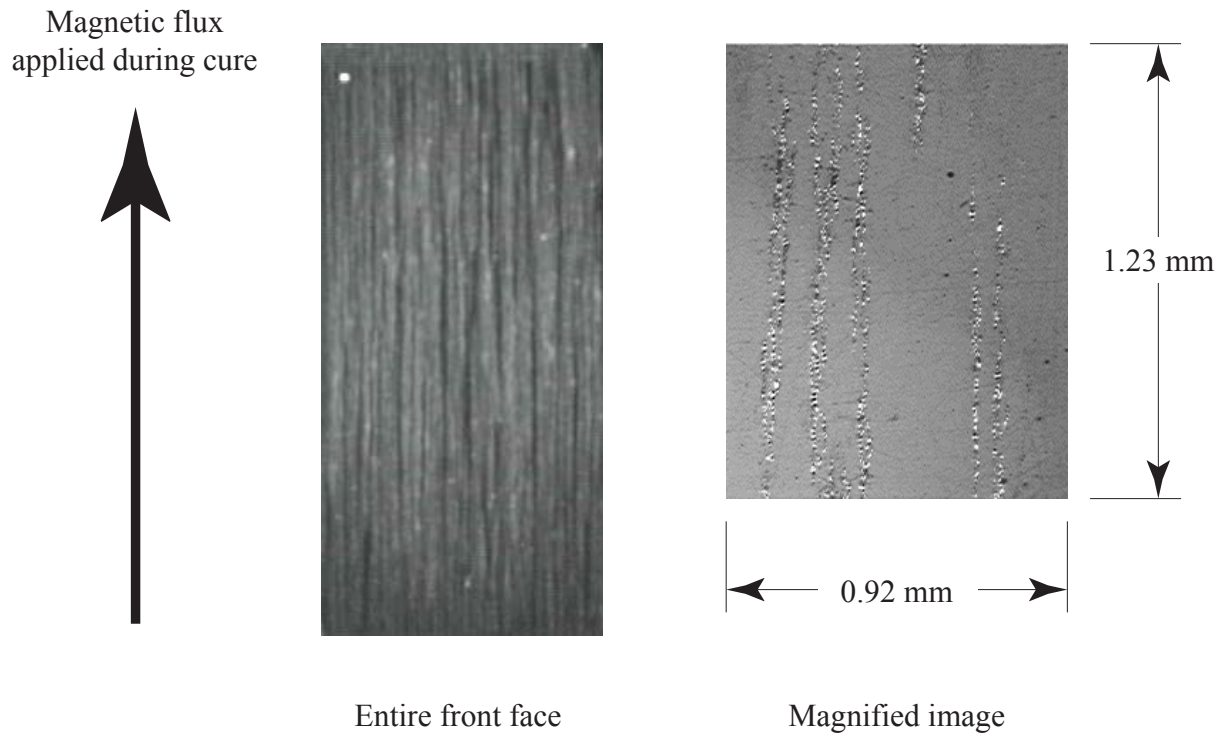
Figure 2.2: Particle chaining phenomenon in Terfenol-D particulate composites cured with a magnetic flux through the length.

Magnetic flux
applied
during cure

Entire front face   Magnified image
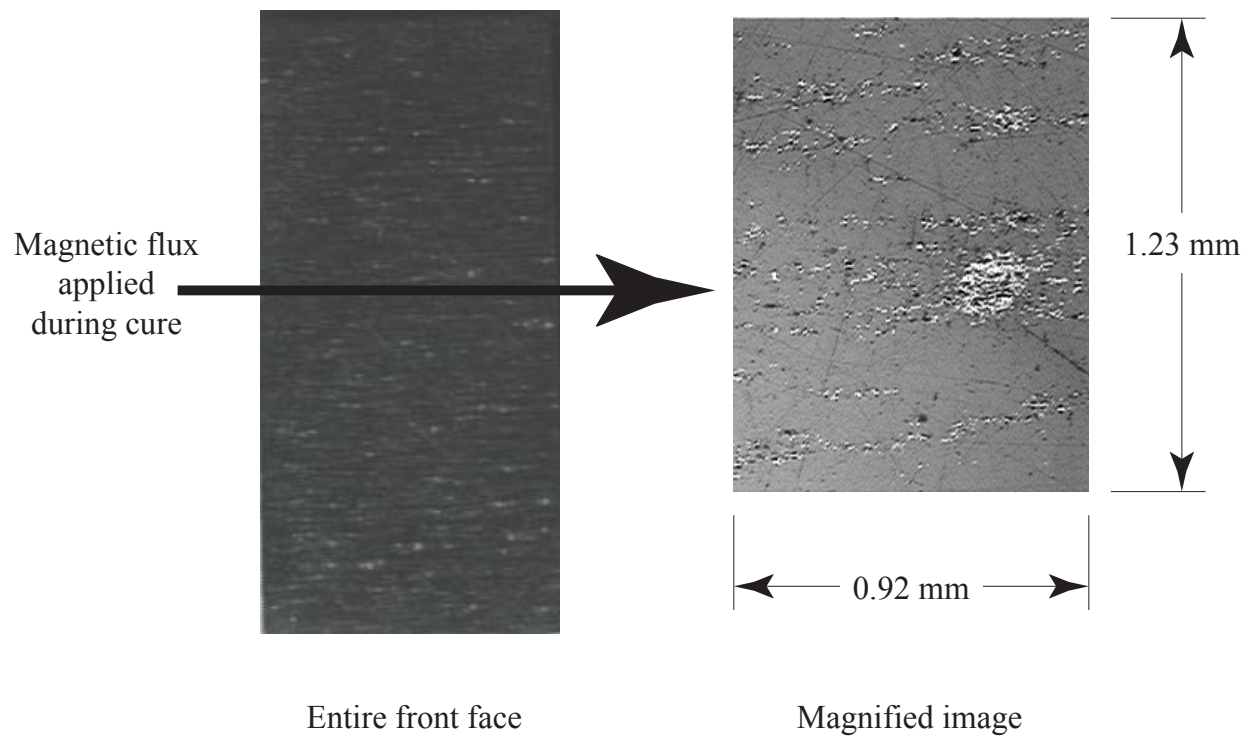
Figure 2.3: Particle chaining phenomenon in Terfenol-D particulate composites cured with a magnetic flux through the width.
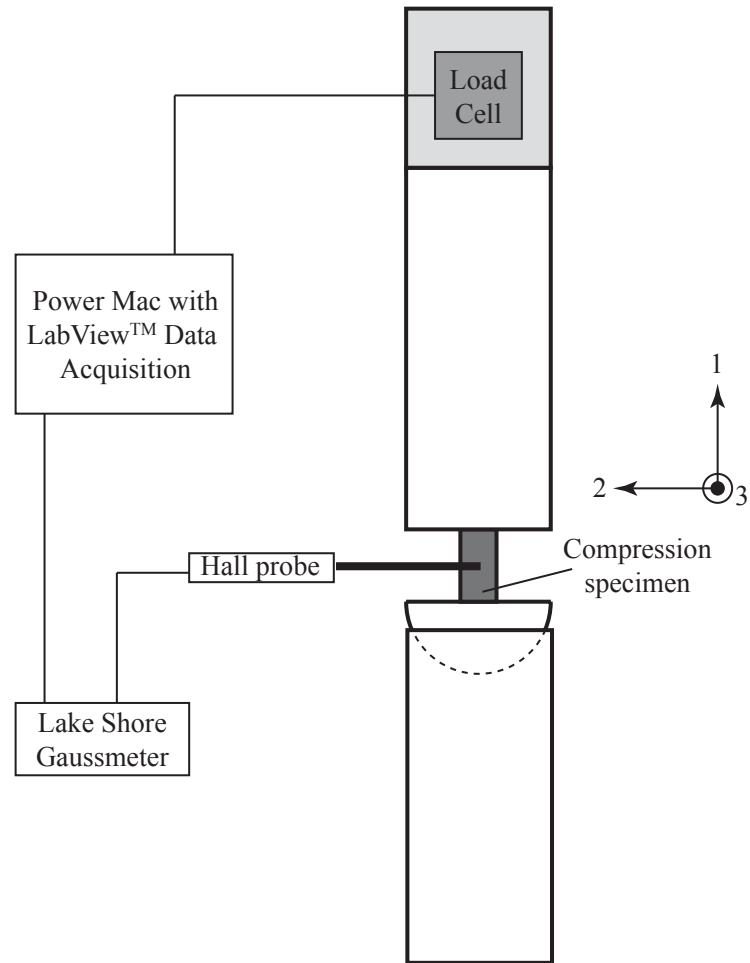
Figure 2.4: Experimental setup for uniaxial compression tests.
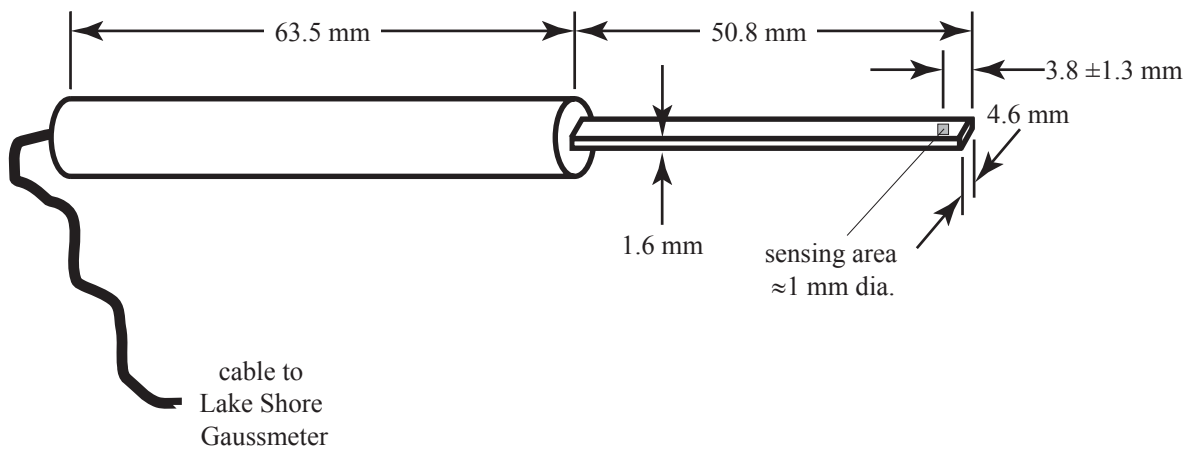
Figure 2.5: Schematic of Hall probe used to measure magnetic flux.
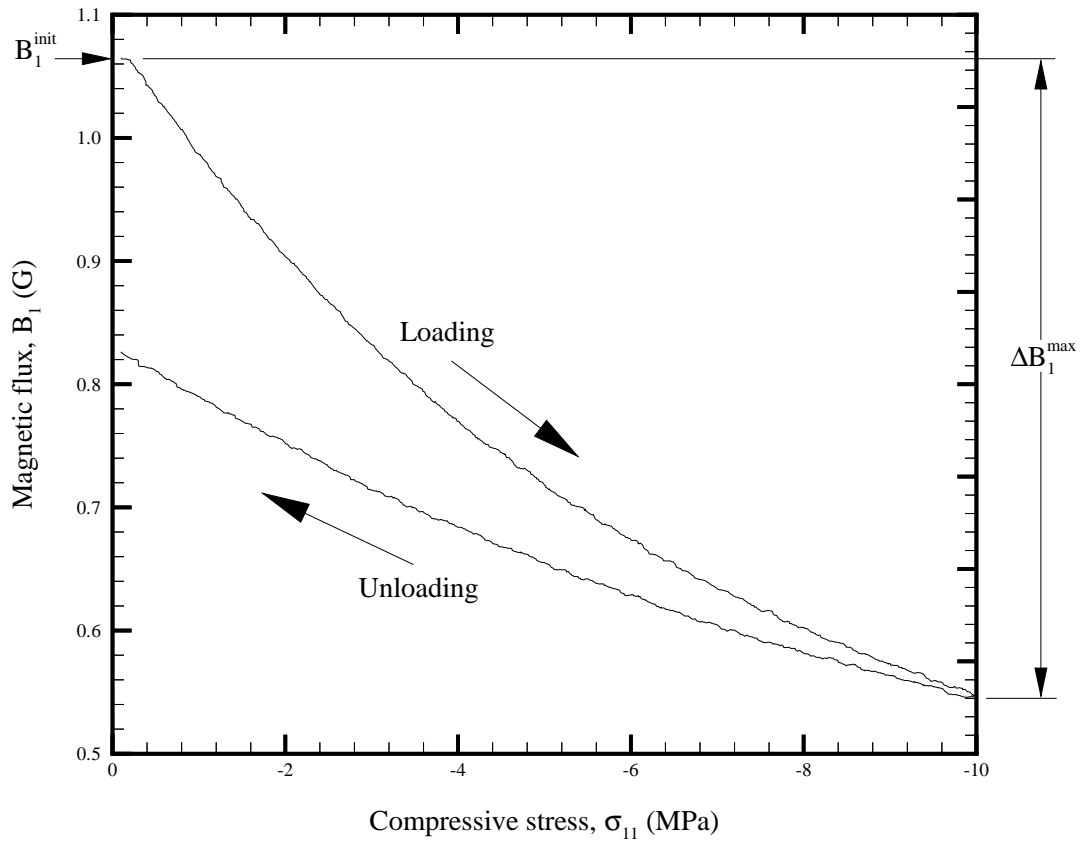
Figure 2.6: Typical response of $(1,1,1)$ composite specimen under uniaxial compressive stress.
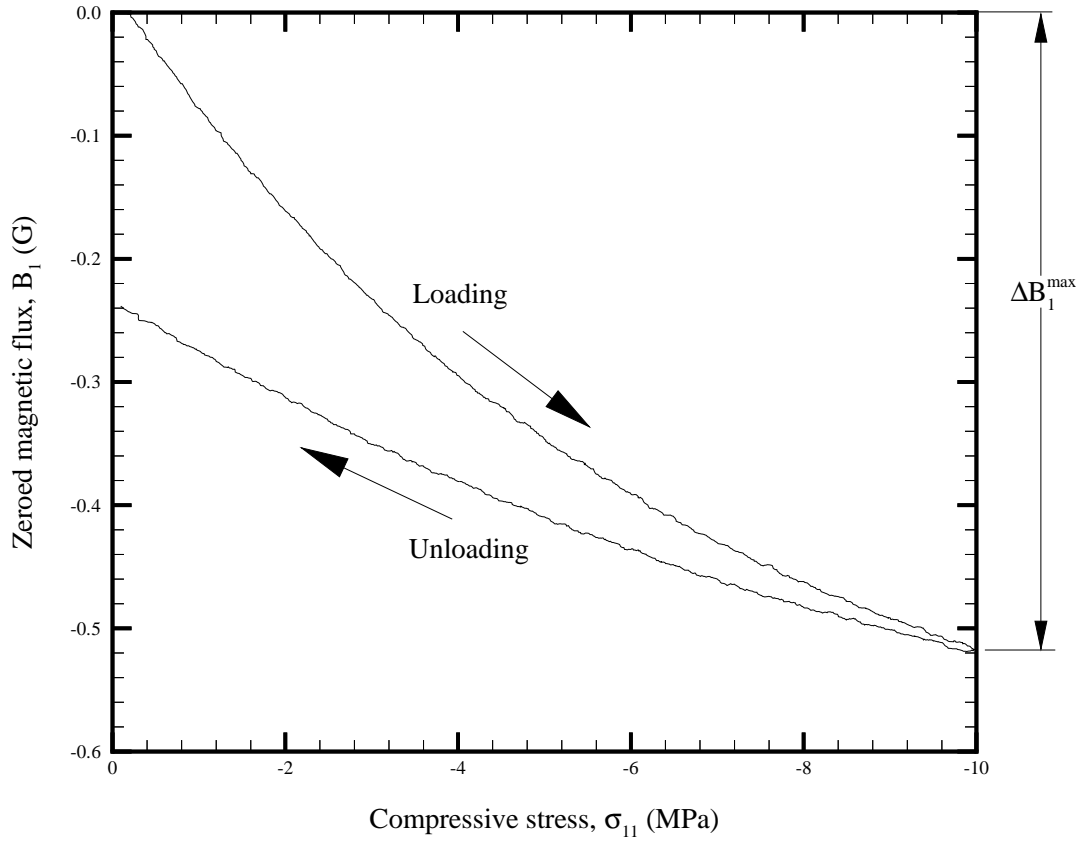
Figure 2.7: Typical response of (1,1,1) composite specimen under uniaxial compressive stress with magnetic flux zeroed by subtracting magnetic flux value at zero load, B_1^{init}.
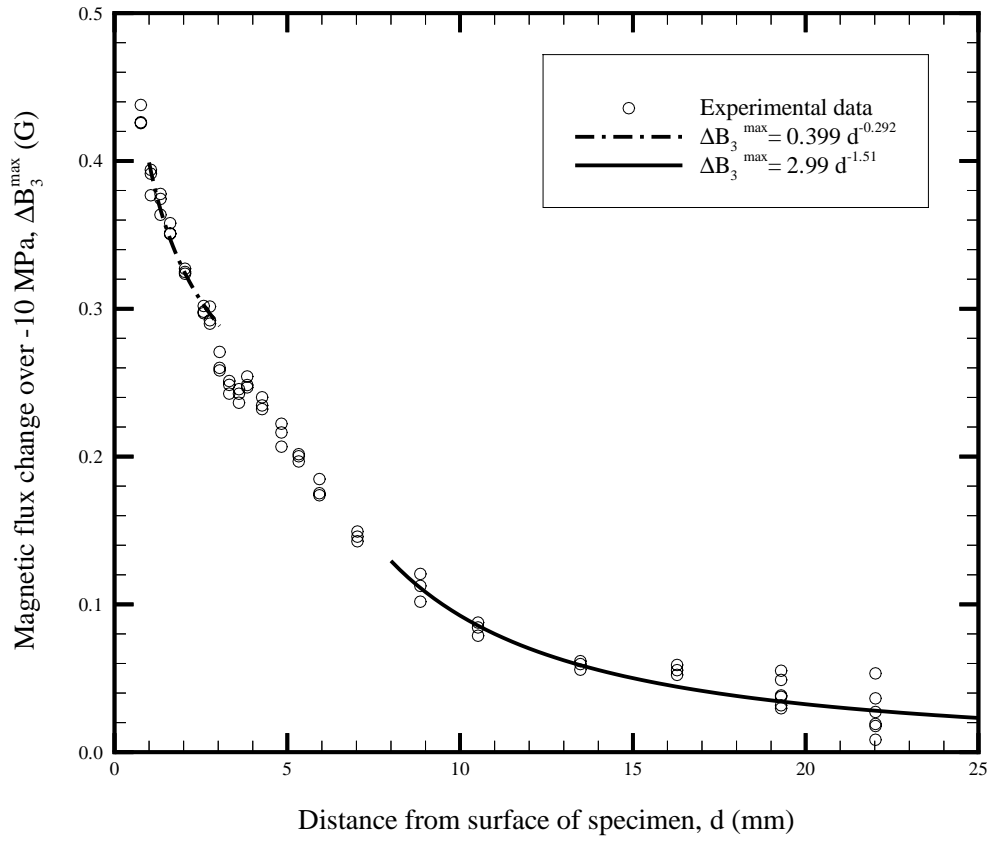
Figure 2.8: Distance dependence of $\Delta B_3^{\max}$ measurement on a (3,3,1) Terfenol-D composite specimen loaded to -10 MPa and annealed at -800 G before each test.

front face ⊥ to 3

+ 8 mm
+ 6 mm
+ 4 mm
+ 2 mm
0 mm
- 2 mm
- 4 mm
- 6 mm
- 8 mm

25 mm

side face
⊥ to -2

6.25 mm   6.25 mm

12.5 mm

1
2
3
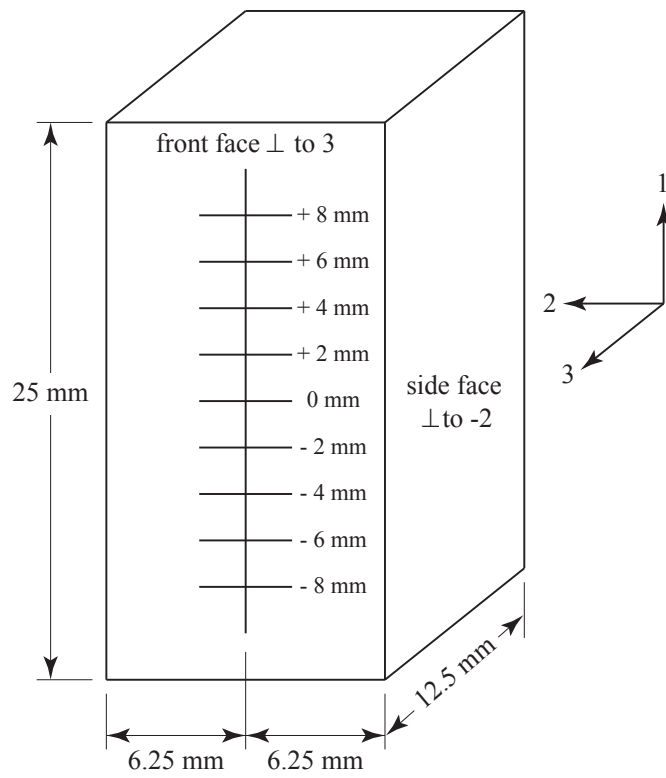
Figure 2.9: Compression specimen marked with grid for gage length characterization.
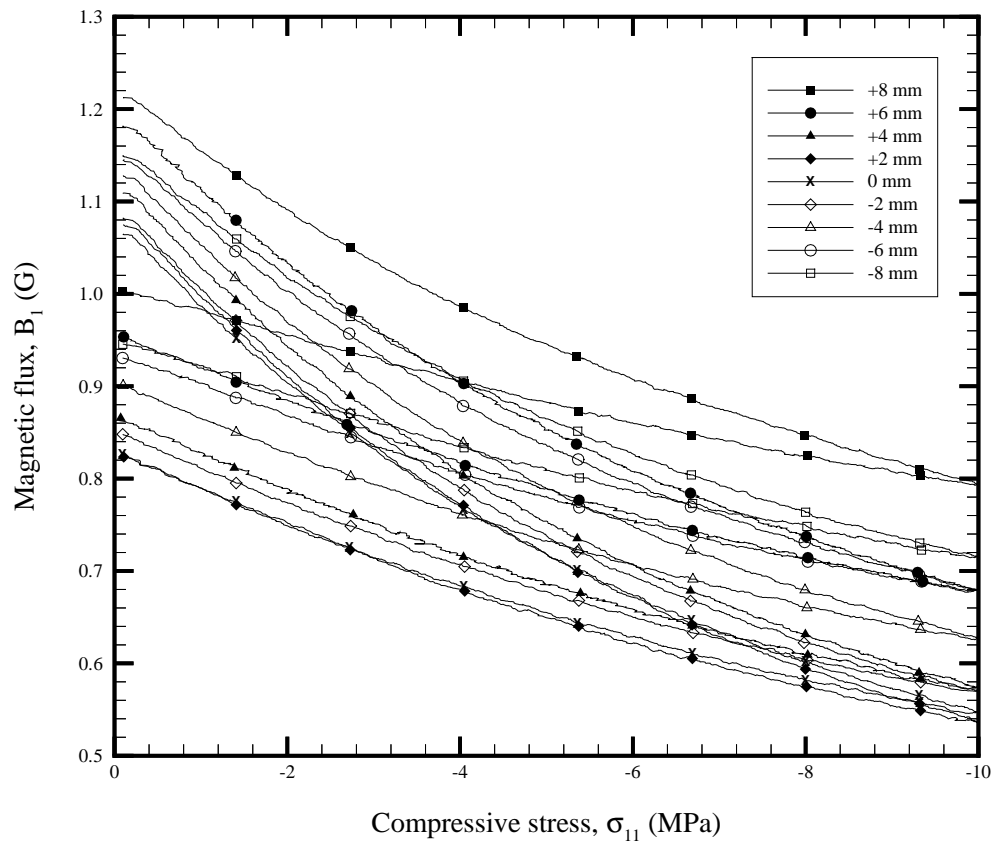
Figure 2.10: Typical gage length response of a (1,1,1) Terfenol-D composite.
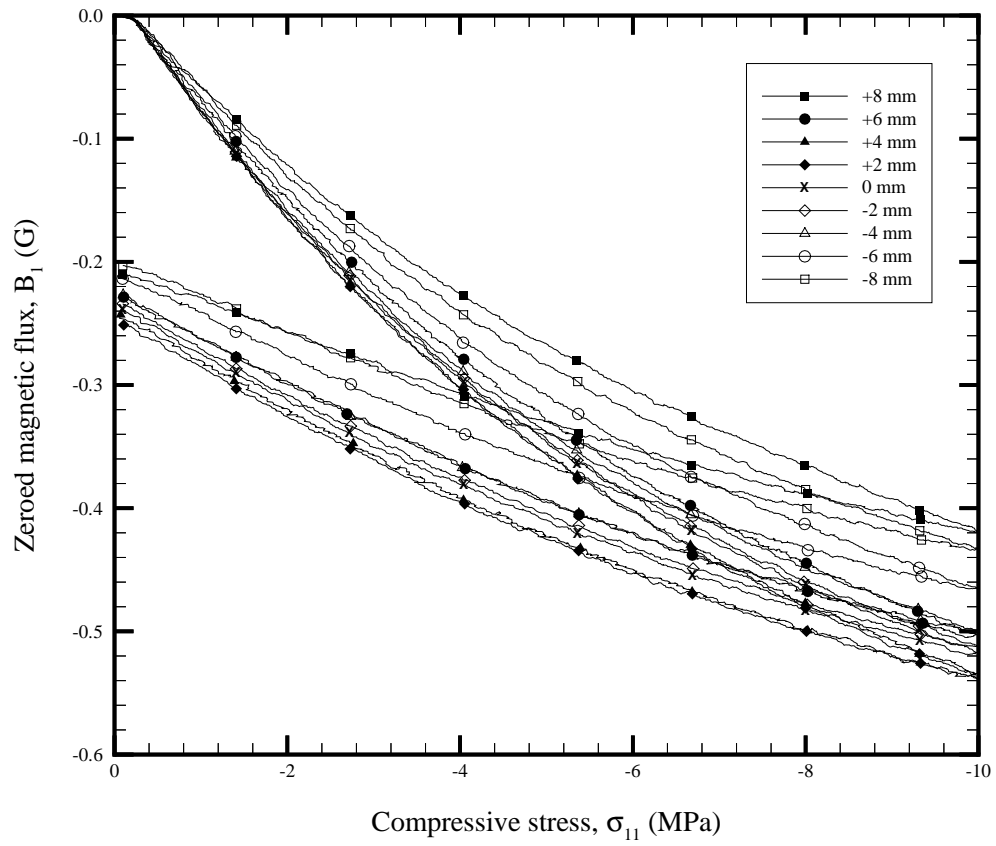
Figure 2.11: Typical gage length response of a (1,1,1) Terfenol-D composite with magnetic flux zeroed by subtracting B_1^{init}.
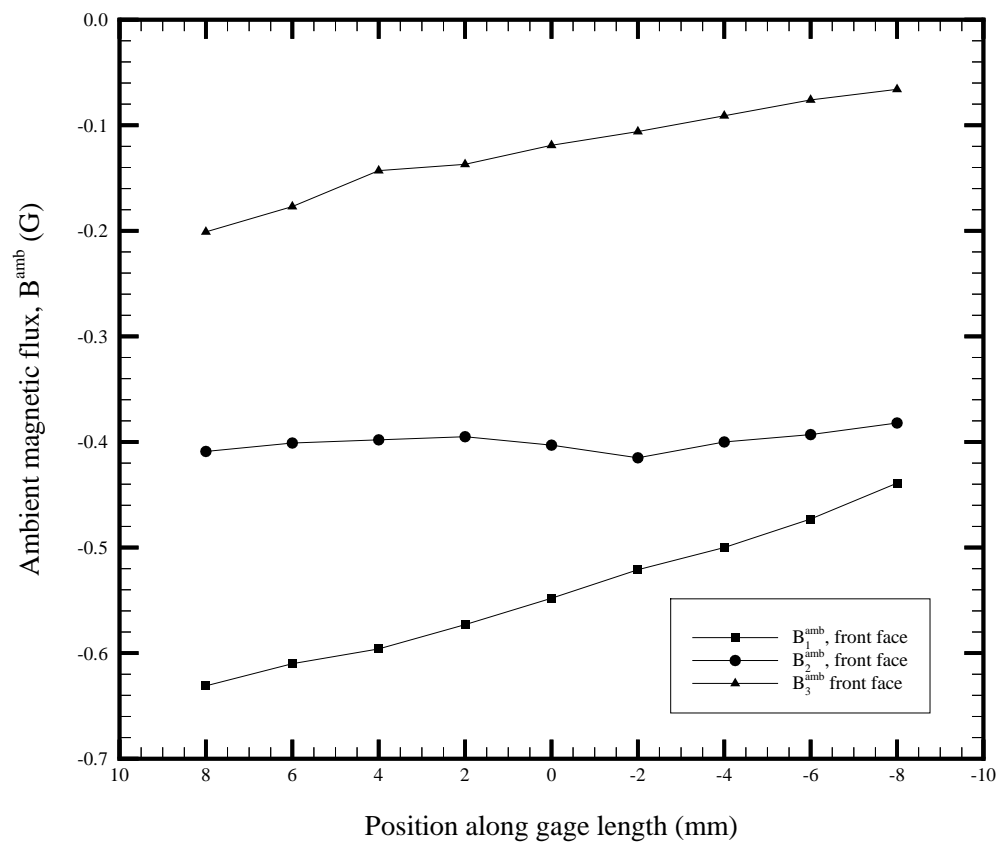
Figure 2.12: Typical ambient magnetic flux measured on a polyester specimen.

36
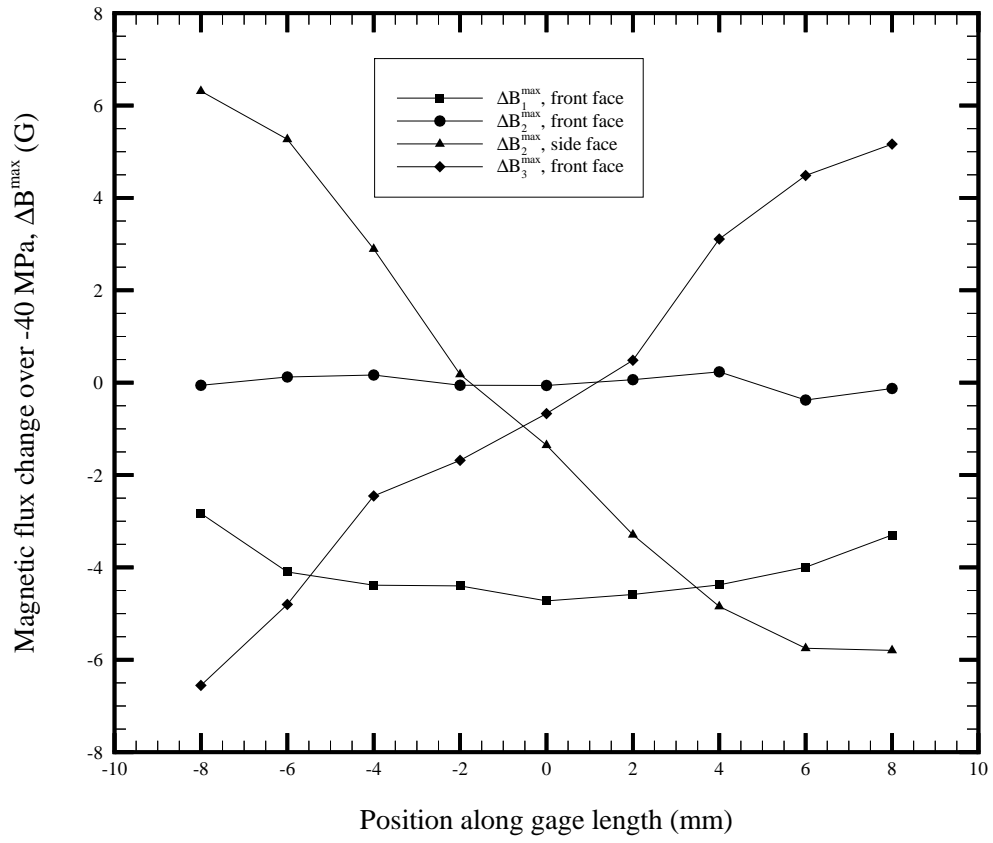
Figure 2.13: Comparison of ΔB^{max}, the change in magnetic flux over -40 MPa, for a pure Terfenol-D specimen annealed at a magnetic flux of -800 G in the 1-direction.
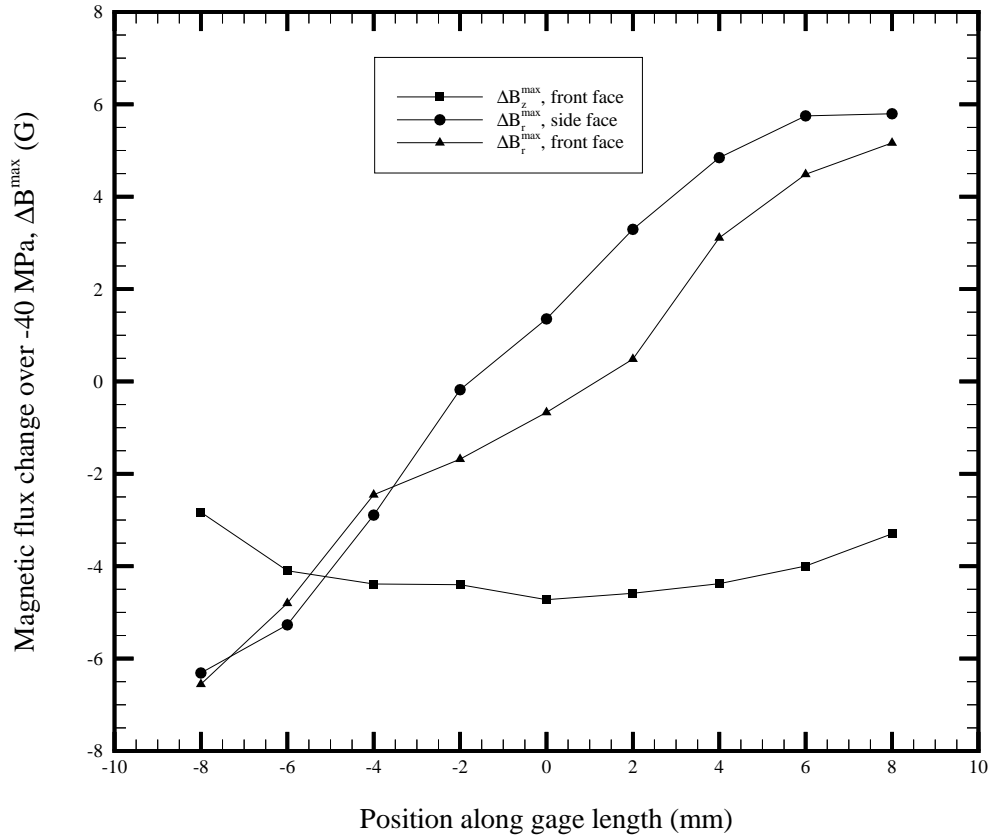
Figure 2.14: Comparison of the change in magnetic flux over -40 MPa, ΔB^{max}, for a pure Terfenol-D specimen annealed at a magnetic flux of -800 G in the z-direction, where z is the axis along the length of the specimen and r points outward.
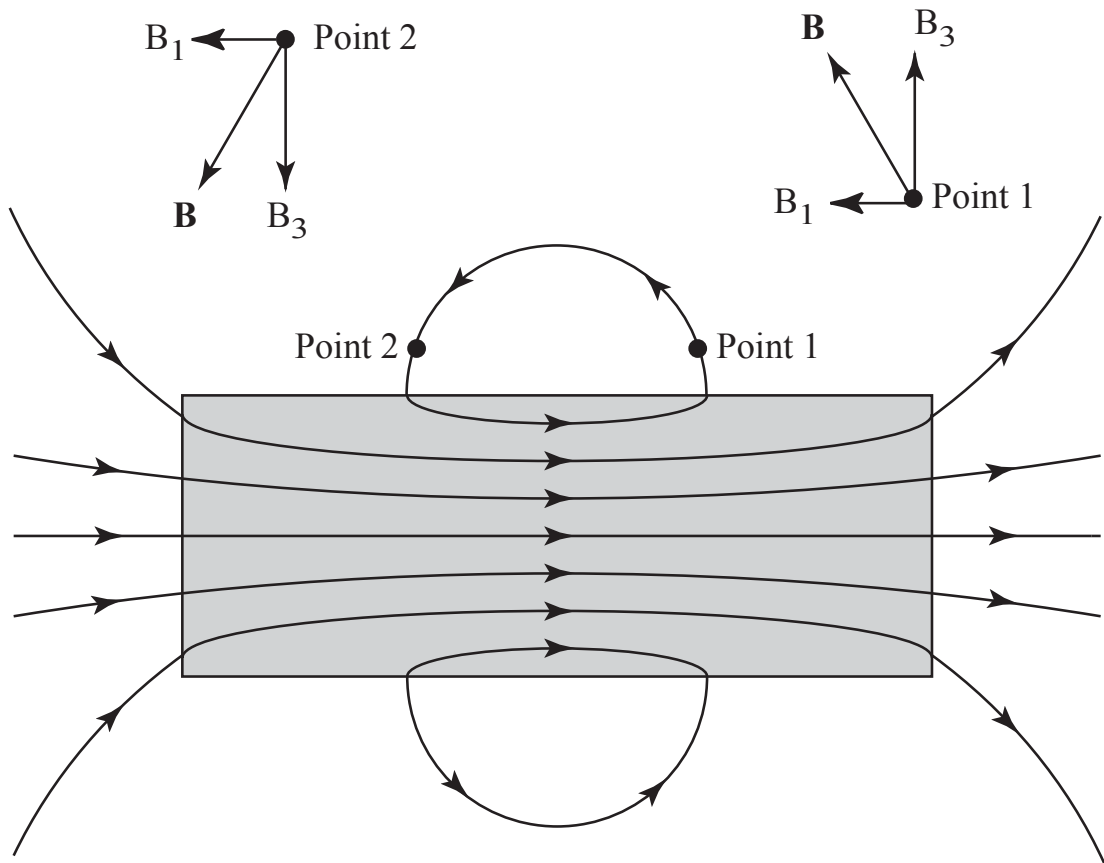
Figure 2.15: Magnetic flux lines of a uniformly magnetized cylinder [26].
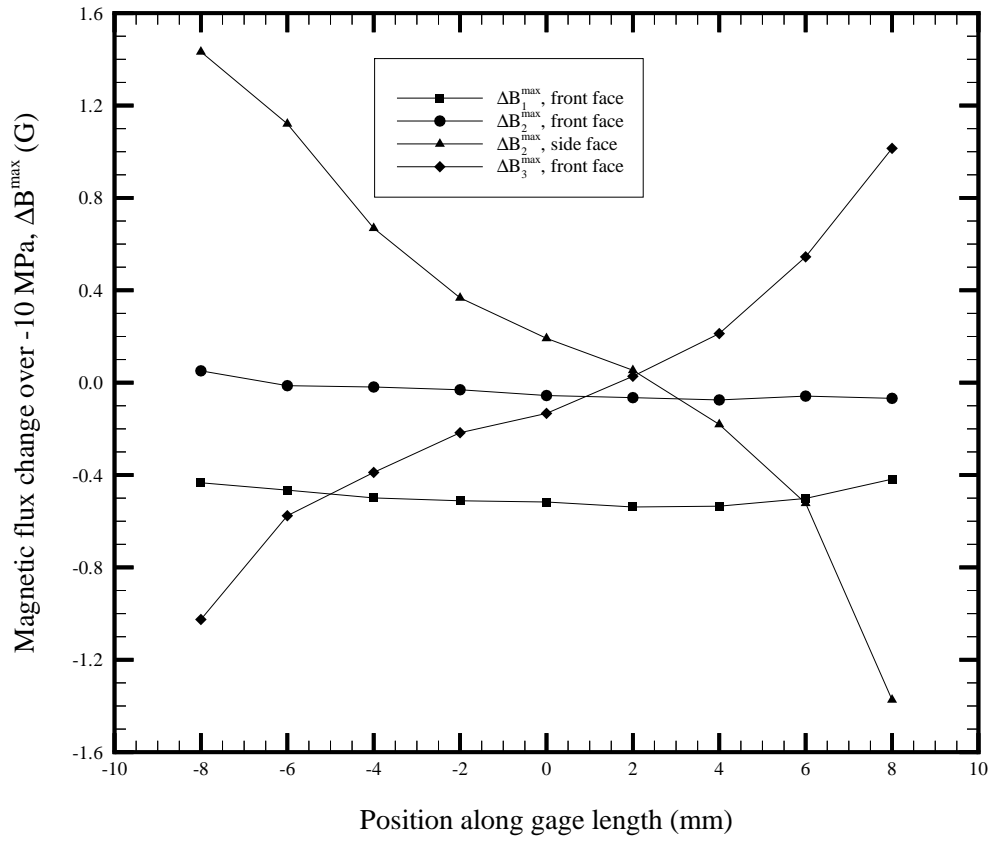
Figure 2.16: Comparison of $\Delta B^{\max}$, the change in magnetic flux over -10 MPa, for a $(1,1,1)$ Terfenol-D composite specimen cured and annealed at -800 G.
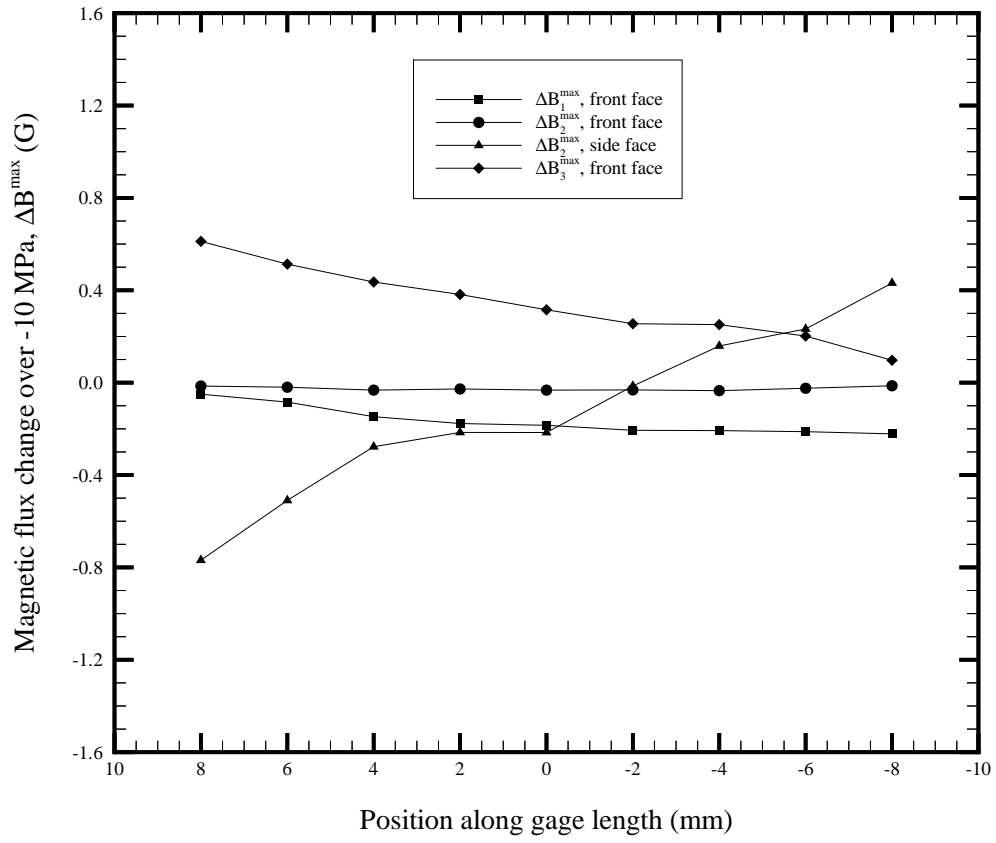
Figure 2.17: Comparison of ΔB^{max}, the change in magnetic flux over -10 MPa, for a $(1,3,1)$ Terfenol-D composite specimen cured at -800 G and annealed at -800 G.
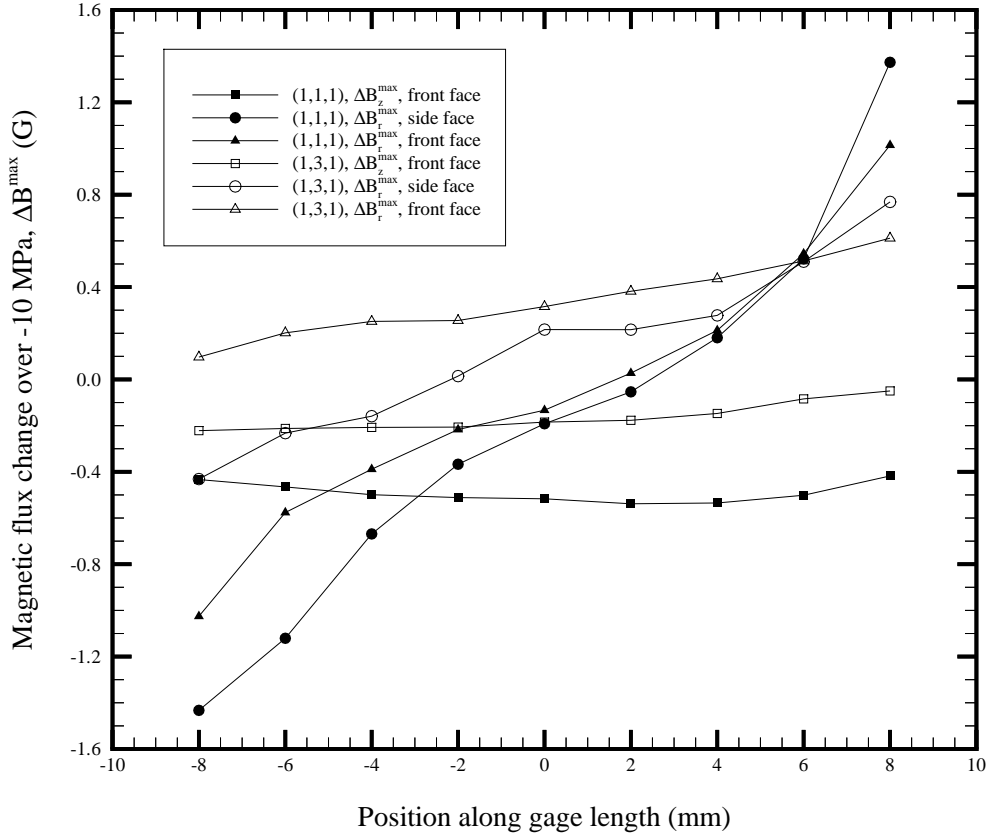
Figure 2.18: Comparison of the change in magnetic flux over -10 MPa, $\Delta B^{\max}$, for $(1,1,1)$ and $(1,3,1)$ Terfenol-D composite specimens cured and annealed at a magnetic flux of -800 G, where z is the axis along the length of the specimen and r points outward.
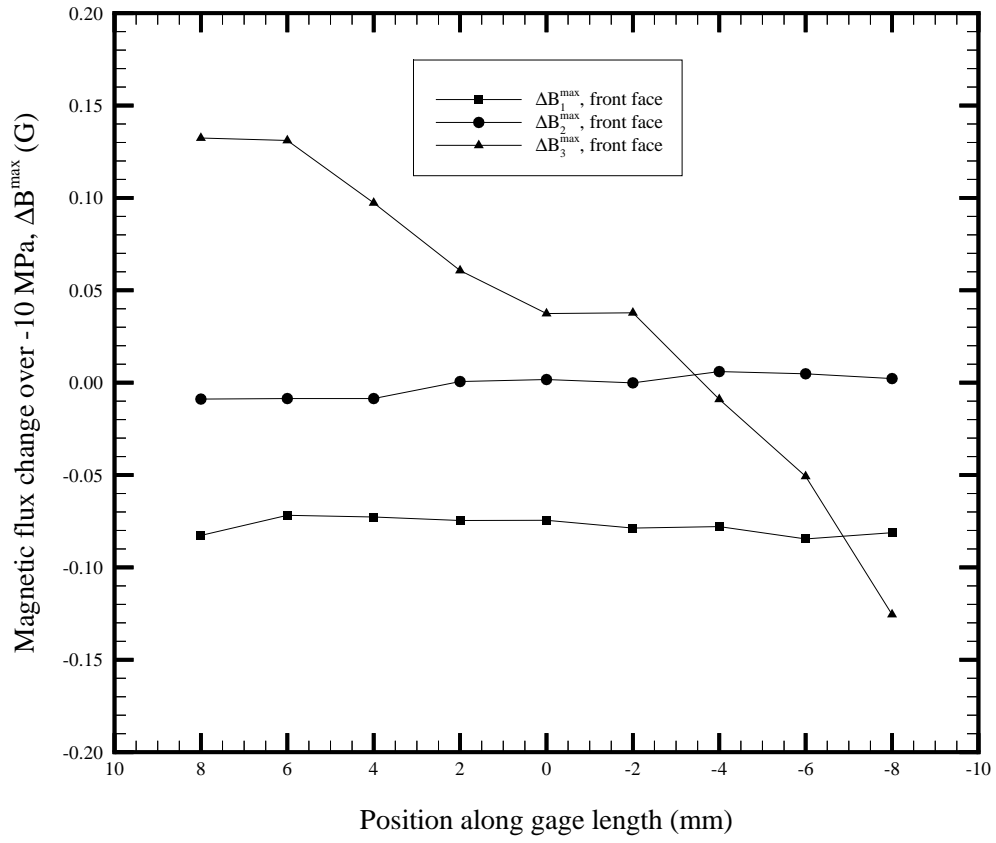
Figure 2.19: Comparison of the change in magnetic flux over -10 MPa, ΔB^{max}, for a $(3,1,1)$ Terfenol-D composite specimen cured at -800 G and annealed at -800 G.
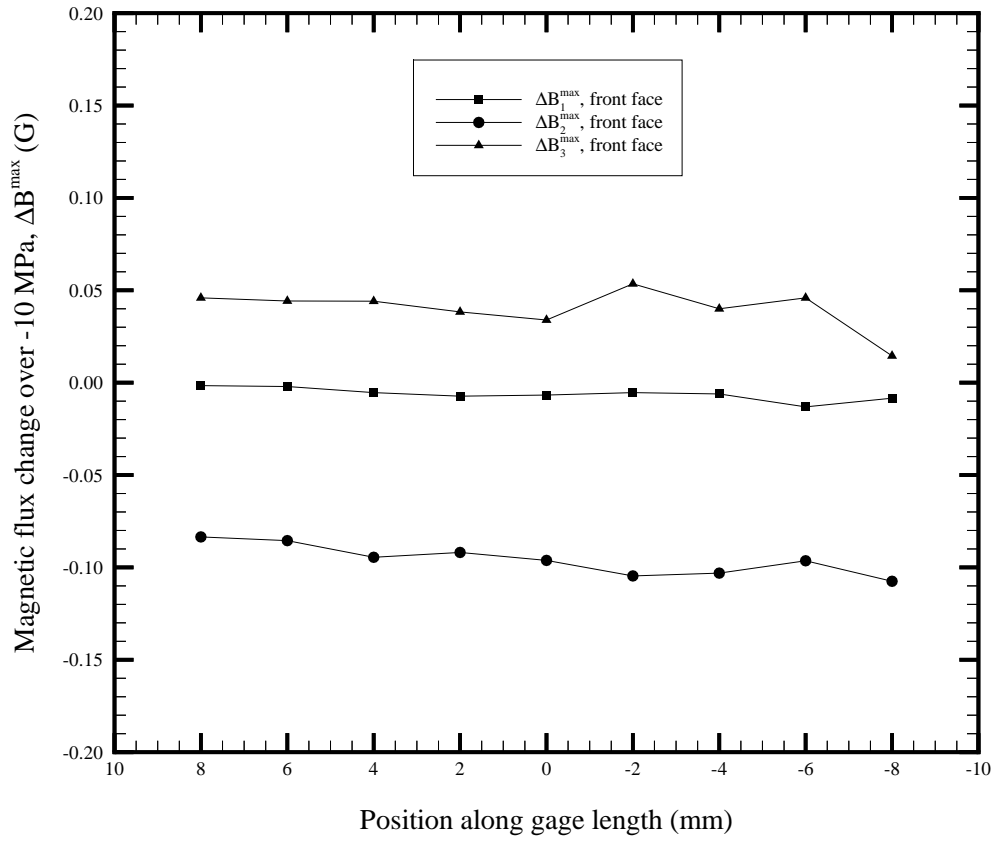
Figure 2.20: Comparison of the change in magnetic flux over -10 MPa, $\Delta B^{\max}$, for a $(3,2,1)$ Terfenol-D composite specimen cured at -800 G and annealed at -800 G.
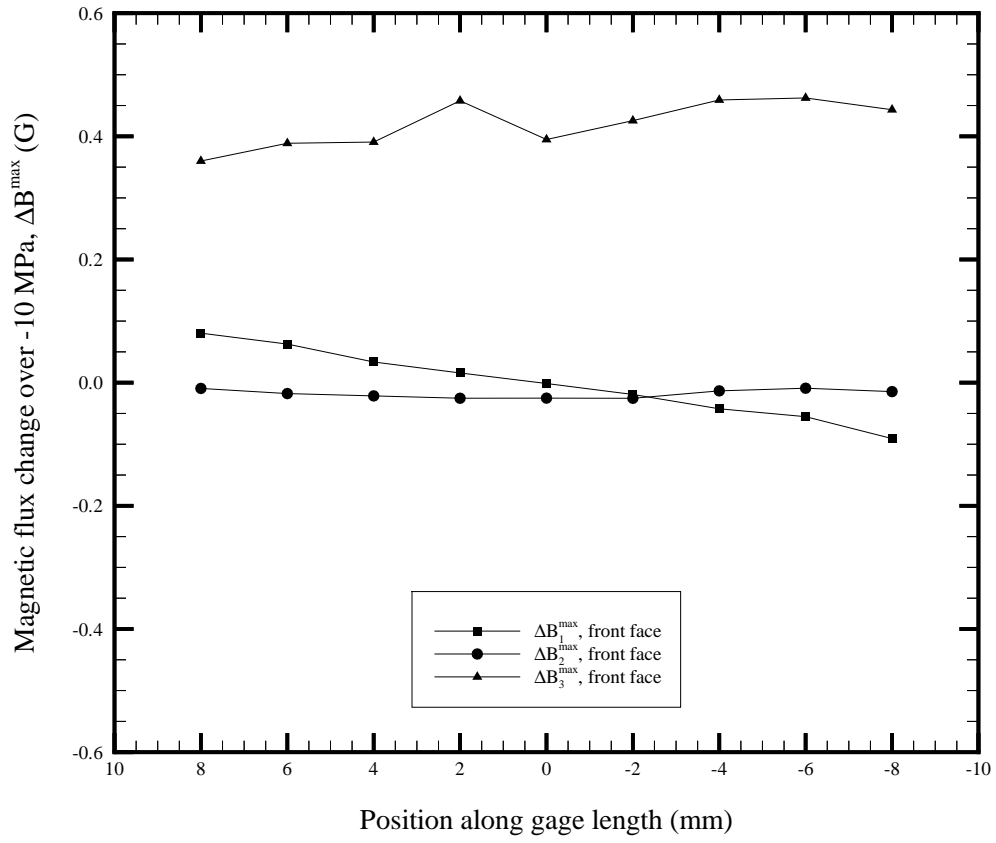
Figure 2.21: Comparison of the change in magnetic flux over -10 MPa, ΔB^{max}, for a (3,3,1) Terfenol-D composite specimen cured at -800 G and annealed at -800 G.

Class I: Poling axis is the same
as the loading axis

Class II: Poling axis is perpendicular
to the loading axis
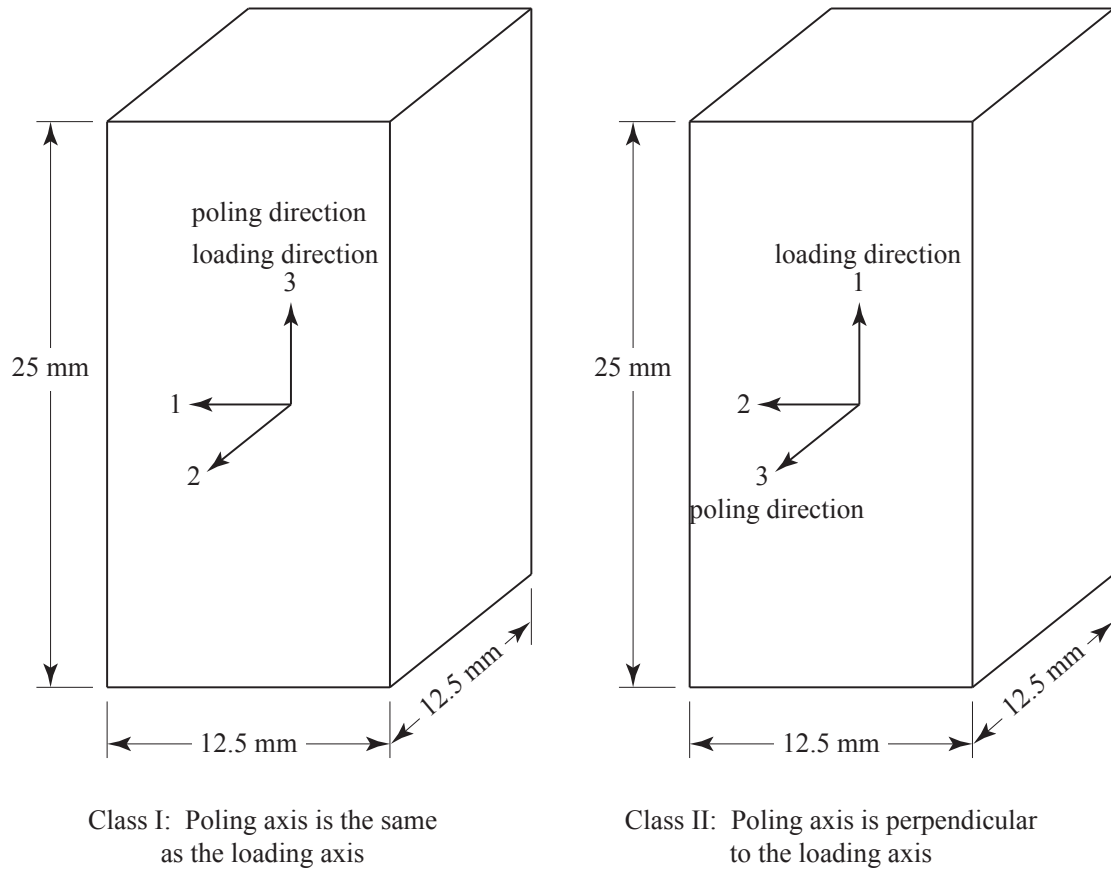
Figure 2.22: Geometries of compression specimens converted to coordinate system used in piezomagnetic literature.
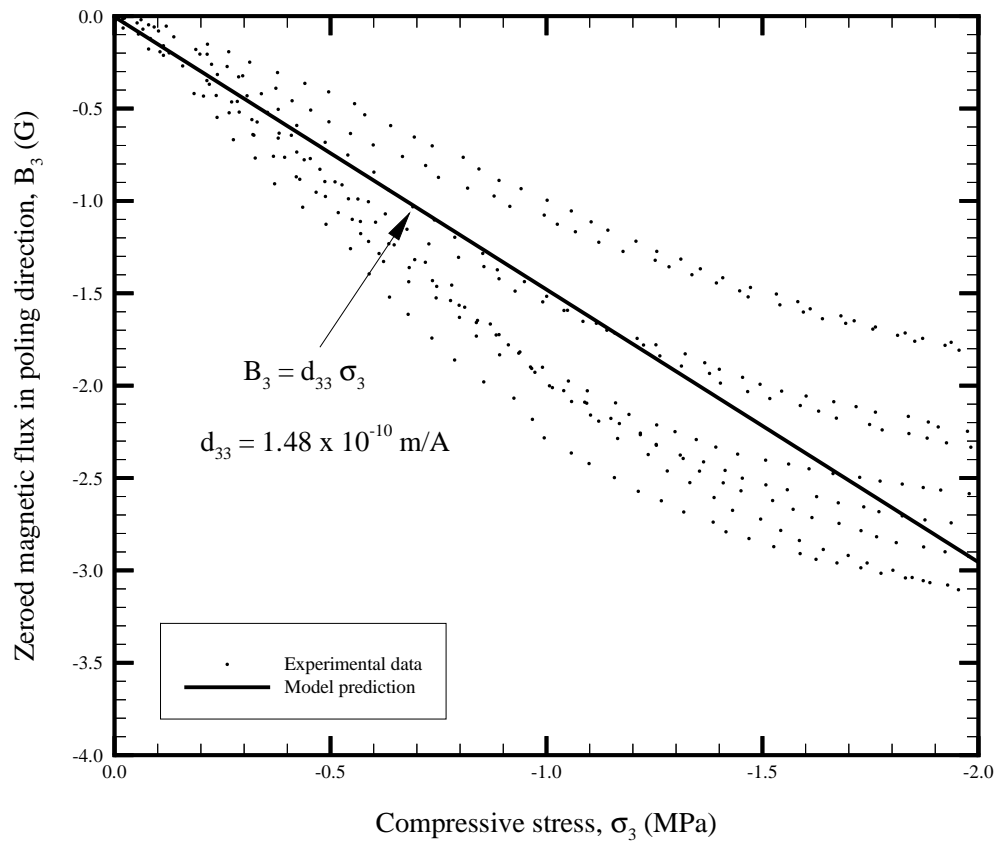
Figure 2.23: Piezomagnetic model prediction and experimental data for Terfenol-D specimen poled in the same direction as the compressive stress.
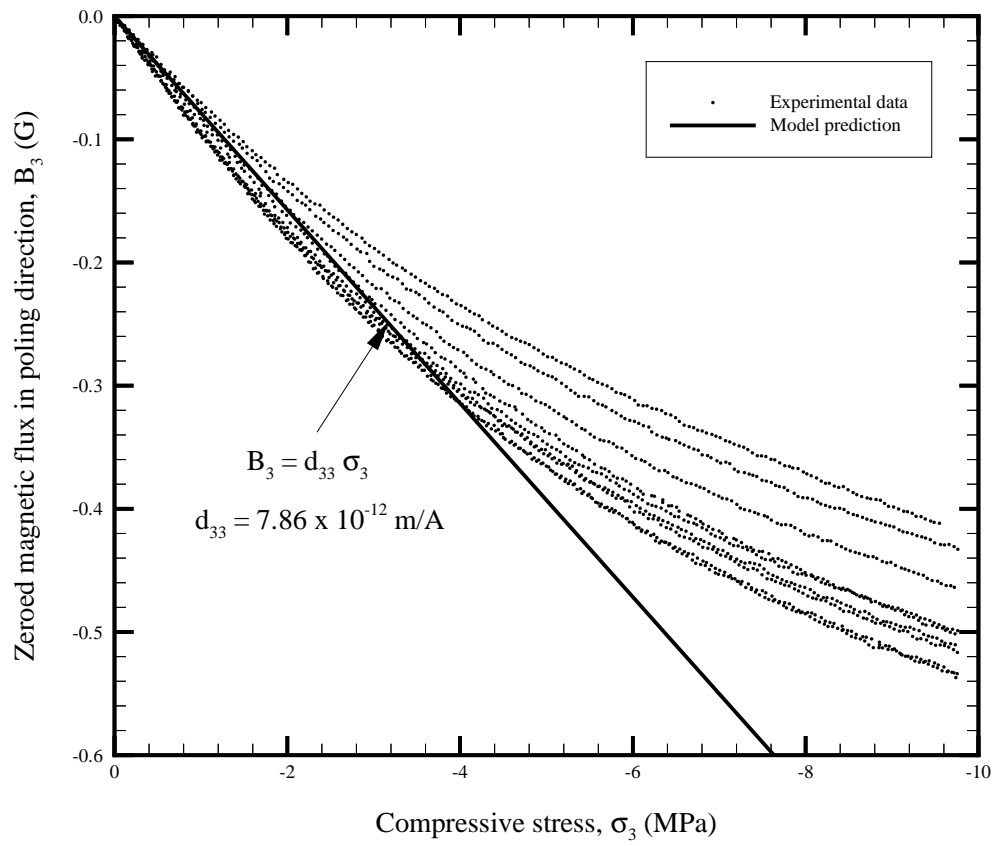
Figure 2.24: Piezomagnetic model prediction and experimental data for (1,1,1) Terfenol-D composite specimen.
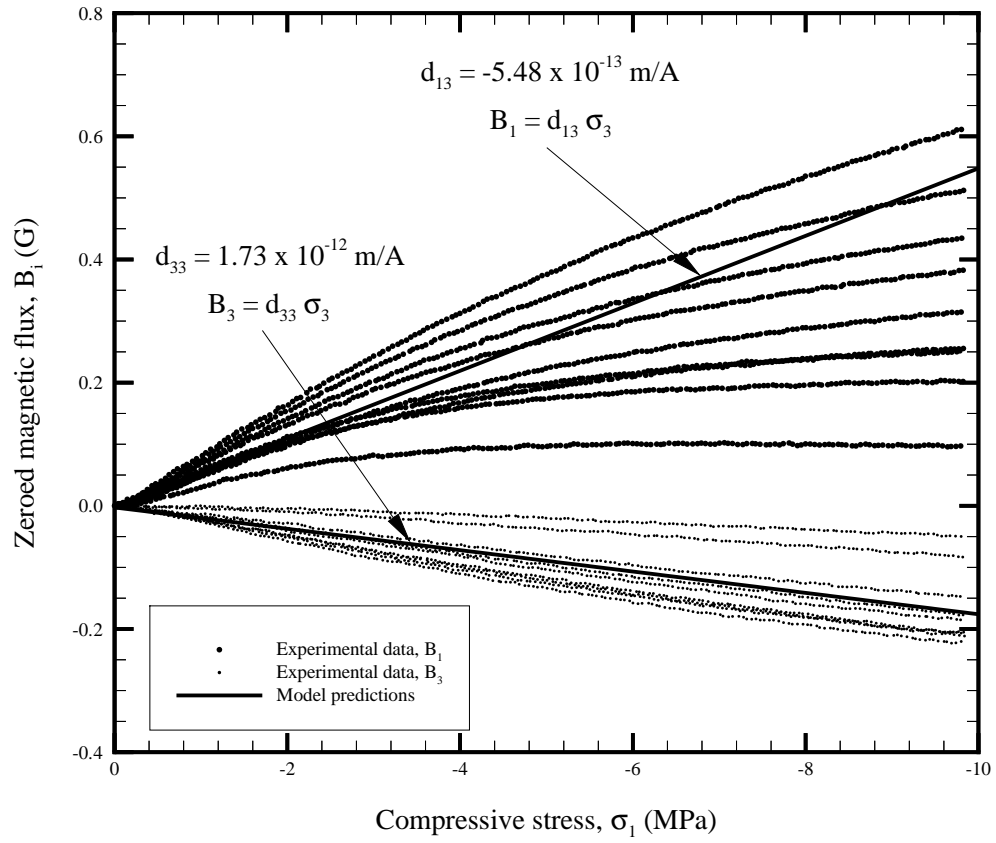
Figure 2.25: Piezomagnetic model prediction and experimental data for (1,3,1) Terfenol-D composite specimen.
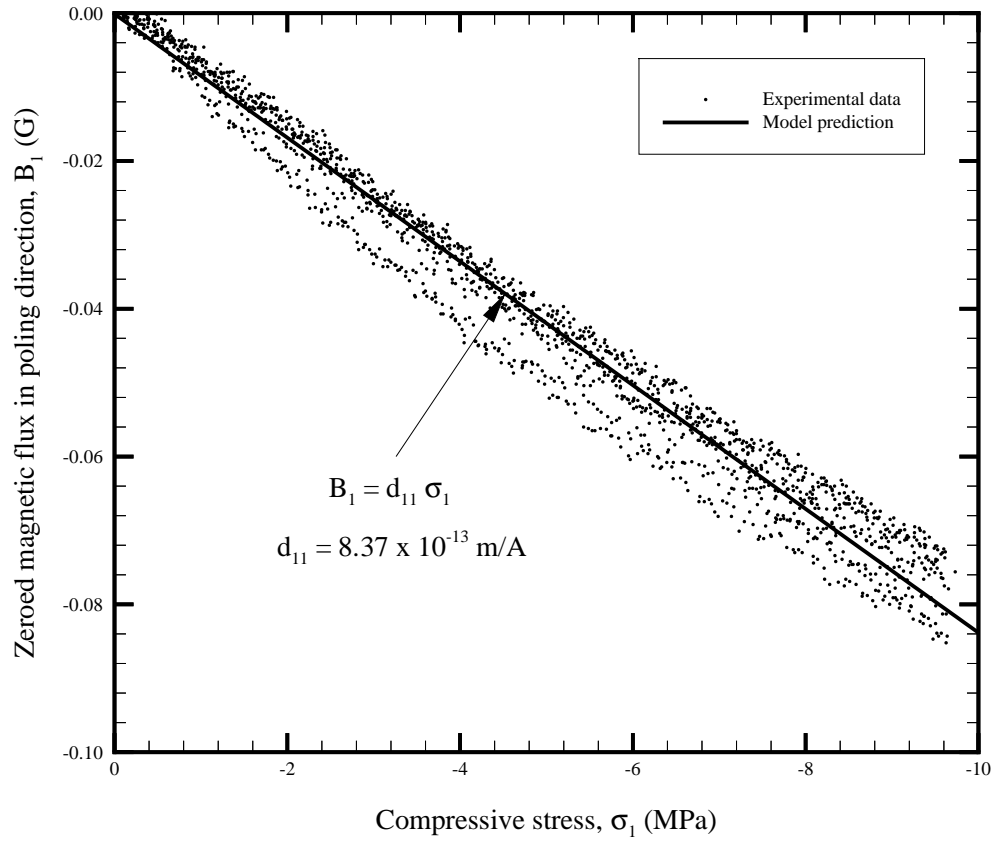
Figure 2.26: Piezomagnetic model prediction and experimental data for (3,1,1) Terfenol-D composite specimen.
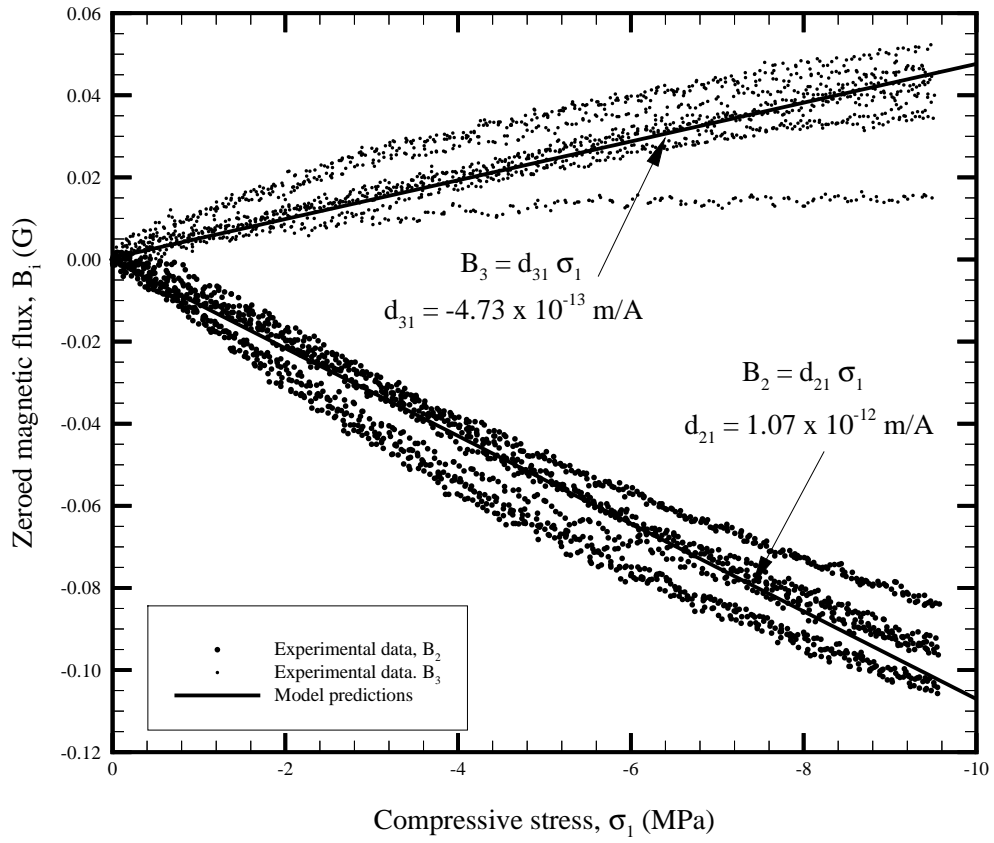
Figure 2.27: Piezomagnetic model prediction and experimental data for (3,2,1) Terfenol-D composite specimen.
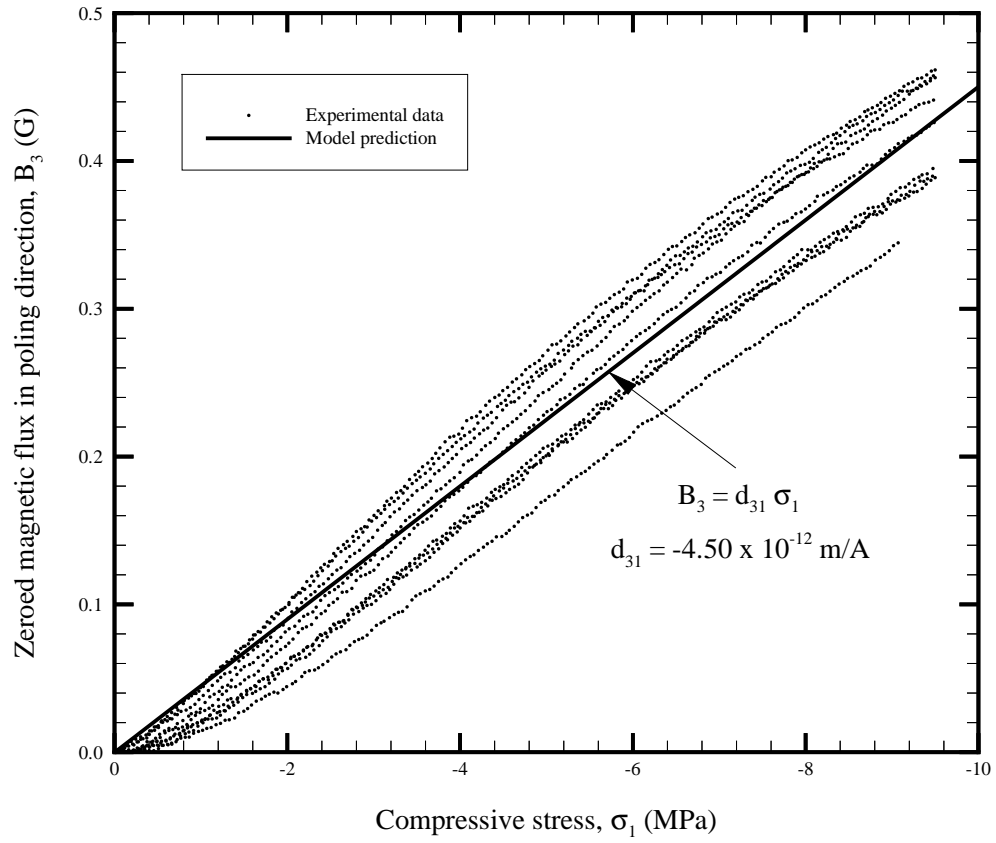
Figure 2.28: Piezomagnetic model prediction and experimental data for (3,3,1) Terfenol-D composite specimen.
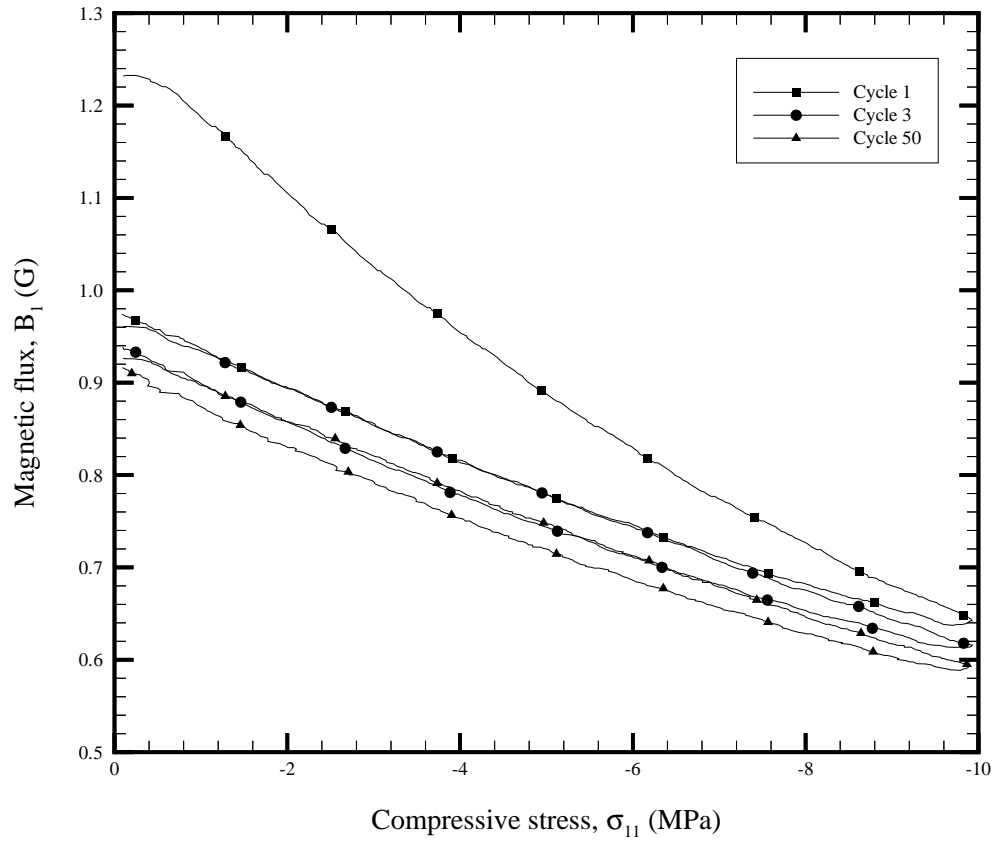
Figure 2.29: Typical cyclic response for a Terfenol-D composite loaded in uniaxial compression to -10 MPa with annealing only once before the first cycle.

53
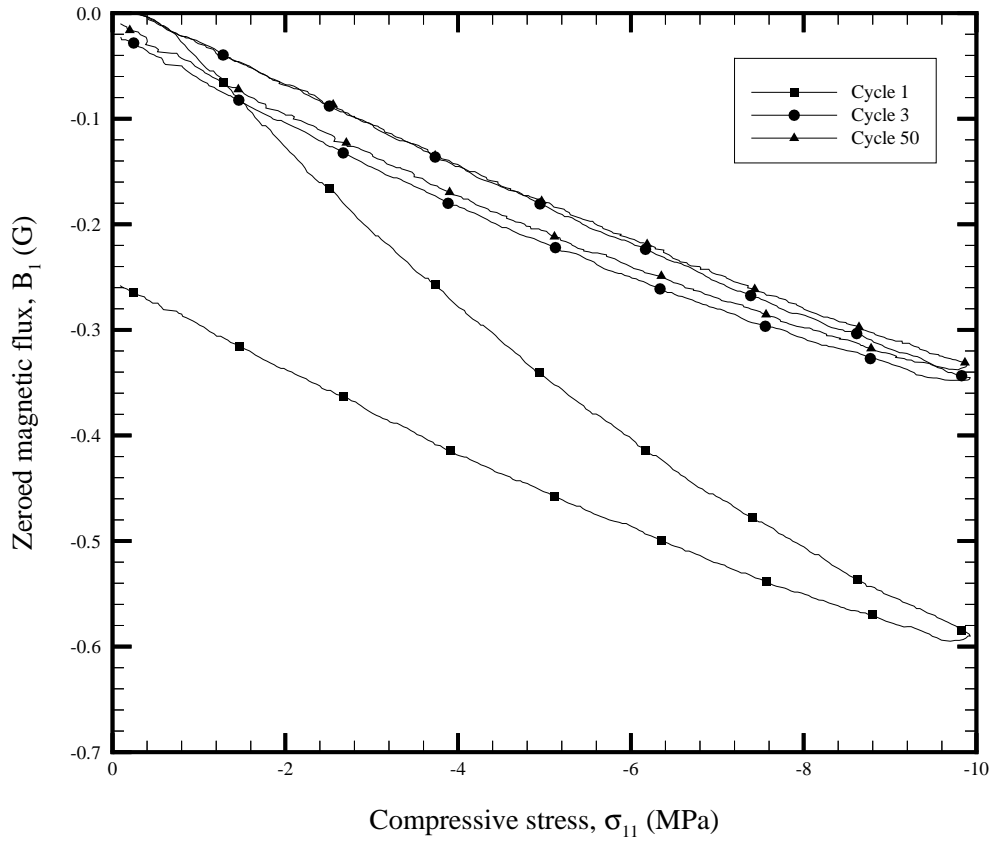
Figure 2.30: Typical cyclic response for a Terfenol-D composite loaded in uniaxial compression to −10 MPa with annealing only once before the first cycle.

Chapter 3

Residual stress analysis

3.1   Introduction

Several competing mechanisms contribute to residual stress development during the fabrication of Terfenol-D composites. Initially, the polyester–particulate mixture is at room temperature and able to flow freely. Then, the mixture is poured into a mold and placed between two magnets. The magnetic field causes the Terfenol-D particles to strain via the magnetostrictive effect as discussed in Section 1.2. At this time, the polyester is also generating heat from the polymerization and crosslinking reactions. Until the polymer "sets" or "gels", there is no stress on the particles and they move freely to align in chains along the field lines between the magnets as shown in Figure 3.1. Once gelation occurs, the particles are constrained and any further chemical shrinkage of the matrix will produce stresses on the particles. Also, the temperature drops slowly back down to room temperature and thermal mismatch stresses occur. When a specimen is taken out of its mold, it is no longer under the influence of a magnetic field, so the magnetostrictive strains are released.

Many theories and models exist for predicting residual stresses in a composite, but few, if any, can be directly applied to the particulate composites at hand. Some of the papers focus on fiber–reinforced composites, especially with thermosetting resin matrices [34, 31]. These theories could be applied to the Terfenol-D particulate composites at hand if the particulate chains are modeled as fibers. There are also a large number of papers in the literature for

metal–matrix particulate composites [3, 12, 24]. The major focus of these papers is residual stresses induced by thermal mismatch. These papers offer the best theories to build on and modify for Terfenol-D composites.

3.2 Analysis

A modified Eshelby model is used to determine the residual stress field in the Terfenol-D composite. The model is based on a similar analysis presented by Hsueh and Becher [12] in which ellipsoidal inclusions are modeled. The residual stress from thermal mismatch is calculated for a number of different inclusion geometries using an anisotropic coefficient of thermal expansion. The geometry of the inclusion is represented by

$$\left(\frac{X_1}{a}\right)^2 + \left(\frac{X_2}{a}\right)^2 + \left(\frac{X_3}{c}\right)^2 = 1 \tag{3.1}$$

with X_3 being the unique axis of the ellipsoid as shown in Figure 3.2. By choosing the ratio c/a appropriately, the geometry of an ellipsoid, sphere, disk, or fiber can be represented. For this analysis, the inclusions are modeled in two ways. First, a single particle is modeled as a spherical inclusion. This may not be the best geometric assumption as the particles group very close together and form chains as shown in Figure 3.1. Therefore, in the second analysis, a chain of multiple particles is represented by an ellipsoidal inclusion. Linear isotropic elasticity is assumed for both the matrix and the inclusions. The model is expanded from the work of Hsueh and Becher [12] to include magnetostrictive effects and chemical shrinkage as sources of residual stress.

The Eshelby model represents the problem of mismatch stresses by applying a series of virtual operations on an inclusion. First, it is imagined that the inclusion is removed from the matrix and all mismatch strains are allowed to develop unconstrained. The strains that develop in this step are defined as the *transformation strains*, ϵ_{ij}^{t*}. In this analysis, the

56

transformation strains are

$$\epsilon_{ij}^{t*} = \epsilon_{ij}^{\mathrm{th}} + \epsilon_{ij}^{\mathrm{ch}} + \epsilon_{ij}^{\mathrm{mag}} \tag{3.2}$$

where $\epsilon_{ij}^{\mathrm{th}}$ are the thermal mismatch strains, $\epsilon_{ij}^{\mathrm{ch}}$ are the chemical shrinkage strains, and $\epsilon_{ij}^{\mathrm{mag}}$ are the magnetostrictive strains. All these strains are either isotropic or transversely isotropic about the X_3 axis of the inclusion.

Next, an imaginary surface traction is applied to the inclusion to fit it back into its void in the matrix. The surface traction creates a stress in the inclusion but no stress in the matrix. To correct this imbalance, the applied surface traction is treated as a layer of body force and an equal and opposite layer of body force is applied at the interface to make the net surface traction vanish along the interface. The strains induced by these body forces are termed *constrained strains*, ϵ_{ij}^{c}, and are functions of the transformation strains, ϵ_{ij}^{t*}. The final residual stresses in the inclusion are spatially uniform and arise from the difference, $\epsilon_{ij}^{c} - \epsilon_{ij}^{t*}$, while the residual stresses in the matrix arise from ϵ_{ij}^{c}.

The Eshelby model, as presented for an ellipsoidal inclusion in an infinite matrix, gives the relationship between ϵ_{ij}^{c} and ϵ_{ij}^{t*} for the case where the elastic properties of the matrix and inclusion are the same. For a composite consisting of two distinct phases, an additional modification is required. First, isotropic linear elasticity is assumed for both the matrix and the inclusion. The true inclusion is then virtually replaced by an *equivalent inclusion* and the *equivalent transformation strains*, ϵ_{ij}^{t}, result. To insure the sameness of stresses and displacements in the two inclusions, two relationships must hold:

$$K_{\mathrm{e}}(\epsilon^{c} - \epsilon^{t*}) = K_{\mathrm{m}}(\epsilon^{c} - \epsilon^{t}) \tag{3.3a}$$

$$G_{\mathrm{e}}(\hat{\epsilon}_{11}^{c} - \hat{\epsilon}_{11}^{t*}) = G_{\mathrm{m}}(\hat{\epsilon}_{11}^{c} - \hat{\epsilon}_{11}^{t}) \tag{3.3b}$$

where K and G are bulk and shear moduli for the ellipsoidal inclusion (subscript e) and the matrix (subscript m). The dilatational and deviatoric strains in Equations (3.3a) and (3.3b)

are defined by

$$\epsilon = \epsilon_{11} + \epsilon_{22} + \epsilon_{33} \tag{3.4a}$$

$$\hat{\epsilon}_{11} = \frac{1}{3}\left(\epsilon_{11} - \epsilon_{33}\right) \tag{3.4b}$$

Finally, the Eshelby model is modified to reflect the finite volume fraction of inclusions. The presence of surrounding inclusions introduces an additional constraint, such that

$$\epsilon^c_{ij} = \epsilon^{c'}_{ij} + \epsilon^{c''}_{ij} \tag{3.5}$$

where $\epsilon^{c'}_{ij}$ are the constrained strains in an infinite matrix and $\epsilon^{c''}_{ij}$ are the additional strains of the surrounding inclusions. The first constrained strains are

$$\epsilon^{c'}_{ij} = S_{ijkl}\epsilon^t_{kl} \tag{3.6}$$

where S_{ijkl} is the Eshelby tensor. The second constrained strains are calculated from mechanical equilibrium to give

$$\epsilon^{c''}_{ij} = \left(\frac{f}{1-f}\right)\left(\epsilon^t_{ij} - \epsilon^c_{ij}\right) \tag{3.7}$$

where f represents the volume fraction of inclusions. Finally, the total constrained strains are

$$\epsilon^c_{ij} = (1-f)\,S_{ijkl}\epsilon^t_{kl} + f\epsilon^t_{ij} \tag{3.8}$$

The Eshelby tensor coefficients, S_{ijkl}, for ellipsoidal inclusions are

$$S_{3333} = Qc^2 I_{cc} + RI_c \tag{3.9a}$$

$$S_{1111} = S_{2222} = Qa^2 I_{aa} + RI_a \tag{3.9b}$$

$$S_{1133} = S_{2233} = Qc^2 I_{ca} - RI_a \tag{3.9c}$$

$$S_{1122} = S_{2211} = Qa^2 I_{ab} - RI_a \tag{3.9d}$$

$$S_{3311} = S_{3322} = Qa^2 I_{ca} - RI_c \tag{3.9e}$$

where Q and R are given by

$$Q = \frac{3}{8\pi (1 - \nu_{\mathrm{m}})} \tag{3.10a}$$

$$R = \frac{1 - \nu_{\mathrm{m}}}{8\pi (1 - \nu_{\mathrm{m}})} \tag{3.10b}$$

When the particle chains are modeled as an ellipsoid, the coefficients are given by

$$I_a = \frac{2\pi a^2 c}{(c^2 - a^2)^{\frac{3}{2}}} \left[\frac{c}{a} \left(\frac{c^2}{a^2} - 1 \right)^{\frac{1}{2}} - \cosh^{-1} \left(\frac{c}{a} \right) \right] \tag{3.11a}$$

$$I_c = 4\pi - 2I_a \tag{3.11b}$$

$$I_{ca} = I_{cb} = \frac{I_a - I_c}{3 (c^2 - a^2)} \tag{3.11c}$$

$$I_{cc} = \frac{4\pi}{3c^2} - 2I_{ca} \tag{3.11d}$$

$$I_{ab} = \frac{\pi}{3a^2} - \frac{I_{ca}}{4} \tag{3.11e}$$

$$I_{aa} = 3I_{ab} \tag{3.11f}$$

For the spherical inclusions, the coefficients are given by

$$I_a = I_c = \frac{4\pi}{3} \tag{3.12a}$$

$$I_{aa} = I_{cc} = 3I_{ca} = 3I_{cb} = 3I_{ab} = \frac{4\pi}{5a^2} \tag{3.12b}$$

The equivalent transformation strains are found by solving Equations (3.3a), (3.3b), and (3.8). For a spherical inclusion,

$$\epsilon_{11}^t = \epsilon_{22}^t = \frac{(2AK_e + BG_e)\,\epsilon_{11}^{t*} + (AK_e - BG_e)\,\epsilon_{33}^{t*}}{3AB} \tag{3.13a}$$

$$\epsilon_{33}^t = \frac{(2AK_e - 2BG_e)\,\epsilon_{11}^{t*} + (AK_e + 2BG_e)\,\epsilon_{33}^{t*}}{3AB} \tag{3.13b}$$

where the constants A and B are as follows:

$$A = G_m + (f + (1-f)(S_{3333} - S_{1133}))(G_e - G_m) \tag{3.14a}$$

$$B = K_m + (f + (1-f)(S_{3333} + 2S_{1133}))(K_e - K_m) \tag{3.14b}$$

The equivalent transformation strains for an ellipsoidal inclusion with X_3 as the major axis are

$$\epsilon_{11}^t = \epsilon_{22}^t = \frac{(2AK_e + BG_e)\,\epsilon_{11}^{t*} + (AK_e - BG_e)\,\epsilon_{33}^{t*}}{CA - BD} \tag{3.15a}$$

$$\epsilon_{33}^t = \frac{(2DK_e + CG_e)\,\epsilon_{11}^{t*} + (DK_e - CG_e)\,\epsilon_{33}^{t*}}{BD - CA} \tag{3.15b}$$

where the constants A and B are defined in Equations (3.14a) and (3.14b), and C and D are as follows:

$$C = 2K_m + 2(f + (1-f)(S_{3311} + S_{1111} + S_{1122}))(K_e - K_m) \tag{3.16a}$$

$$D = -G_m + (-f + (1-f)(2S_{3311} - S_{1111} - S_{1122}))(G_e - G_m) \tag{3.16b}$$

The constrained strains, $\epsilon_{ij}^{c\prime}$, are calculated from the equivalent transformation strains via Equation (3.8). Finally, using the stress–strain relation, the residual stresses in an inclusion are

$$\sigma_{ij} = \frac{\nu_m E_m}{(1 + \nu_m)(1 - 2\nu_m)}\left(\epsilon^c - \epsilon^t\right)\delta_{ij} + \frac{E_m}{1 + \nu_m}\left(\epsilon_{ij}^c - \epsilon_{ij}^t\right) \tag{3.17}$$

60

Table 3.1: Summary of material properties used in modified Eshelby model for residual stresses.

	E [GPa]	ν	α [°C^{-1}]	f
Polyester	3.8	0.33	75×10^{-6}	0.9776
Terfenol-D	50	0.444	12×10^{-6}	0.0224

3.3 Results

3.3.1 Material properties

In this section, the modified Eshelby model of Section 3.2 is used to analyze residual stresses in the inclusions in the composites described in Section 2.1.2. The necessary material properties and other parameters for the Terfenol-D particulate composites were found in the literature [32] and from the suppliers. A summary of the material properties is presented in Table 3.1. The Terfenol-D particles are 20–40 μm in their longest dimension, so a diameter of 30 μm is assumed when modeling a single particle as a spherical inclusion. A typical composite specimen was studied under an optical microscope and fifty chains of particles were measured. The average chain length in the 3-direction was 955 ± 469 μm and the average width was 110 ± 33 μm. In the ellipsoidal particle chain model, the constants a and c are then 55 μm and 478 μm, respectively. The model geometries are shown in Figure 3.3.

3.3.2 Thermal mismatch

The Terfenol-D composites in this study have a polyester matrix that is cured at room temperature. As the polyester cures, heat is released in the polymerization reaction. Initially, the polymer is a liquid with low viscosity, and the particles in the composite are assumed to be stress-free. Then, at a point known as the gel point, the polymer sets and begins to solidify. When gelation occurs the polymer is at an elevated temperature due to the heat created by the polymerization reaction. The temperature at this point is known as the stress-free temperature. As the composite cools, thermal residual stresses develop. These stresses arise

from the difference in the coefficients of thermal expansion of the two constituent phases. If the assumption of isotropic thermal expansion is made, the transformation strains for the Eshelby model presented in Section 3.2 are

$$\epsilon_{11}^{t*} = \epsilon_{22}^{t*} = \epsilon_{33}^{t*} = (\alpha_{\mathrm{e}} - \alpha_{\mathrm{m}}) \Delta T \tag{3.18}$$

where ΔT is the final temperature minus the stress-free temperature. The residual stresses in the inclusions are compressive and increase with increasing magnitude of ΔT. The residual stresses on a spherical particle are hydrostatic, while the residual stresses on an ellipsoidal particle chain are biased in the chain direction as shown in Figure 3.4.

To determine the stress-free temperature and the gel point of the Terfenol-D composites, a simple experiment was performed. A polyester specimen was manufactured and a type K thermocouple was embedded in the center of the specimen during the cure cycle. All other steps of the manufacturing process were exactly the same as those described in Section 2.1.2 except that no particles were mixed into the resin. LabVIEW$^{\mathrm{TM}}$ was used to acquire the temperature data. Multiple measurements were taken, averaged, and then output to a file every 15 seconds. An identical specimen was manufactured simultaneously, but not placed between the magnets or equipped with a thermocouple. The gel point was recorded as the time when a probe could no longer penetrate the surface of this specimen. The results from the test showed the gel point to be 50 minutes corresponding to a stress-free temperature of 48°C as shown in Figure 3.5. The change in temperature, ΔT, in Equation (3.18) is

$$\Delta T = 24°\mathrm{C} - 48°\mathrm{C} = -24°\mathrm{C}$$

The thermally induced residual stresses from this ΔT for a single spherical inclusion are

$$\sigma_{11}^{\mathrm{th}} = \sigma_{22}^{\mathrm{th}} = \sigma_{33}^{\mathrm{th}} = -8.0 \text{ MPa}$$

and the residual stress for a particle chain are

$$\sigma_{11}^{\text{th}} = \sigma_{22}^{\text{th}} = -5.7 \text{ MPa}$$

$$\sigma_{33}^{\text{th}} = -38.8 \text{ MPa}$$

3.3.3 Chemical shrinkage

Another effect of the polymerization reaction is chemical shrinkage. As the monomers join to form polymer chains and crosslinking occurs between the chains, the volume of polymer decreases. The chemical shrinkage can occur both before and after gelation and can be as large as 20% [28]. Before gelation, the shrinkage causes no stress on the Terfenol-D particles because the polymer relaxes immediately, but after gelation the shrinkage compresses the particles causing the development of residual stresses. The strains associated with volumetric chemical shrinkage are isotropic and calculated via

$$\epsilon_{11} = \epsilon_{22} = \epsilon_{33} = (1 + \Delta V_{\text{ch}})^{\frac{1}{3}} - 1 \tag{3.19}$$

where ΔV_{ch} is the volumetric chemical shrinkage [34]. The transformation strains for the Eshelby model are the shrinkage strains of the inclusion minus the shrinkage strains of the matrix. Since there is no chemical shrinkage of the inclusion, the transformation strains are

$$\epsilon_{11}^{t*} = \epsilon_{22}^{t*} = \epsilon_{33}^{t*} = -\left((1 + \Delta V_{\text{ch}})^{\frac{1}{3}} - 1\right) \tag{3.20}$$

The residual stress state due to chemical shrinkage is hydrostatic pressure on the Terfenol-D particles modeled as spherical inclusions. The pressure increases with higher amounts of shrinkage as shown in Figure 3.6. For the ellipsoidal particle chain, the residual stresses are negative as well, but σ_{33} is almost an order of magnitude larger than σ_{11}.

For the Terfenol-D composites in this study, an experiment was conducted to determine

Table 3.2: Summary of chemical shrinkage experiment results.

Specimen #	a [g]	b [g]	c [g]	SG	$V_f[cm^3]$	$V_i[cm^3]$	ΔV_{ch}
1	4.8882	0.4649	1.6946	1.3361	3.667	3.906	-6.12%
2	4.9054	0.4649	1.7053	1.3384	3.674	3.906	-5.95%

the total volumetric chemical shrinkage. An upper bound to the shrinkage was determined in the experiment, but this bound included both the shrinkage before gelation and the shrinkage afterward. The experiment was conducted according to ASTM standard D 792-91. First, the specimen was weighed in air and its weight (a) was recorded. Then, a wire was suspended from the scale, immersed in water, and weighed (b). Finally, the specimen was suspended by the wire, immersed in the water, and its weight was recorded (c). The specific gravity was calculated via

$$\text{SG} = \frac{a}{a + c - b} \tag{3.21}$$

and the final volume, V_f, was

$$V_f = \frac{a}{\rho_{\text{water}}\text{SG}} \tag{3.22}$$

where ρ_{water} was the density of water at room temperature (997.6 kg/m^3 at 22.5°C). The initial volume, V_i, was determined by measuring the size of the specimen mold. The volumetric chemical shrinkage is

$$\Delta V_{ch} = \frac{V_f - V_i}{V_i} \tag{3.23}$$

Two specimens were tested and the results are shown in Table 3.2. The average volumetric chemical shrinkage was -6.0%. Using the estimate that only half of this shrinkage (-3.0%) occurs after gelation, the chemically induced residual stresses on a single spherical particle are

$$\sigma_{11}^{ch} = \sigma_{22}^{ch} = \sigma_{33}^{ch} = -53.5 \text{ MPa}$$

and for a particle chain are

$$\sigma_{11}^{\text{ch}} = \sigma_{22}^{\text{ch}} = -37.8 \text{ MPa}$$

$$\sigma_{33}^{\text{ch}} = -258.9 \text{ MPa}$$

3.3.4 Magnetostrictive effects

The final mechanism that creates residual stresses is the magnetostrictive effect. Since the specimens are cured between two permanent magnets as discussed in Section 2.1.2, the Terfenol-D particles strain in response to the magnetic field, up to a possible saturation magnetostriction strain of 2.4×10^{-3} in the direction of the field. An assumption of

$$\epsilon_{11}^{\text{mag}} = \epsilon_{22}^{\text{mag}} = -\frac{1}{2}\epsilon_{33}^{\text{mag}} \tag{3.24}$$

is made for the strains in the plane of isotropy. These strains are then used as the transformation strains in the Eshelby model, but must be negative as they are released after the composite is removed from the magnetic field:

$$\epsilon_{33}^{t*} = -\epsilon_{33}^{\text{mag}} \tag{3.25a}$$

$$\epsilon_{11}^{t*} = \epsilon_{22}^{t*} = \frac{1}{2}\epsilon_{33}^{\text{mag}} \tag{3.25b}$$

The magnetostrictive effect on residual stresses is shown in Figure 3.7. In the direction of the applied field (3), the residual stress is positive, but in the plane of isotropy, the residual stresses are negative and smaller. For the manufacturing process described in Section 2.1.2, the magnetic field on the composites is 900 Oe, which corresponds to $\epsilon_{33}^{\text{mag}} = 0.55 \times 10^{-3}$ as shown in Figure 3.8 [21] for a Terfenol-D rod with no prestress. These values of magne-

tostrictive strains correspond to residual stresses of

$$\sigma_{11}^{\text{mag}} = \sigma_{22}^{\text{mag}} = -0.8 \text{ MPa}$$

$$\sigma_{33}^{\text{mag}} = 1.6 \text{ MPa}$$

for the spherical particle model and

$$\sigma_{11}^{\text{mag}} = \sigma_{22}^{\text{mag}} = -0.2 \text{ MPa}$$

$$\sigma_{33}^{\text{mag}} = 12.5 \text{ MPa}$$

for the ellipsoidal particle chain model when only magnetostrictive effects are considered.

3.3.5   Combination of all effects

Combining all of the residual stress mechanisms discussed in Sections 3.3.2, 3.3.3, and 3.3.4 gives transformation strains of

$$\epsilon_{11}^{t*} = \epsilon_{22}^{t*} = (\alpha_{\text{e}} - \alpha_{\text{m}}) \Delta T - (1 + \Delta V_{\text{ch}})^{\frac{1}{3}} + 1 + \frac{1}{2}\epsilon_{33}^{\text{mag}} \tag{3.26a}$$

$$\epsilon_{33}^{t*} = (\alpha_{\text{e}} - \alpha_{\text{m}}) \Delta T - (1 + \Delta V_{\text{ch}})^{\frac{1}{3}} + 1 - \epsilon_{33}^{\text{mag}} \tag{3.26b}$$

for the Eshelby model discussed in Section 3.2. Using the results from the experiments on the Terfenol-D composites in Sections 3.3.2, 3.3.3, and 3.3.4, the total residual stresses and the contribution from each mechanism are summarized in Table 3.3. Chemical shrinkage has the largest effect on the magnitude of the residual stresses for both models. The magnetostrictive effect gives the smallest contribution, and is distinct in that σ_{33} due to the magnetostrictive effect is positive whereas all other residual stress contributions are negative.

Table 3.3: Summary of residual stresses for spherical particle model and ellipsoidal particle chain model.

	spherical particle model		particle chain model	
	σ_{11} (MPa)	σ_{33} (MPa)	σ_{11} (MPa)	σ_{33} (MPa)
Thermal mismatch ($\Delta T = -24°C$)	-8.0	-8.0	-5.7	-38.8
Chemical shrinkage ($\Delta V_{\text{ch}} = -3.0\%$)	-53.5	-53.5	-37.8	-258.9
Magnetostriction ($\epsilon_{33}^{\text{mag}} = 0.00055$)	-0.8	1.6	-0.2	12.5
Total residual stress	-62.3	-59.9	-43.7	-285.2

3.4   Summary

The residual stresses in Terfenol-D particulate composites are derived using a modified Eshelby model. Closed-form analytical solutions are obtained for a spherical particle and a chain of particles modeled as an ellipsoid. Linear isotropic elasticity is assumed for the matrix and the inclusions. The residual stresses are caused by three mechanisms: thermal mismatch, chemical shrinkage of the matrix, and magnetostriction of the particles. Thermal mismatch and chemical shrinkage cause negative residual stresses (Figures 3.4 and 3.6), while the magnetostrictive strains cause a positive residual stress in the direction of the applied field (3) and negative stresses in the plane of isotropy perpendicular to the field (Figure 3.7).

Several experiments were conducted to determine the important parameters for the Terfenol-D particulate composites in this study. The stress-free temperature of the composite was measured to be 48°C (Figure 3.5). The total chemical shrinkage was measured to be -6.0%, and half of that shrinkage (-3.0%) was assumed to occur after gelation. The magnetic field during cure was measured to be 900 Oe, leading to $\epsilon_{33}^{\text{mag}} = 0.00055$ (Figure 3.8). If the assumptions that the magnetostrictive strains in the plane of isotropy perpendicular to the applied field are half of $\epsilon_{33}^{\text{mag}}$ and the volume fraction of Terfenol-D is 0.0224, the residual stresses are

$$\sigma_{11}^{\text{tot}} = \sigma_{22}^{\text{tot}} = -62.3 \text{ MPa}$$

$$\sigma_{33}^{\text{tot}} = -59.9 \text{ MPa}$$

for a single particle modeled as a spherical inclusion and

$$\sigma_{11}^{\text{tot}} = \sigma_{22}^{\text{tot}} = -43.9 \text{ MPa}$$

$$\sigma_{33}^{\text{tot}} = -286.8 \text{ MPa}$$

for a chain of multiple particles modeled as an ellipsoidal inclusion.
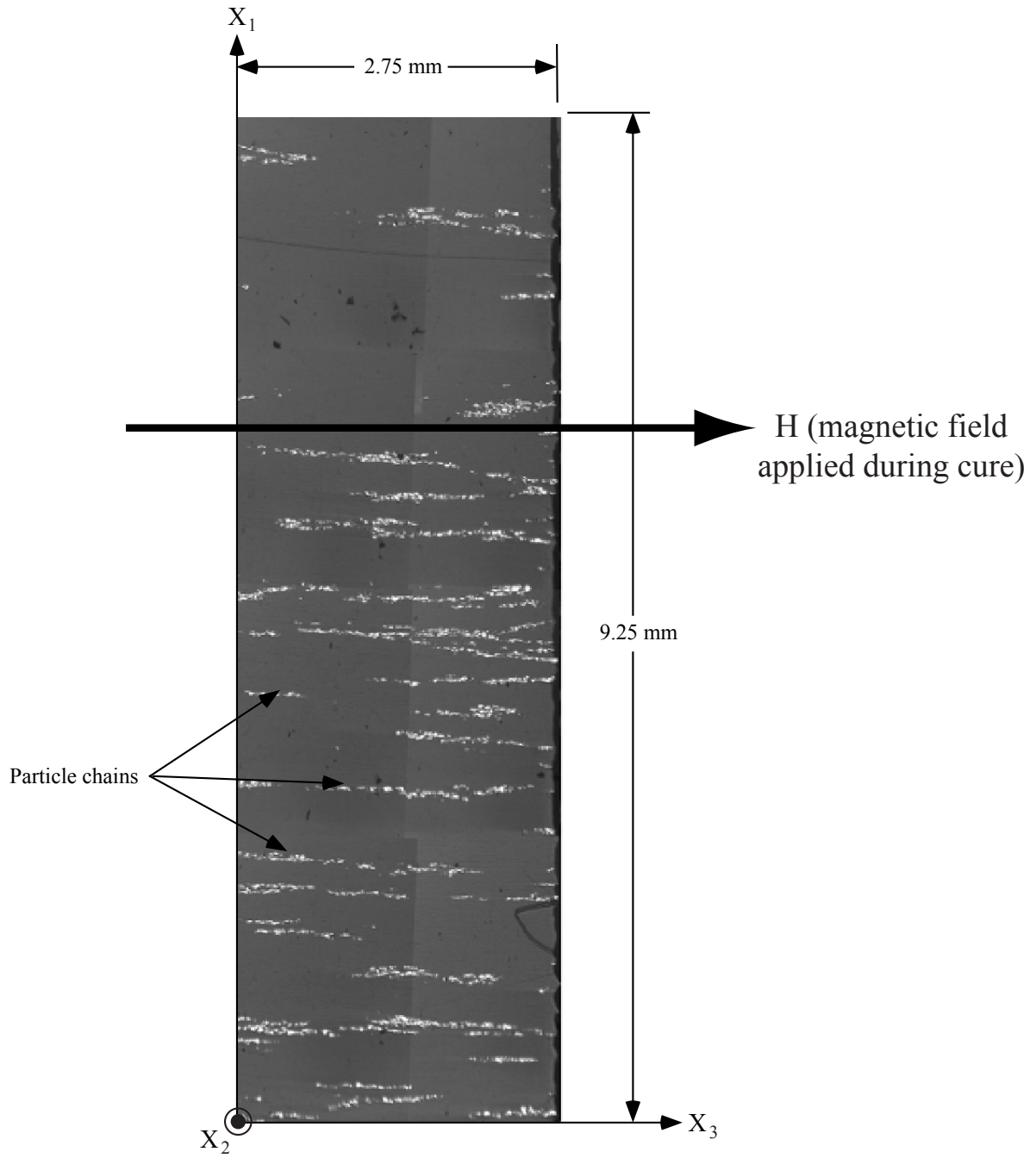
Figure 3.1: Particle chaining phenomenon in Terfenol-D particulate composites cured under a magnetic field in X_3 direction [2].
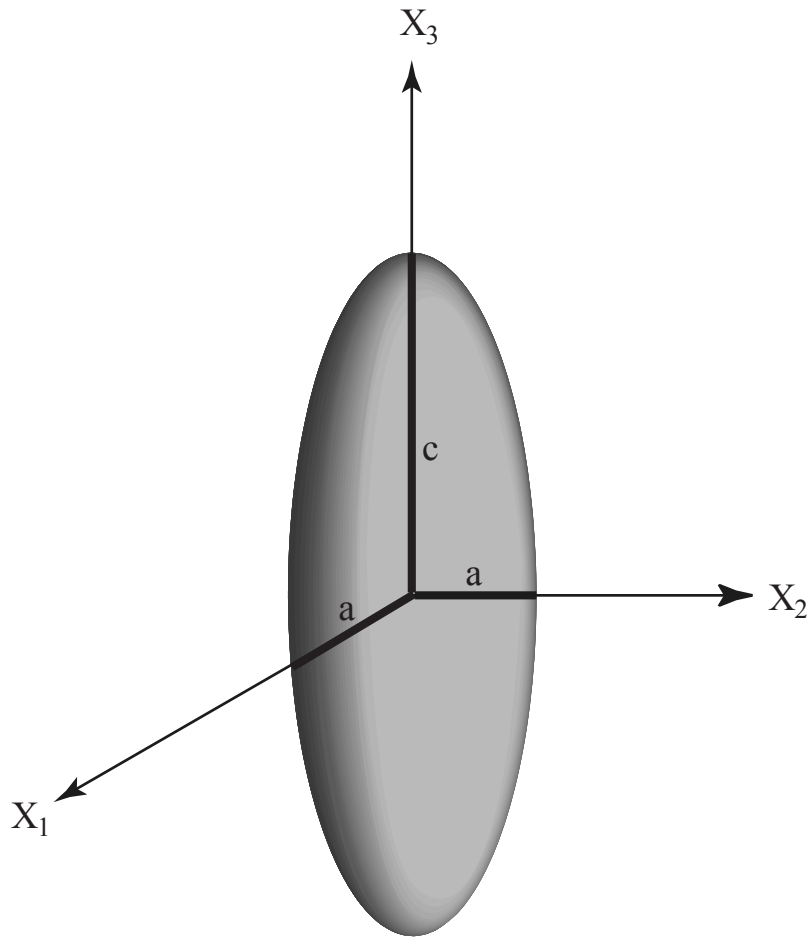
Figure 3.2: Geometry of the ellipsoidal inclusion in the modified Eshelby model.
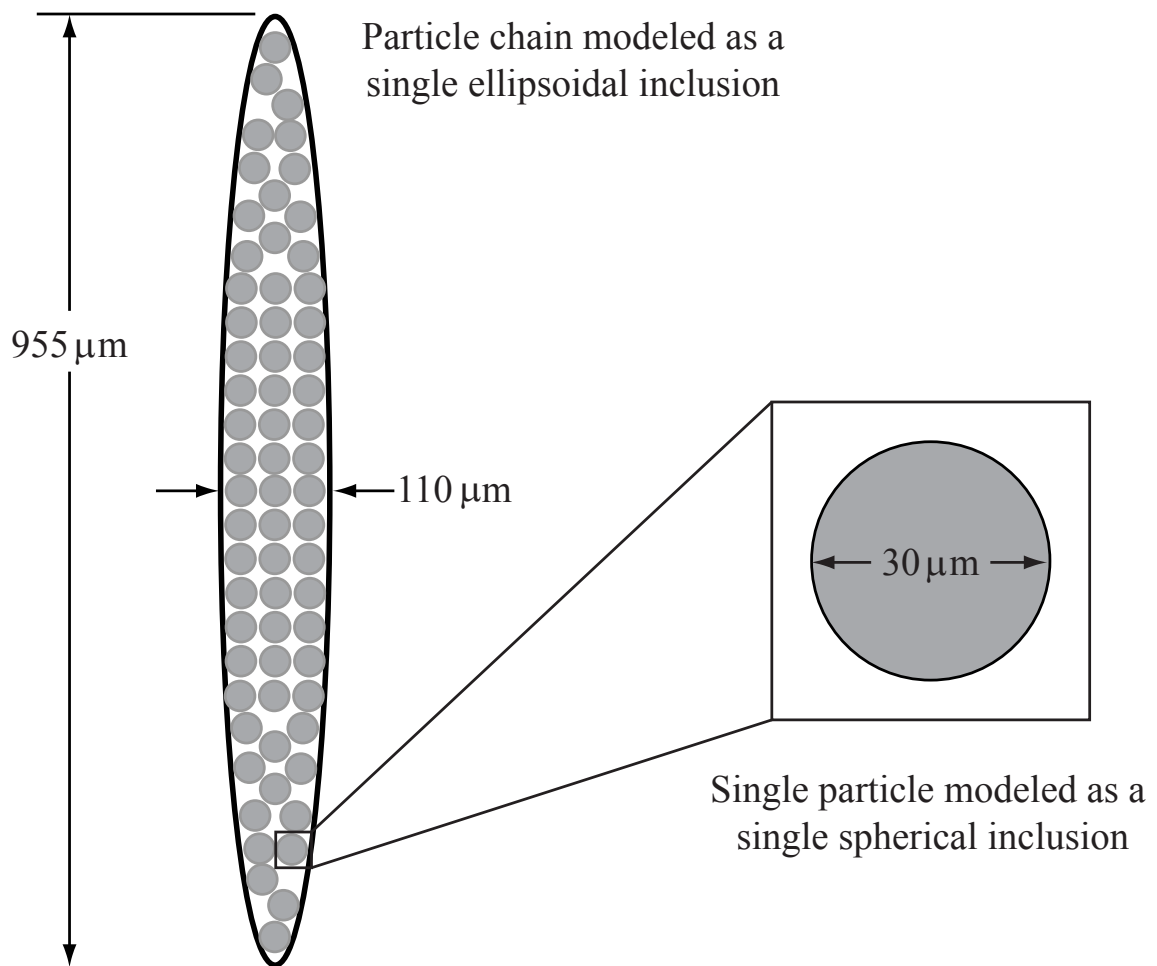
Figure 3.3: Model geometries for the modified Eshelby model.
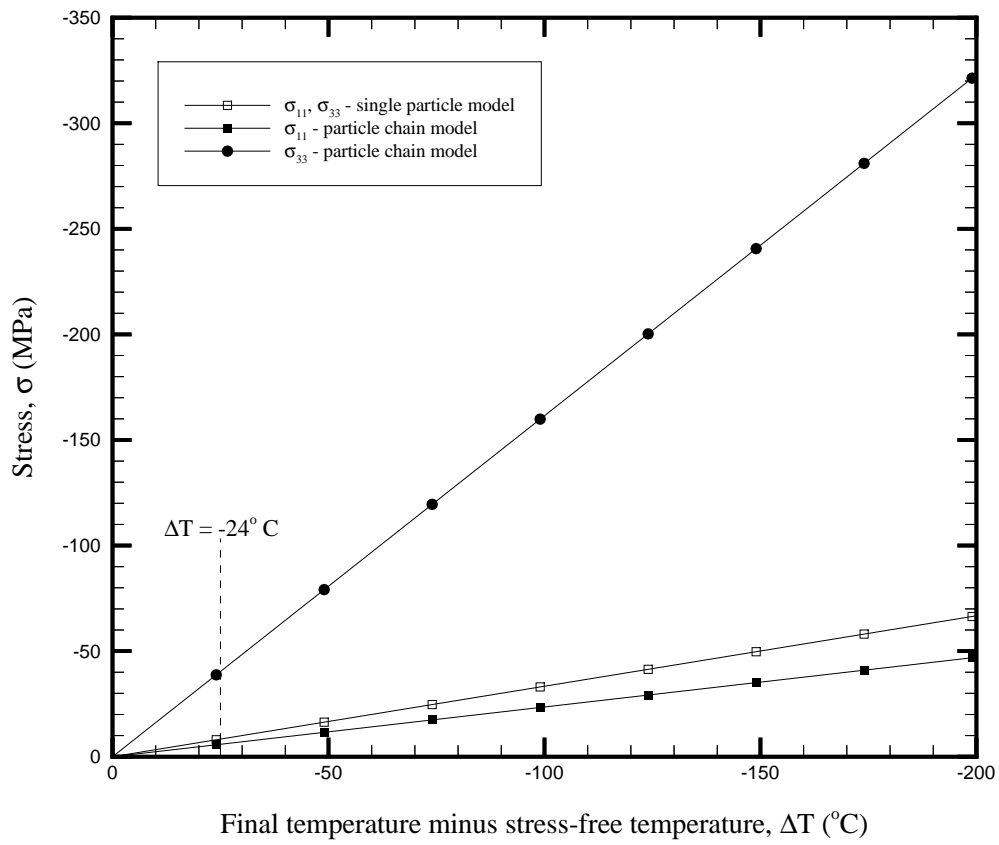
Figure 3.4: Residual stresses from thermal mismatch.
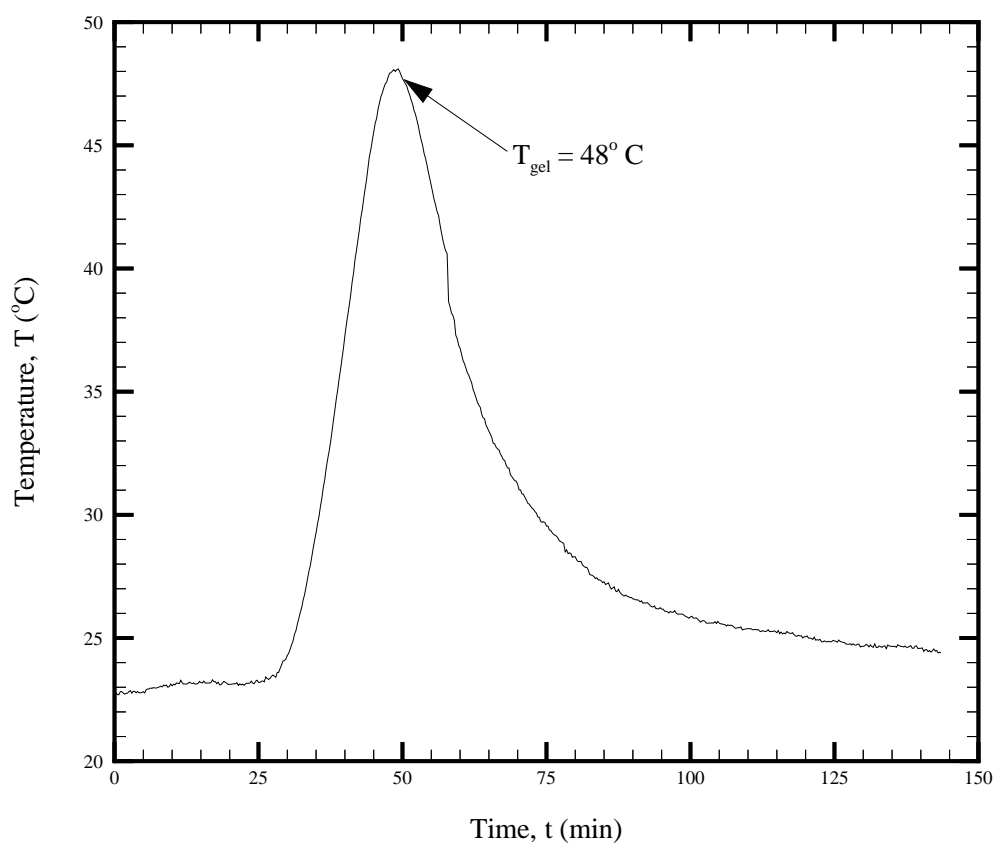
Figure 3.5: Temperature recorded by thermocouple at center of polyester specimen cured at room temperature between permanent magnets at 800 G.
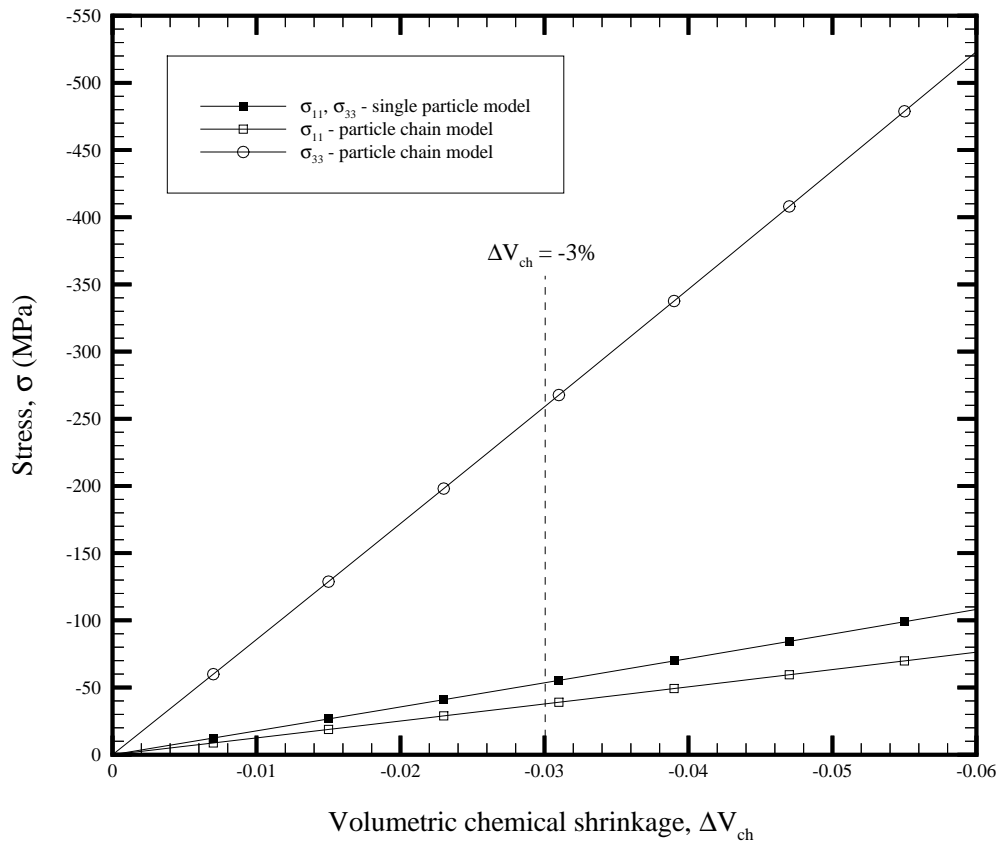
Figure 3.6: Residual stresses from chemical shrinkage.
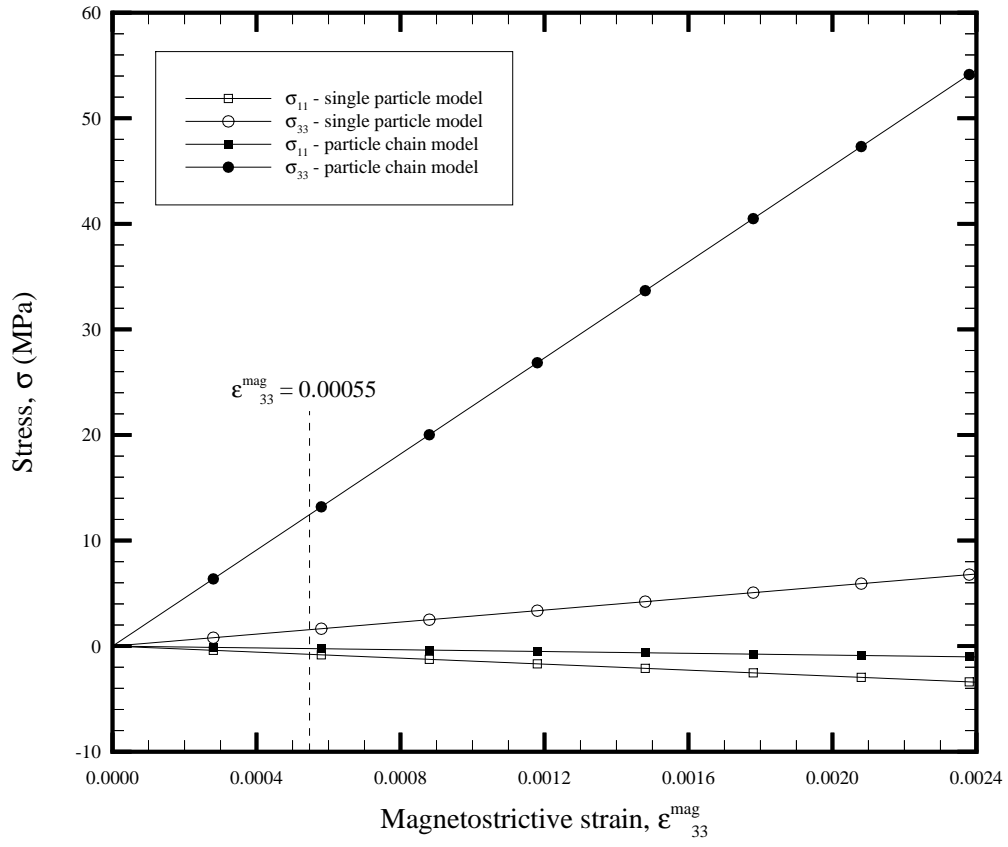
Figure 3.7: Residual stresses from magnetostrictive strains.
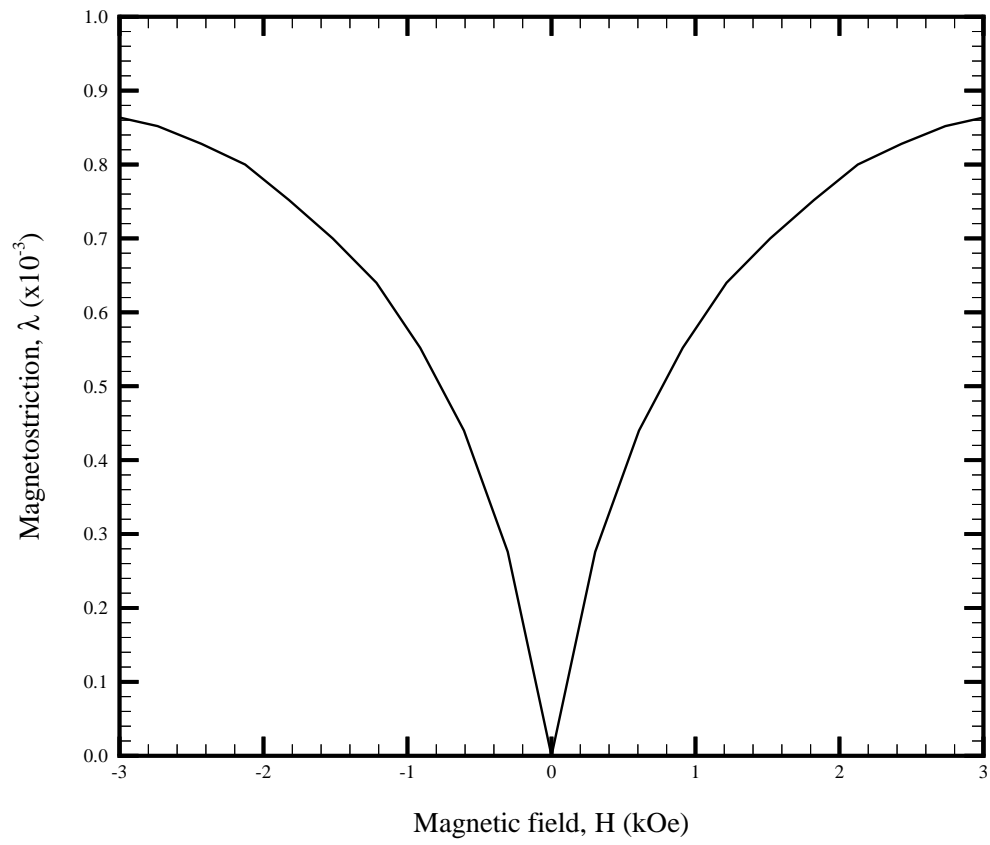
Figure 3.8: Direct effect of magnetostriction for a Terfenol-D rod with no prestress [21].

Chapter 4

Finite element analysis

4.1 Introduction

The use of finite element analysis (FEA) to solve problems in engineering has become quite common with the advent of many commercially available programs. The magnetostrictive phenomenon is not modeled with any of these programs, but there is a strong analogy between piezoelectricity and piezomagnetism. When this analogy is fully exploited, piezomagnetic behavior can be modeled with the piezoelectric analysis available in the commercially available program ABAQUS. The geometry of the model presented here is axisymmetric and consists of a Terfenol-D rod embedded in a polymer cylinder.

4.1.1 Analogy between piezomagnetism and piezoelectricity

The governing equations for piezomagnetism, as discussed in Section 1.2.2, are analogous to those of the piezoelectric effect. The important quantities in piezomagnetism are magnetic flux ($\mathbf{B}$) and magnetic field ($\mathbf{H}$). These are analogous to the relevant quantities of piezoelectricity, electric displacement ($\mathbf{D}$) and electric field ($\mathbf{E}$), respectively. Table 4.1 shows a comparison of the governing equations for piezomagnetism and piezoelectricity [22]. To complete the analogy, Table 4.2 shows a comparison of all the pertinent quantities and corresponding units [23, 22].

Table 4.1: Comparison of piezomagnetic and piezoelectric governing equations.

Piezomagnetism	Piezoelectricity
$S_{ij} = s^H_{ijkl}T_{kl} + d_{kij}H_k$ $B_i = d_{ikl}T_{kl} + \mu^T_{ik}H_k$	$S_{ij} = s^E_{ijkl}T_{kl} + d_{kij}E_k$ $D_i = d_{ikl}T_{kl} + \epsilon^T_{ik}E_k$

Table 4.2: Comparison of piezomagnetic and piezoelectric quantities with units.

Piezomagnetism			Piezoelectricity		
Quantity	Symbol	Units	Quantity	Symbol	Units
Stress	$\mathbf{T}$	N/m^2	Stress	$\mathbf{T}$	N/m^2
Strain	$\mathbf{S}$	-	Strain	$\mathbf{S}$	-
Magnetic flux	$\mathbf{B}$	T	Electric displacement	$\mathbf{D}$	C/m^2
Magnetic field	$\mathbf{H}$	A/m	Electric field	$\mathbf{E}$	V/m
Elastic compliance ($\mathbf{H}$=constant)	$\mathbf{s}^H$	m^2/N	Elastic compliance ($\mathbf{E}$=constant)	$\mathbf{s}^E$	m^2/N
Elastic stiffness ($\mathbf{H}$=constant)	$\mathbf{c}^H$	N/m^2	Elastic stiffness ($\mathbf{E}$=constant)	$\mathbf{c}^E$	N/m^2
Piezomagnetic constant	$\mathbf{d}$	m/A	Piezomagnetic constant	$\mathbf{d}$	m/V
Piezomagnetic constant	$\mathbf{e}$	T	Piezomagnetic constant	$\mathbf{e}$	C/m^2
Permeability ($\mathbf{T}$=constant)	μ^T	H/m	Permittivity ($\mathbf{T}$=constant)	ϵ^T	F/m
Permeability ($\mathbf{S}$=constant)	μ^S	H/m	Permittivity ($\mathbf{S}$=constant)	ϵ^S	F/m
Magnetic scalar potential	ϕ_m	A	Electric potential	ϕ_e	V

Table 4.3: Comparison of interface conditions for piezomagnetism and piezoelectricity.

	Piezomagnetism	Piezoelectricity
Continuity of displacement	$u_i^{\mathrm{I}} = u_i^{\mathrm{II}}$	$u_i^{\mathrm{I}} = u_i^{\mathrm{II}}$
Continuity of normal stresses	$n_i T_{ij}^{\mathrm{I}} = n_i T_{ij}^{\mathrm{II}}$	$n_i T_{ij}^{\mathrm{I}} = n_i T_{ij}^{\mathrm{II}}$
Continuity of scalar potential	$\phi_{\mathrm{m}}^{\mathrm{I}} = \phi_{\mathrm{m}}^{\mathrm{II}}$	$\phi_{\mathrm{e}}^{\mathrm{I}} = \phi_{\mathrm{e}}^{\mathrm{II}}$
Continuity of normal magnetic flux or normal electric displacement	$n_i B_i^{\mathrm{I}} = n_i B_i^{\mathrm{II}}$	$n_i D_i^{\mathrm{I}} = n_i D_i^{\mathrm{II}}$

4.1.2   Boundary conditions

Along with the piezomagnetic governing equations, boundary conditions are necessary to solve a problem. These conditions stem from the equations [10]

$$\nabla \cdot \mathbf{B} = 0 \tag{4.1a}$$

$$\nabla \times \mathbf{H} = 0 \tag{4.1b}$$

which hold for magnetostatic problems when there are no free currents. The electrostatic equations

$$\nabla \cdot \mathbf{D} = 0 \tag{4.2a}$$

$$\nabla \times \mathbf{E} = 0 \tag{4.2b}$$

hold when there are no free charges [10]. These analogous sets of equations lead to important continuity conditions at the interface of two materials. A comparison of the interface conditions for piezomagnetism and piezoelectricity follows in Table 4.3. The superscripts I and II specify the two materials on either side of the interface. The symbol n_i denotes the components of the unit normal to the interface and u_i denotes the components of the displacement vector.

One side of the equation for continuity of normal electric displacement is often set to zero. This condition is called the air-dielectric interface condition and should be used when

the permittivity of one material is much larger than the other [23]. The condition could similarly be applied to the magnetic flux for appropriate permeability values. Although this approximation is a common one, it will not be used in this analysis.

The final boundary condition is setting the scalar potential equal to a reference potential on the surfaces where electrodes are located. Although these electroded surfaces do not physically exist in the piezomagnetic case, the locations are analogous to those where the magnetic potential is set, since the scalar potentials are similarly defined:

$$-\nabla\phi_{\mathrm{e}} = \mathbf{E} \tag{4.3a}$$

$$-\nabla\phi_{\mathrm{m}} = \mathbf{H} \tag{4.3b}$$

4.1.3 Symmetry from polarization

When Terfenol-D is not polarized, it is isotropic, but when it is magnetized (polarized), it develops transverse isotropy about the induced polarization vector [32]. This type of symmetry is analogous to that of piezoelectric polycrystalline ceramics and is classified as crystallographic class $6mm$ in the hexagonal crystal system. The induced polarization vector is typically denoted by X_3. Any direction perpendicular to X_3 can be defined as X_1, since there is isotropy in the plane perpendicular to X_3.

The presence of this transverse isotropy about the 3-axis greatly reduces the number of independent material constants necessary to characterize Terfenol-D fully. The form of the

elastic compliance matrix becomes

$$\begin{bmatrix} s_{11} & s_{13} & s_{13} & 0 & 0 & 0 \\ s_{12} & s_{11} & s_{13} & 0 & 0 & 0 \\ s_{13} & s_{13} & s_{33} & 0 & 0 & 0 \\ 0 & 0 & 0 & s_{44} & 0 & 0 \\ 0 & 0 & 0 & 0 & s_{44} & 0 \\ 0 & 0 & 0 & 0 & 0 & 2(s_{11} - s_{12}) \end{bmatrix}$$

and only five material constants are needed to populate it. It is important to note that the compressed matrix form has been used and the superscripts on s_{ij} have been omitted. The transverse isotropy also modifies the piezomagnetic matrix to the form

$$\begin{bmatrix} 0 & 0 & 0 & d_{14} & d_{15} & 0 \\ 0 & 0 & 0 & d_{15} & -d_{14} & 0 \\ d_{31} & d_{31} & d_{33} & 0 & 0 & 0 \end{bmatrix}$$

with four material constants. Finally, two material constants fully characterize the transversely isotropic permeability matrix

$$\begin{bmatrix} \mu_{11} & 0 & 0 \\ 0 & \mu_{11} & 0 \\ 0 & 0 & \mu_{33} \end{bmatrix}$$

Again, superscripts on μ_{ij} have been omitted since the form of the matrix is the same for both cases. In summary, the matrix form of the piezomagnetic equation with transverse

isotropy about X_3 is

$$
\begin{bmatrix} S_1 \\ S_2 \\ S_3 \\ S_4 \\ S_5 \\ S_6 \\ B_1 \\ B_2 \\ B_3 \end{bmatrix} = \begin{bmatrix} s_{11}^H & s_{12}^H & s_{13}^H & 0 & 0 & 0 & 0 & 0 & d_{31} \\ s_{12}^H & s_{11}^H & s_{13}^H & 0 & 0 & 0 & 0 & 0 & d_{31} \\ s_{13}^H & s_{13}^H & s_{33}^H & 0 & 0 & 0 & 0 & 0 & d_{33} \\ 0 & 0 & 0 & s_{44}^H & 0 & 0 & d_{14} & d_{15} & 0 \\ 0 & 0 & 0 & 0 & s_{44}^H & 0 & d_{15} & -d_{14} & 0 \\ 0 & 0 & 0 & 0 & 0 & 2(s_{11}^H - s_{12}^H) & 0 & 0 & 0 \\ 0 & 0 & 0 & d_{14} & d_{15} & 0 & \mu_{11}^T & 0 & 0 \\ 0 & 0 & 0 & d_{15} & -d_{14} & 0 & 0 & \mu_{11}^T & 0 \\ d_{31} & d_{31} & d_{33} & 0 & 0 & 0 & 0 & 0 & \mu_{33}^T \end{bmatrix} \begin{bmatrix} T_1 \\ T_2 \\ T_3 \\ T_4 \\ T_5 \\ T_6 \\ H_1 \\ H_2 \\ H_3 \end{bmatrix} \tag{4.4}
$$

4.2 Finite element formulation

4.2.1 Preprocessing with PATRAN

The preprocessing for this analysis was performed using PATRAN 6.2. In this software, the geometry is defined first, and then several options for mesh development are available. The user can define mesh seeds with a uniform distribution, a one-way bias, or a two-way bias along curves. The program then generates elements and nodes from these mesh seeds. Two options, *isomesh* and *paver*, are available for the generation of the finite element mesh from the mesh seeds. *Isomesh* is good for small areas where the user wants a very even distribution of elements. *Paver* works wells for a large area that does not need a uniform distribution of the elements. In general, *paver* generates a much smaller total number of elements.

After the mesh is developed, the user must input the boundary conditions, loading conditions, and material properties. PATRAN 6.2 does not have a degree of freedom for electric potential available, so the analysis can not be completed with this program. The final step is to produce an input file for ABAQUS.

Table 4.4: Piezoelectric elements available in ABAQUS.

Plane strain elements	Plane stress elements	Axisymmetric elements	Three-dimensional elements
CPE3E	CPS3E	CAX3E	C3D4E
CPE4E	CPS4E	CAX4E	C3D6E
CPE6E	CPS6E	CAX6E	C3D8E
CPE8E	CPS8E	CAX8E	C3D10E
CPE8RE	CPS8RE	CAX8RE	C3D15E
			C3D20E
			C3D25E

4.2.2 Analysis with ABAQUS

ABAQUS, Version 5.7, has piezoelectric elements and can perform piezoelectric analyses. Procedures are available for both static and dynamic piezoelectric analyses. The piezoelectric analysis procedure uses the equations presented in Table 4.1. Since these equations and the boundary conditions in Table 4.3 have a one-to-one correspondence with those for piezomagnetism, one can effectively model piezomagnetism by substitution of the appropriate quantities into the piezoelectric model via Table 4.2.

There are several types of piezoelectric elements available in ABAQUS. Plane strain, plane stress, and axisymmetric elements are available with 3, 4, 6, and 8 nodes. Three-dimensional elements are available with 4, 6, 8, 10, 15, and 20 nodes. The piezoelectric elements have degrees of freedom for displacement and scalar electric potential. The elements are named according to a certain pattern. The first letter corresponds to the major type of element. For piezoelectric analysis, the first letter is always C, which stands for continuum. The next two characters correspond to plane strain (PE), plane stress (PS), axisymmetric (AX), or three-dimensional ($3D$). The next number is the number of nodes per element. After this number, such options as piezoelectric (E) and reduced integration (R) are included. Table 4.4 shows a complete listing of the piezoelectric elements available in ABAQUS.

Boundary conditions can be applied to displacement and electric potential at any nodes. Displacement degrees of freedom, u_i, are numbered 1, 2, and 3. Electric potential, ϕ_e, is

numbered degree of freedom 9. Loading is applied to an element or an element face. Body force, edge pressure, surface pressure, and electric charge are several of the loading quantities available for a piezoelectric analysis.

The outputs from the piezoelectric analysis include both nodal quantities and integration point quantities. The nodal quantities are electric potential and displacement. Integration point values are not calculated at the nodes of an element, but rather at integration points inside the boundaries of an element. Integration point variables include stress, strain, electric displacement, and electric field.

4.2.3   Modification of the input file

After the PATRAN input file is created, it must be modified before it is ready for piezoelectric analysis in ABAQUS. The input and analysis are treated as piezoelectric by ABAQUS, but if the user enters the appropriate quantities for piezomagnetism, the results will correspond to piezomagnetism. The analogy of relevant quantities is completely described in Table 4.2.

An abbreviated example input file is included in Appendix C. The first item to modify in the PATRAN file is the type of element. In the example file, PATRAN created CAX8 elements. For piezoelectric analysis, the element type must be changed to CAX8E, which denotes axisymmetric, 8-node, piezoelectric elements.

Second, the material properties must be adjusted to include piezomagnetic properties. PATRAN produces the input only for materials with elastic properties, which are presented in the order of Young's modulus followed by Poisson's ratio. The piezomagnetic coefficients can be entered as the d coefficients or the e coefficients described in Table 4.2. If the user enters d coefficients, "type = e" must be included. For e coefficients, "type = s" is the

necessary flag. The format of the entry of the coefficients is

$$d_{111},\ d_{122},\ d_{133},\ d_{112},\ d_{113},\ d_{123},\ d_{211},\ d_{222}$$

$$d_{233},\ d_{212},\ d_{213},\ d_{223},\ d_{311},\ d_{322},\ d_{333},\ d_{312}$$

$$d_{313},\ d_{323}$$

and this pattern must be followed exactly. It is important to note that this order is slightly different from the order of the coefficients in the matrices described in the IEEE Standards [22, 23] and in Equation (1.2).

The permittivity coefficients of piezoelectricity are referred to as dielectric properties in ABAQUS. There is no flag available for constant stress or constant strain, so the user may input whichever properties are appropriate to the analysis. For piezomagnetism, the analogous permeability quantities are input. They can be entered in the order

$$\mu_{11},\ \mu_{12},\ \mu_{22},\ \mu_{13},\ \mu_{23},\ \mu_{33}$$

with "type = aniso". If symmetry exists, "type = ortho" and "type = iso" are possible flags that reduce the number of quantities that need to be included. The permeability values should not be entered as relative permeability with respect to μ_0 but must be entered as true permeability.

PATRAN can not produce boundary conditions for the scalar potential, so the input file must be modified to include these. Electric flux loads must also be input by hand since they do not exist in the initial PATRAN file. Finally, the line "*RESTART, WRITE" must be added to the end of the input file just before "END STEP". This command creates a file from which ABAQUS Post can run.

4.3 Composite cylinder model

4.3.1 Geometry, loading, and boundary conditions

The geometry of concentric cylinders was selected to model a Terfenol-D rod embedded in a polymer matrix. As shown in Figure 4.1, the piezomagnetic rod has a radius that is one-tenth of the outer radius of the polymer cylinder, giving a volume fraction of 1% for the rod. The rod's poling axis is parallel to the axis of the cylinder (2-direction). The loading is a uniform compressive stress of -10 MPa in the 2-direction applied to the ends of the cylinder. Although this geometry is three-dimensional, it can be modeled as axisymmetric by choosing the boundary conditions appropriately.

The left edge of the model is a symmetry boundary, so the normal displacement is constrained and u_1 (displacement in the 1-direction) is set equal to zero along this edge. In the piezoelectric case, the electric potential would be set to zero along the top and bottom of the cylinder. The analogous piezomagnetic boundary condition is to set the magnetic potential, ϕ_m, equal to zero on top and bottom edges. The boundary conditions are also denoted in Figure 4.1.

4.3.2 Material properties

Several assumptions are made about the properties of Terfenol-D in order to complete the model. First, since only a few elastic properties of Terfenol-D are published, the assumption of isotropic elasticity is assumed. A value of 50 GPa is used for Young's modulus [32] and 0.444 is used for the Poisson's ratio [19]. For the piezomagnetic coefficients, the "type = e" flag is used. The value of d_{33} is taken to be 1.48×10^{-10} m/A, using the results from Section 2.4.3.1 and assuming transverse isotropy with respect to the 3-axis. Three more piezomagnetic coefficients are necessary to populate the piezomagnetic matrix. The values for d_{31} and d_{15} are assumed to be $0.5d_{33}$ and $-0.5d_{33}$, respectively. When a magnetostrictive material is poled in the 3-direction, d_{14} has not been experimentally observed [32], so it

Table 4.5: Summary of material properties used in finite element analysis of composite cylinder model.

	E (GPa)	ν	d_{33} (m/A)	d_{31} (m/A)	d_{15} (m/A)	μ_{ii} (H/m)
Polyester	3.8	0.33	1.48×10^{-12}	-0.72×10^{-12}	0.72×10^{-12}	6.28×10^{-6}
Terfenol-D	50	0.444	0	0	0	1.26×10^{-6}

is taken to be zero. ABAQUS defines the radial direction as the 1-direction and the axial direction as the 2-direction for axisymmetric elements. For this model, the axial direction is the poling axis, so the piezomagnetic coefficients must be transformed to the coordinate system of the model shown in Figure 4.1.

4.4 Convergence study

Two different meshes were constructed for the finite element analysis of the composite cylinder. The elements used were axisymmetric 8-node quads (CAX8E) for both meshes. Each node has two displacement degrees of freedom, u_1 and u_2, and a degree of freedom for electric (in this case, magnetic) potential, ϕ_e. Mesh 1, shown in Figure 4.2, has $14,869$ nodes and $4,860$ elements. This mesh was created using the *isomesh* option in PATRAN. A second mesh was constructed with a higher concentration of small elements at the interface. Mesh 2, shown in Figure 4.3, has $17,750$ nodes and $5,813$ elements. The mesh in the Terfenol-D rod was created with *isomesh* and the mesh in the polyester matrix was created with *paver*.

To determine how well each of these meshes modeled the composite cylinder problem, both meshes were run and the results were compared. The shear stress, σ_{12}, and the magnetic flux, B_1, were measured at the interface of the Terfenol-D rod and the polyester matrix. These two quantities should be continuous across the interface as shown in Table 4.3. Using ABAQUS Post, the stress and flux could be determined for each side of the interface. At

the interface, the equations

$$B_1^{\mathrm{T}} - B_1^{\mathrm{P}} = 0 \tag{4.5a}$$

$$\sigma_{12}^{\mathrm{T}} - \sigma_{12}^{\mathrm{P}} = 0 \tag{4.5b}$$

should be true, where the superscript T denotes the Terfenol-D side of the interface and P denotes the polyester side of the interface. For both meshes, the continuity was enforced except at the top and bottom of the model. Figures 4.4 and 4.5 show the difference in B_1 across interface for the lower and upper 10% of the interface, respectively. Both meshes enforce the continuity well up to approximately 5%, where mesh 1 begins to fail. Mesh 2 is able to capture the continuity much better. Only 1% of the interface at the top and bottom of the model has problems with continuity. Similar results are seen for the continuity of shear stress in Figures 4.6 and 4.7. The increased number and decreased size of the elements at the interface in Mesh 2 significantly improved the model results.

4.5   Results

All results shown were obtained using Mesh 2 unless otherwise specified. The variables of interest are the two components of magnetic flux. ABAQUS Post was used to obtain contour plots of the magnetic flux. The model was separated into two parts—the Terfenol-D rod and the polyester matrix, for the contour plots. Figures 4.8 and 4.9 show the magnetic fluxes, B_1 and B_2, in the Terfenol-D rod. The polyester matrix contour plots are given in Figures 4.10 and 4.11. The values for the contours were adjusted for each plot so that more detail could be seen.

The magnetic flux, B_1, is continuous across the interface, so the value remains relatively large in the matrix near the interface, but drops off quickly as the distance from the Terfenol-D rod increases. Only 2 mm from the rod, the flux is nearly zero. The magnetic

flux, B_2, is not continuous across the interface. In the Terfenol-D rod, B_2 is larger than any other magnetic flux in the model. At the midpoint of the rod near the interface, B_2 is around -72 G. Across the interface in the matrix, B_2 is an order of magnitude smaller and of opposite sign. The quick decay of the magnetic flux in the matrix is demonstrated clearly in Figures 4.12 and 4.13. These two figures show the magnetic flux along the line $y = 5$ mm.

To compare the finite element model results with the compression test results presented in Section 2.4.1, the magnetic flux along the interface in the Terfenol-D rod is plotted in Figures 4.14 and 4.15. The trends are similar to the gage length results for the pure Terfenol-D specimen. The "fanning phenomenon" is seen in the magnetic flux, B_1, that is perpendicular to the direction of the magnetization or poling axis. Also, the response, B_1, in the direction of poling is nearly constant in the center of the specimen, but decreases in magnitude slightly before rising dramatically at the ends of the specimen. Both these trends are documented in Figure 2.13.

There is a large difference in the magnitude of the magnetic flux measured in the compression testing and the magnetic flux calculated in the finite element model. The large discrepancy is seen mainly in the magnetic flux along the loading axis, which is also the poling axis. The finite element model uses linear piezomagnetism, which is not a poor assumption, but there is no concept of saturation incorporated into the model. If the piezomagnetic analysis were modified to include saturation behavior, the exaggerated predictions of magnetic flux would disappear.
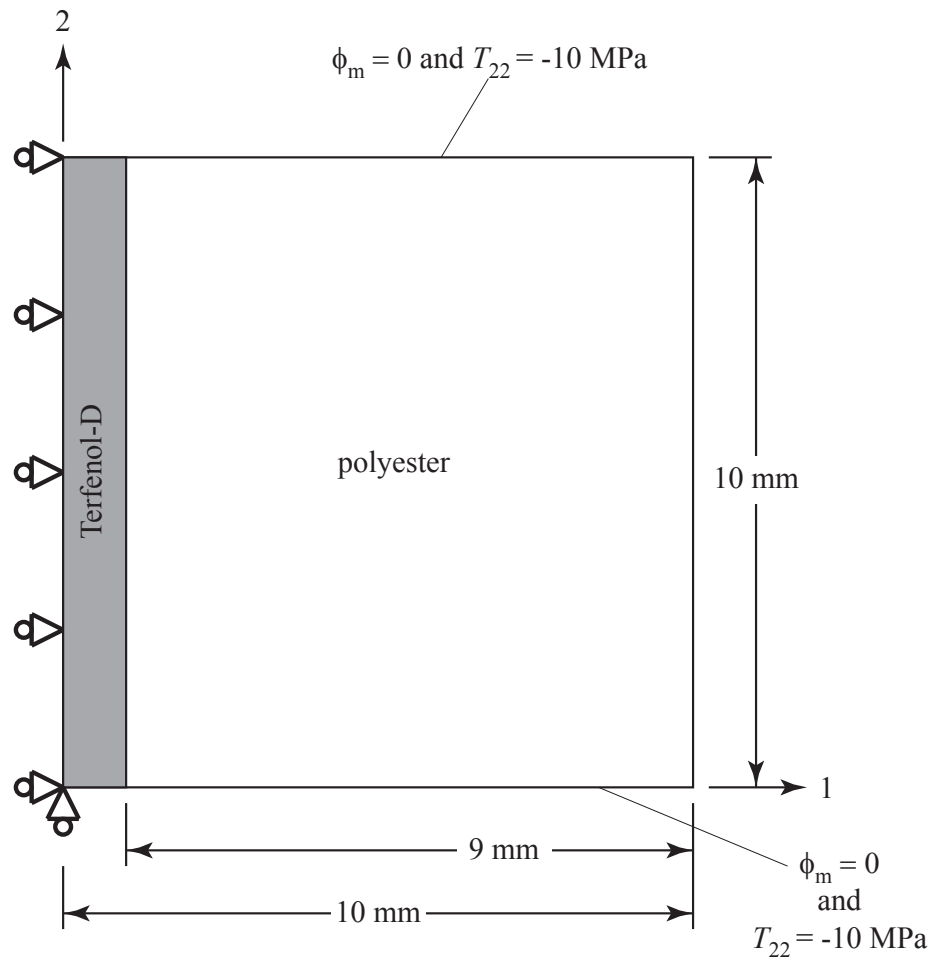
Figure 4.1: Geometry of the composite cylinder model.
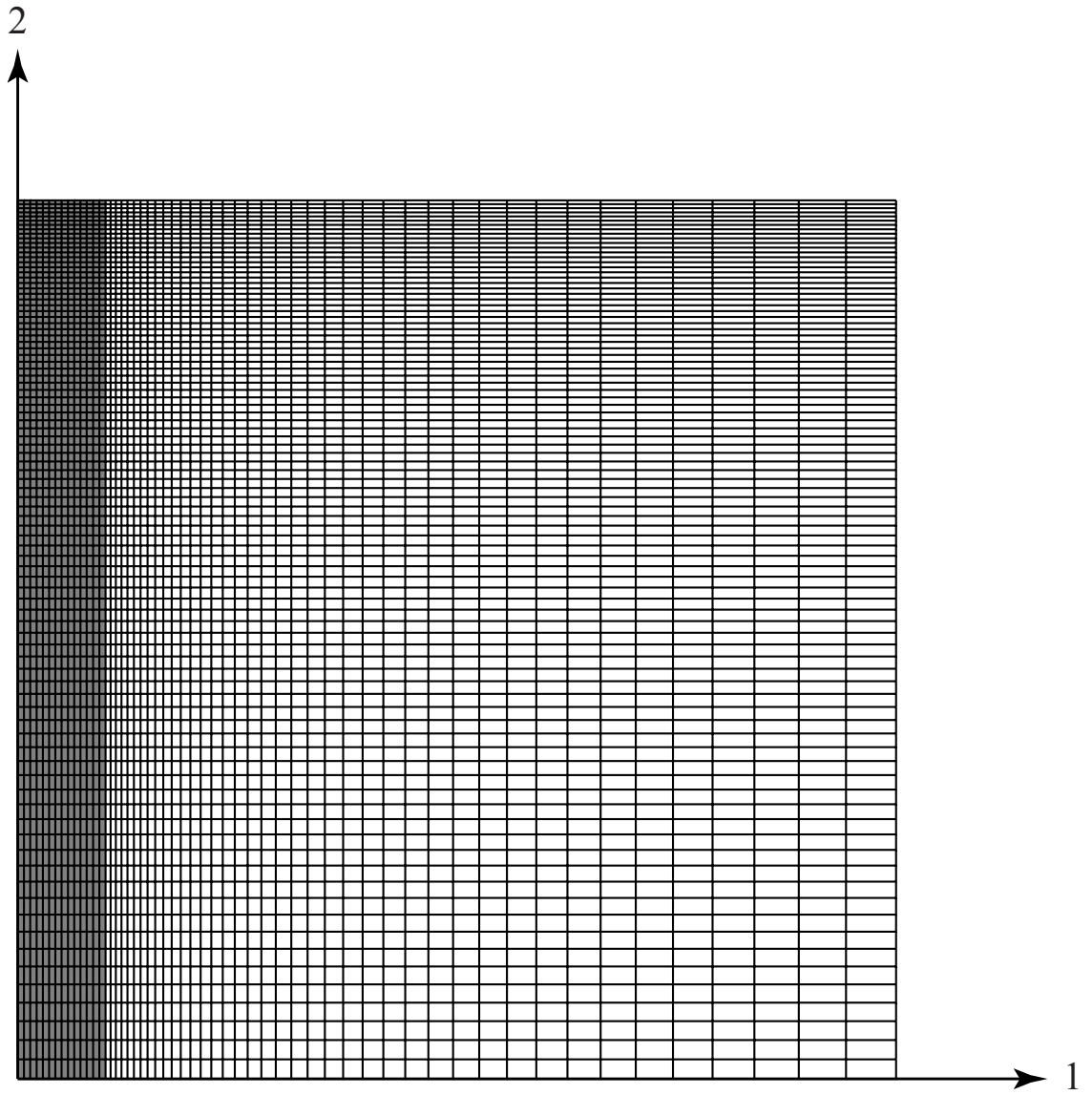
Figure 4.2: Mesh 1 with $14,869$ nodes and $4,860$ elements.

91
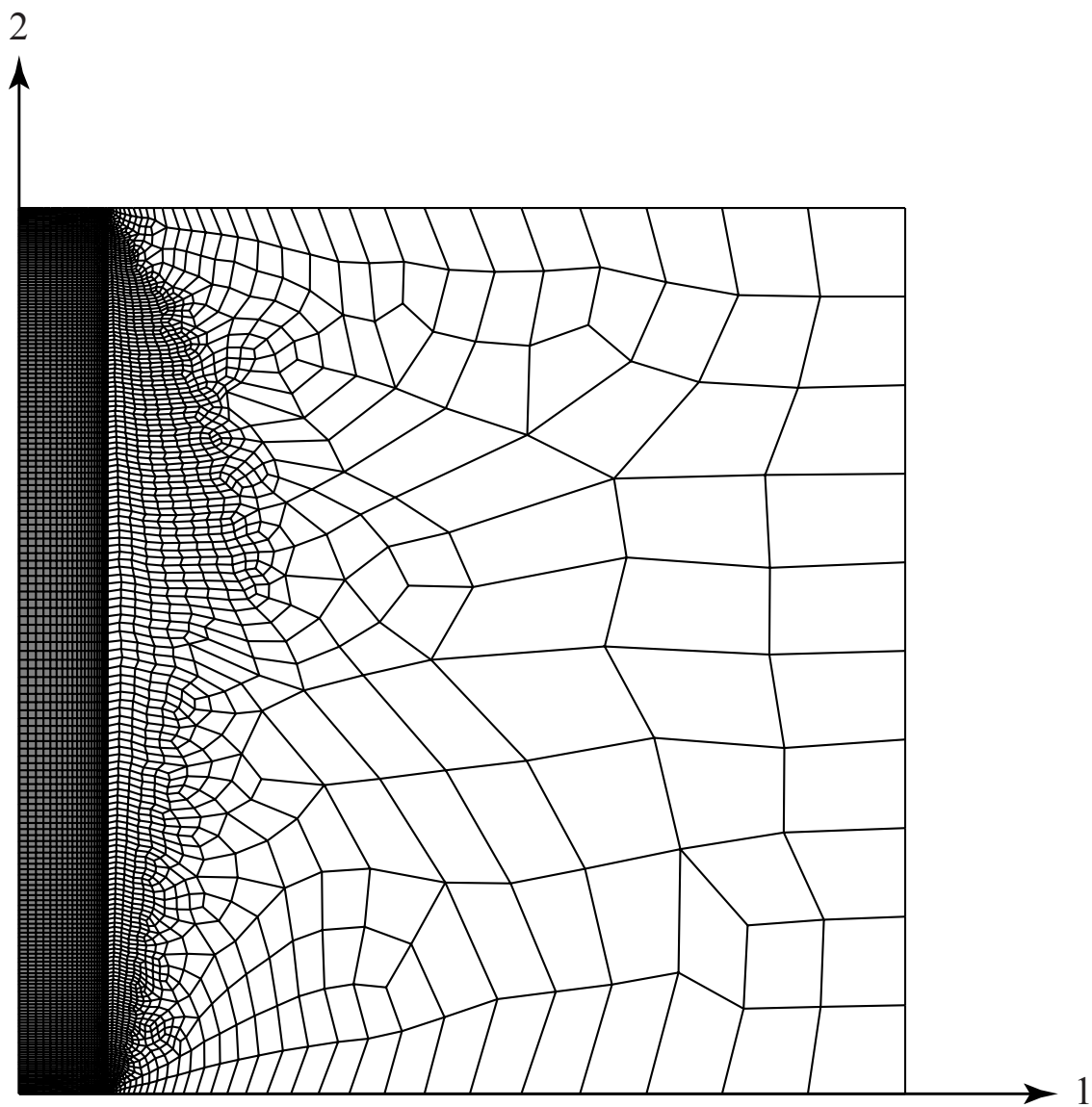
Figure 4.3: Mesh 2 with $17,750$ nodes and $5,813$ elements.
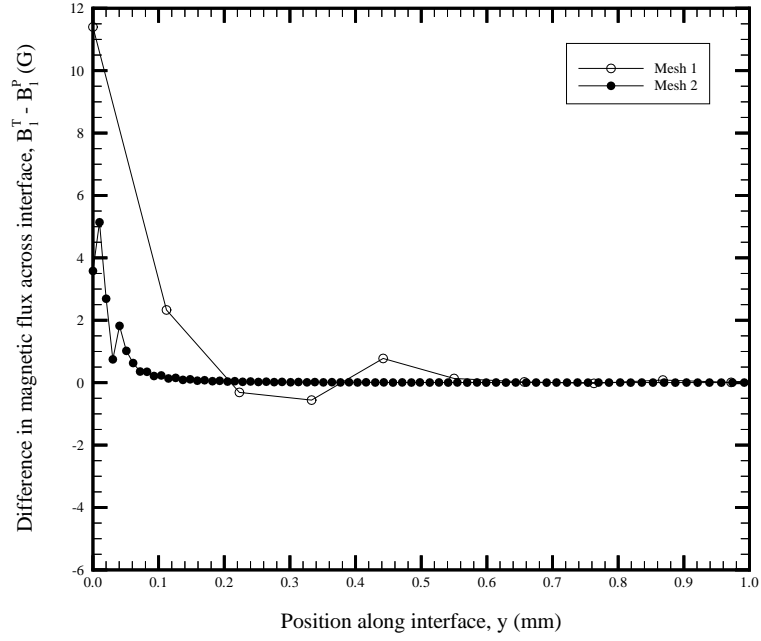
Figure 4.4: Difference in magnetic flux, B_1, across interface at lower 10% of the composite cylinder model.
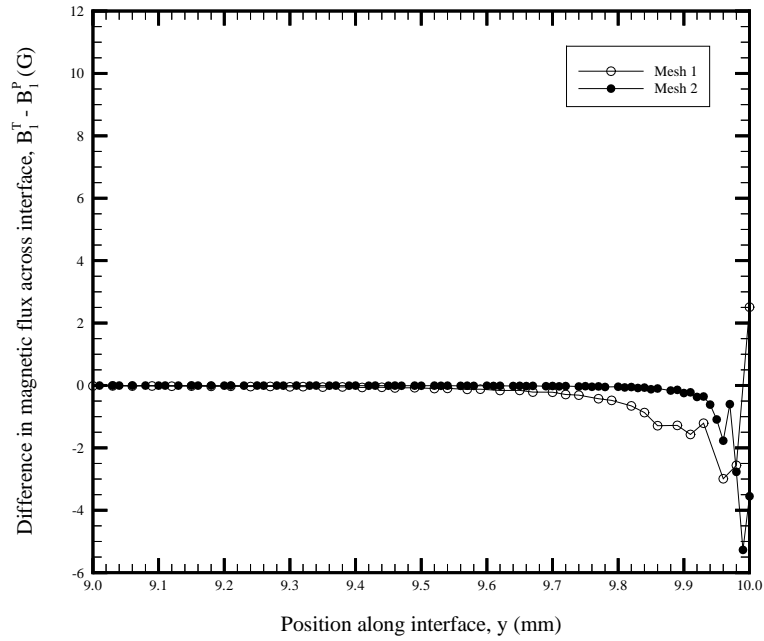
Figure 4.5: Difference in magnetic flux, B_1, across interface at upper 10% of the composite cylinder model.
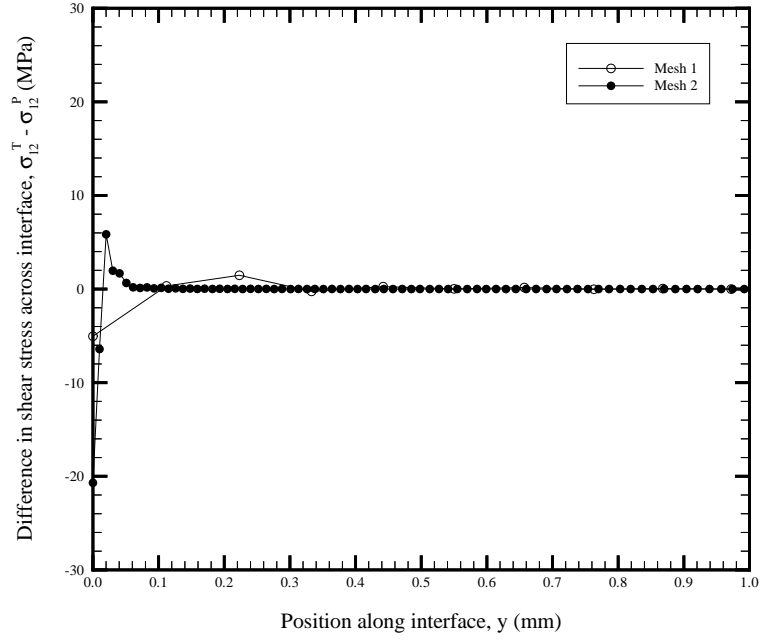
Figure 4.6: Difference in shear stress, σ_{12}, across interface at lower 10% of the composite cylinder model.
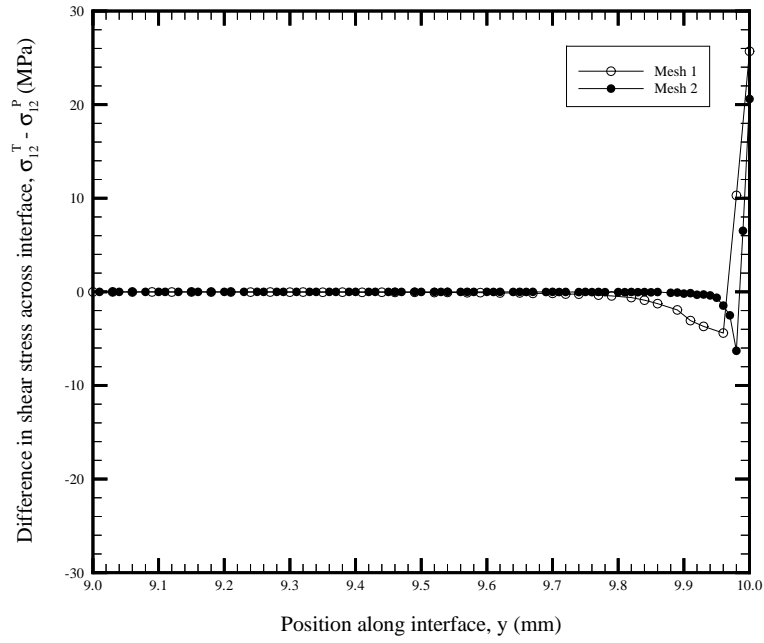
Figure 4.7: Difference in shear stress, σ_{12}, across interface at upper 10% of the composite cylinder model.

94
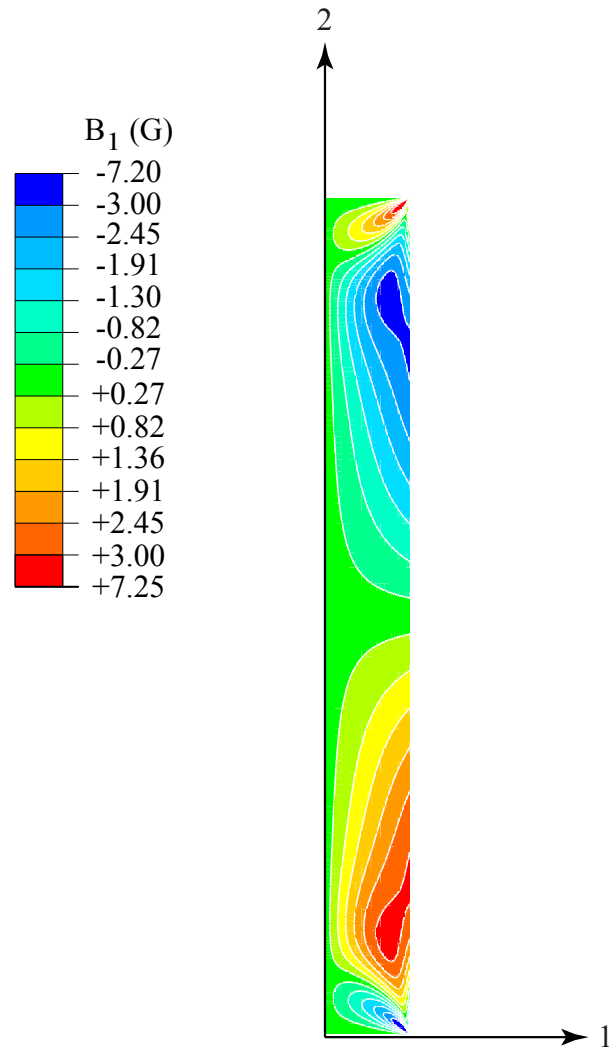
Figure 4.8: Contour plot of the magnetic flux, B_1, in the Terfenol-D rod of the composite cylinder model.
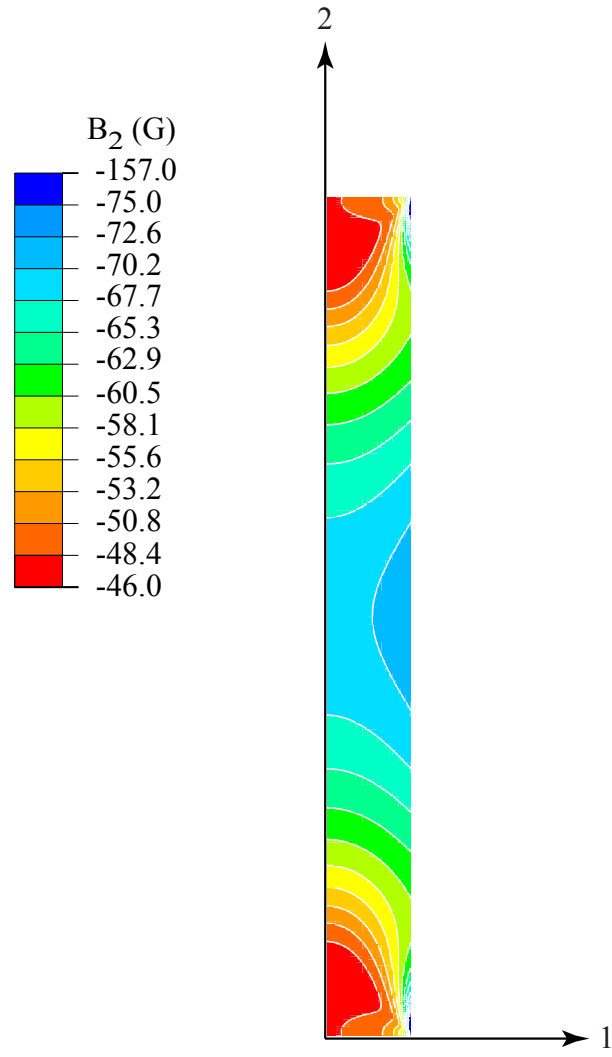
Figure 4.9: Contour plot of the magnetic flux, B_2, in the Terfenol-D rod of the composite cylinder model.

96
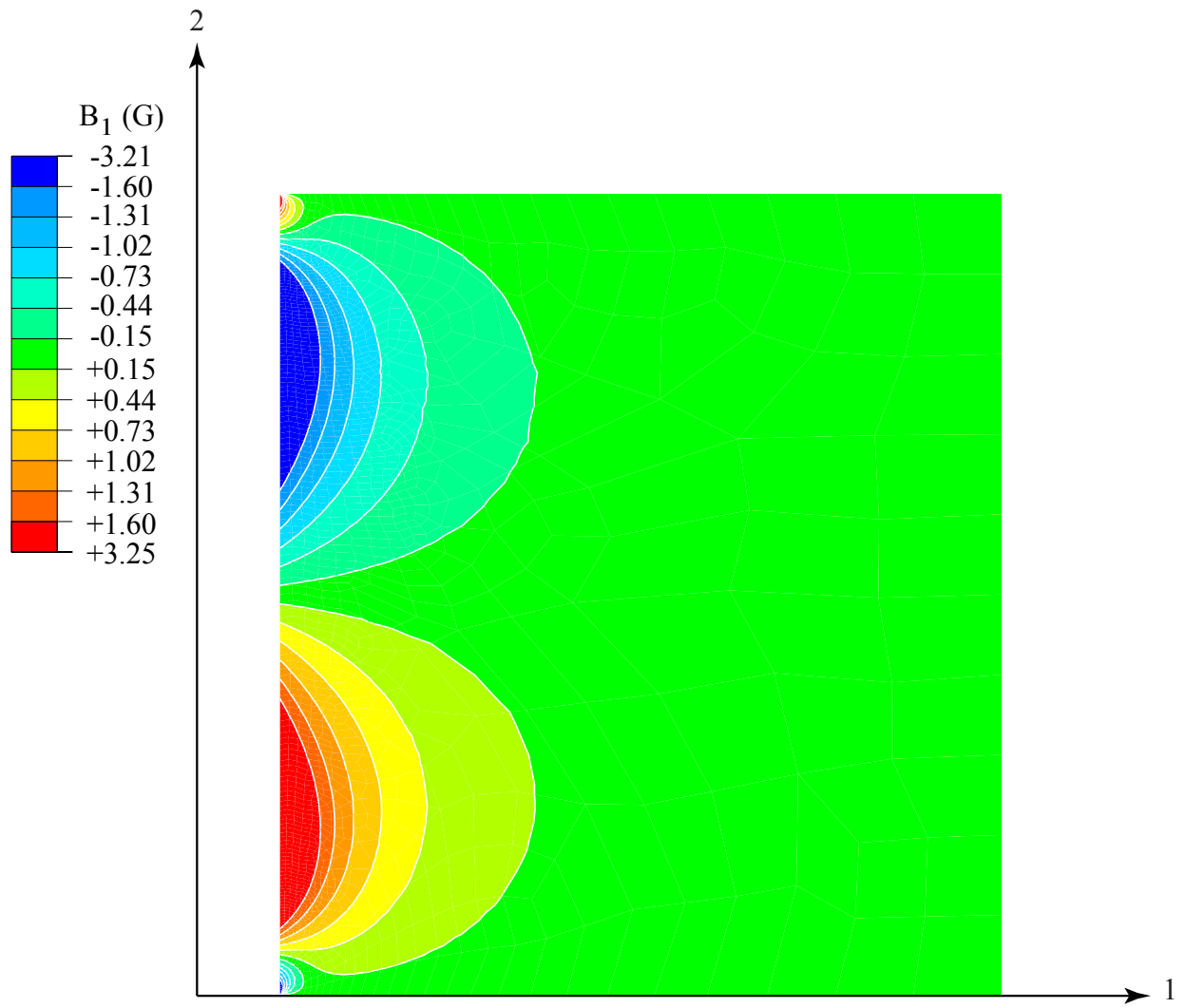
Figure 4.10: Contour plot of the magnetic flux, B_1, in the polyester matrix of the composite cylinder model.
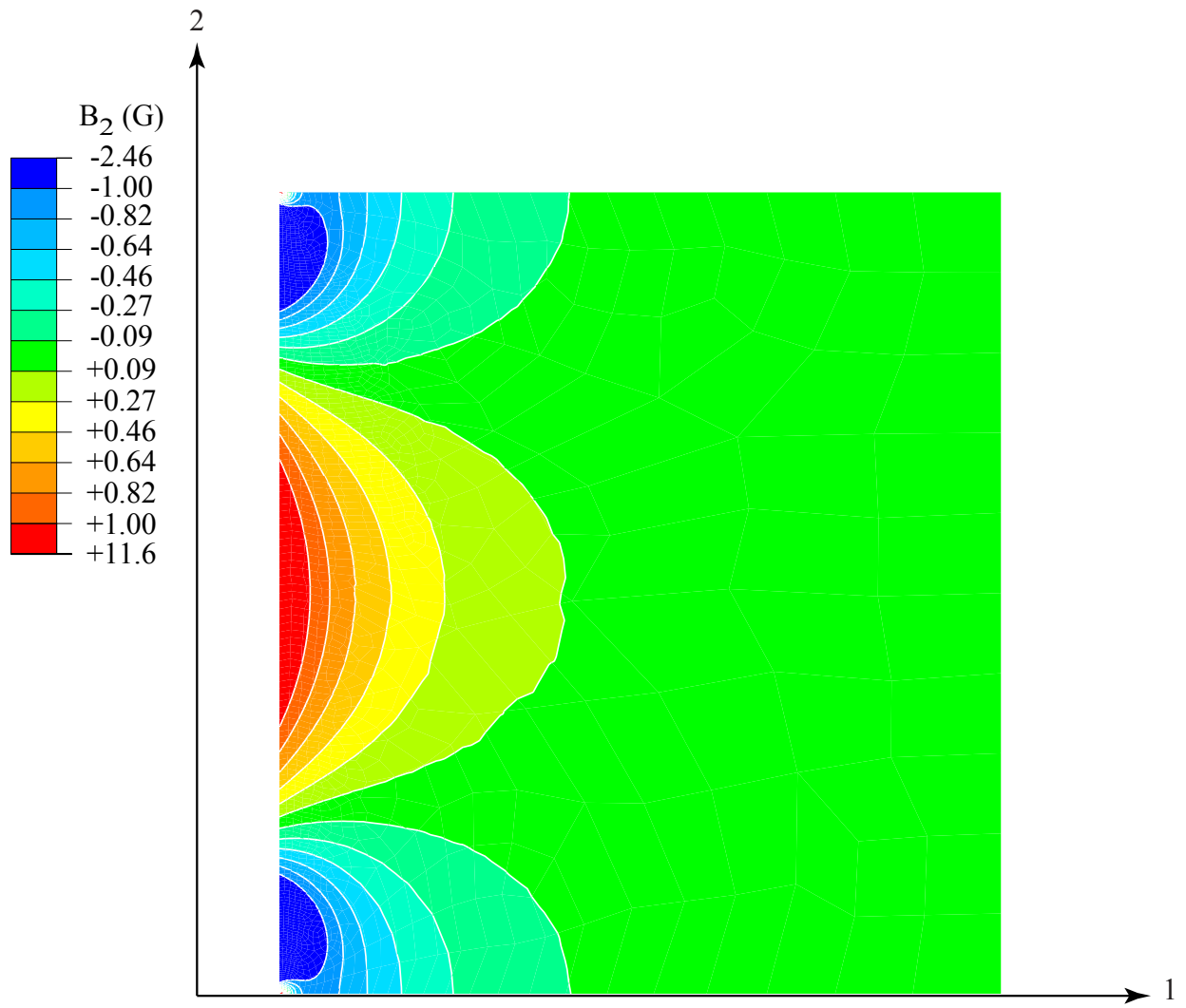
Figure 4.11: Contour plot of the magnetic flux, B_2, in the polyester matrix of the composite cylinder model.
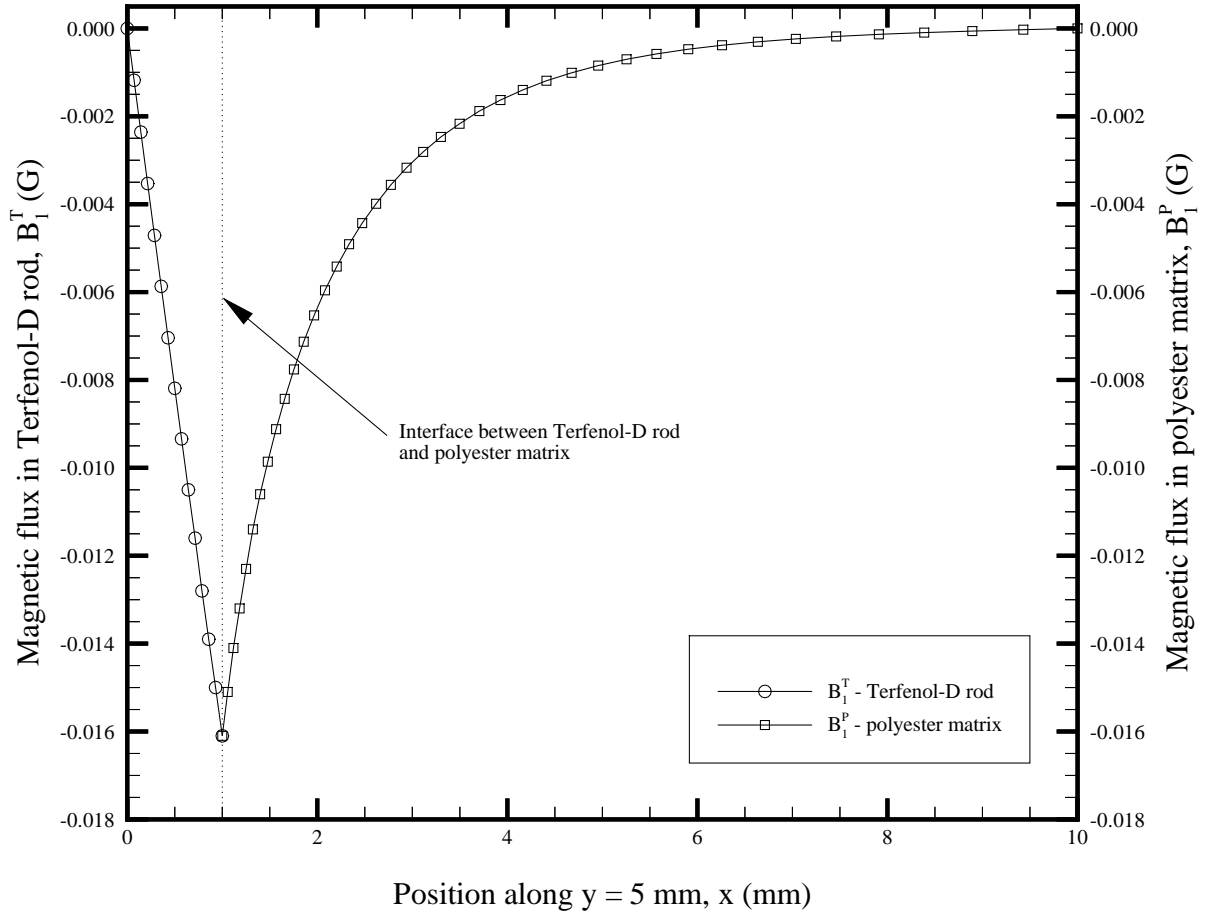
Figure 4.12: The magnetic flux, B_1, along the line $y = 5$ mm of the composite cylinder model.
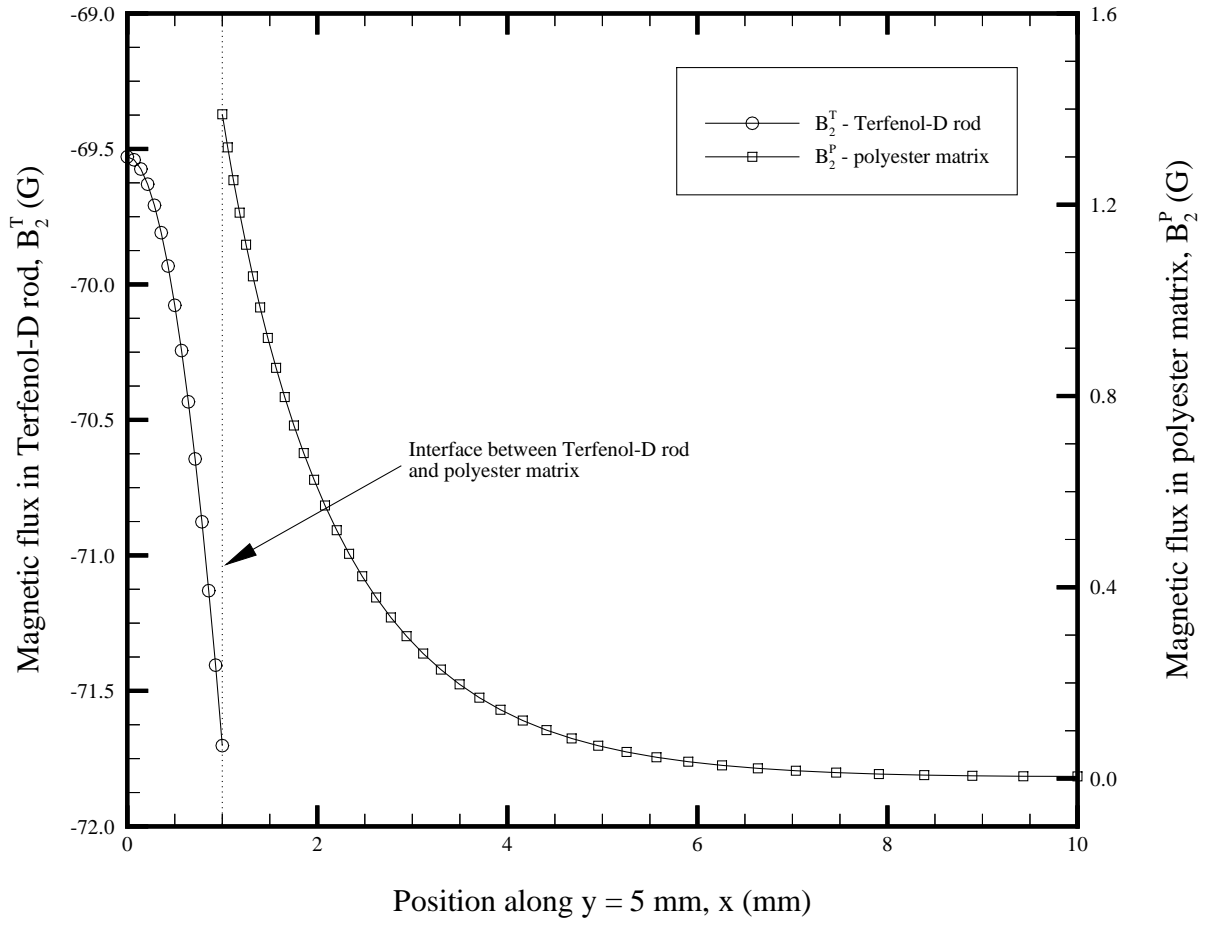
Figure 4.13: The magnetic flux, B_2, along the line $y = 5$ mm of the composite cylinder model.
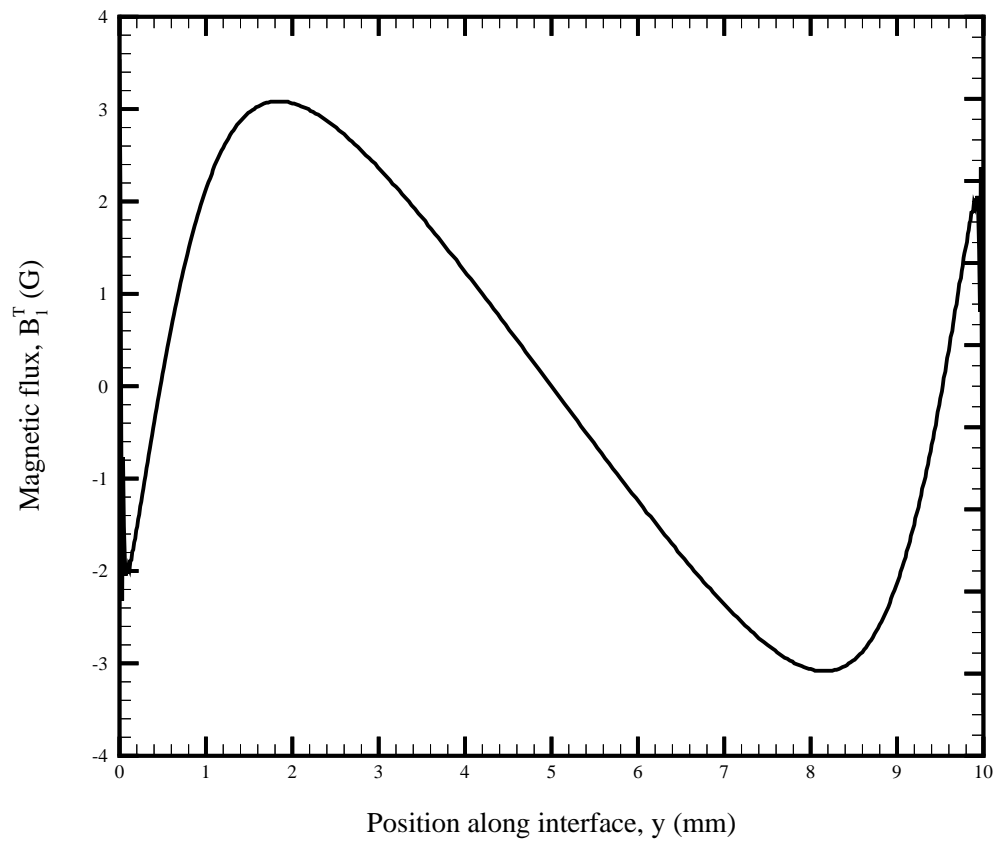
Figure 4.14: Magnetic flux, B_1^T, along the interface in the Terfenol-D rod.
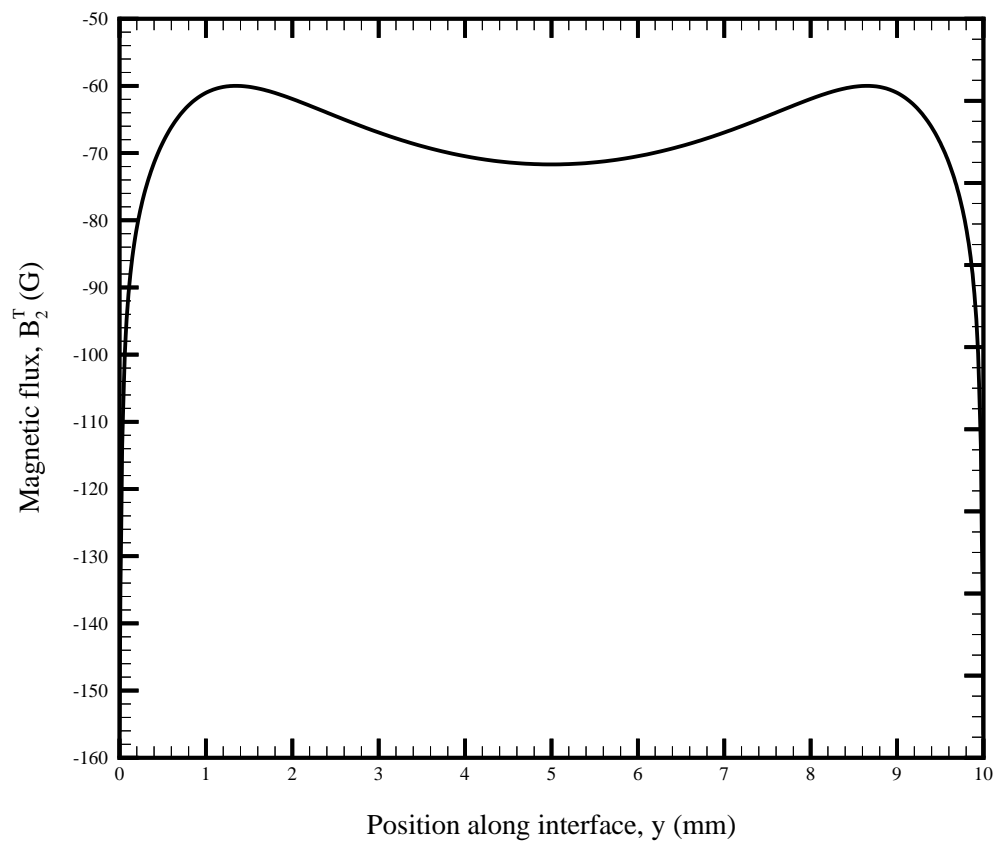
Figure 4.15: Magnetic flux, B_2^T, along the interface in the Terfenol-D rod.

Chapter 5

Summary and conclusions

The increasing use of composite materials in structural applications has led to a need to develop new structural health monitoring techniques. Tagging of a structure with a smart material phase is a viable option. The work reported in this thesis was undertaken to understand the magnetomechanical behavior of Terfenol-D and Terfenol-D particulate composite to further the possibility of composites tagged with the magnetostrictive material, Terfenol-D.

Uniaxial compression testing was conducted on a pure Terfenol-D specimen and several Terfenol-D particulate composites. The composites consisted of a polyester matrix and 2.2% volume fraction of Terfenol-D particulates. Different combinations of curing magnetic flux and annealing magnetic flux were studied. Chaining of the particles was seen whether the specimen was cured with a flux through its length or its width. The three components of magnetic flux were measured with a Hall probe over the gage length of each specimen under uniaxial compressive loading. Results showed that maximum responses occurred when the maximum number of domains were oriented in the direction of the applied compressive stress. It was shown that if the domains are initially aligned in the direction of the compressive stress, they rotate away from this axis as the stress increases. Also, a "fanning phenomenon" was observed that could be explained by observing the magnetic field lines of a uniformly magnetized cylinder.

Piezomagnetic coefficients were measured for the Terfenol-D specimen and the compos-

ites. The largest piezomagnetic coefficient measured was d_{33} (1.48×10^{-10} m/A) for the pure specimen. This value is much lower than the values reported in the literature for the direct effect. Saturation behavior was observed for the pure specimen at stresses as low as -2 MPa. The values of the piezomagnetic coefficients were at least two orders of magnitude smaller for the Terfenol-D composites. The largest d_{33} coefficient measured for a Terfenol-D composite was 7.86×10^{-12} m/A. Saturation was not always reached in the Terfenol-D composites tested.

Cyclic testing was conducted on the Terfenol-D composites. First, a specimen was magnetically annealed. Then, it was loaded and unloaded in compression. The loading and unloading cycle was repeated until a stable response was seen without any further annealing. It was shown that as few as 3 cycles were necessary to reach a stable response. The cyclic testing showed that increasing the magnitude of the curing magnetic flux increased both the initial and the stable responses. On the other hand, increasing the annealing magnetic flux increased only the initial magnetic response.

A possible explanation for the absence of the saturation behavior in the composites is that the residual stresses are quite high. To investigate the residual stress state, a modified Eshelby model was developed. Thermal mismatch, chemical shrinkage, and magnetostrictive strains were all included in the Eshelby model. Two different geometries were studied: a single particle modeled as a spherical inclusion and a chain of particles modeled as an ellipsoidal inclusion.

A finite element analysis was conducted on a composite cylinder in compression using the piezoelectric analysis available in ABAQUS. Results from the finite element analysis showed the same "fanning phenomenon" seen in the compression tests. Also, the magnetic flux change was largest in the direction of the poling axis, just as in the compression testing. The limitation to using the finite element analysis is that saturation behavior is not currently incorporated into the governing equations. The compression testing of the pure Terfenol-D rod showed that saturation occurred at very low stresses, so the finite element analysis greatly

overpredicted the magnetic response observed in experiments.

This research could be improved with a better magnetic flux sensing device. Such a device would simultaneously measure all three components of the magnetic flux at the same point. Unfortunately, the measurements of flux in this research were not all taken at the same distance from the surface of the specimen. It was shown that the magnetic flux measured is strongly affected by the distance from the surface of the specimen. Calculations of maximum magnetic flux change and piezomagnetic coefficients should be compared carefully as some of the measurements are smaller since they were taken farther from the surface of the specimen.

The finite element analysis could be improved by incorporating saturation behavior into the governing equations used in the piezoelectric analysis. Also, it would be interesting to include the residual stresses predicted by the modified Eshelby model. These two modifications would probably improve the correlation between the experimental results and the finite element analysis results.

Appendix A

Gage length characterization results
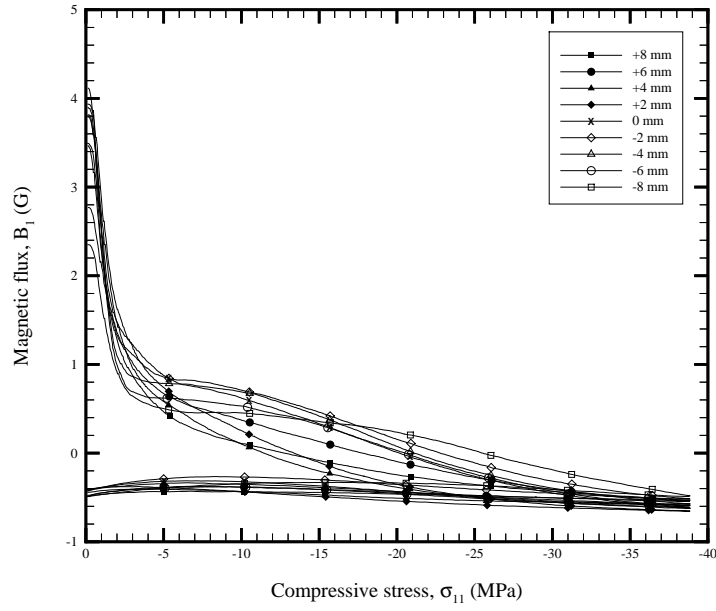
Figure A.1: Magnetic flux ,B_1, over the gage length of pure Terfenol-D specimen, annealing flux of -800 G in 1–direction applied before testing at each position.
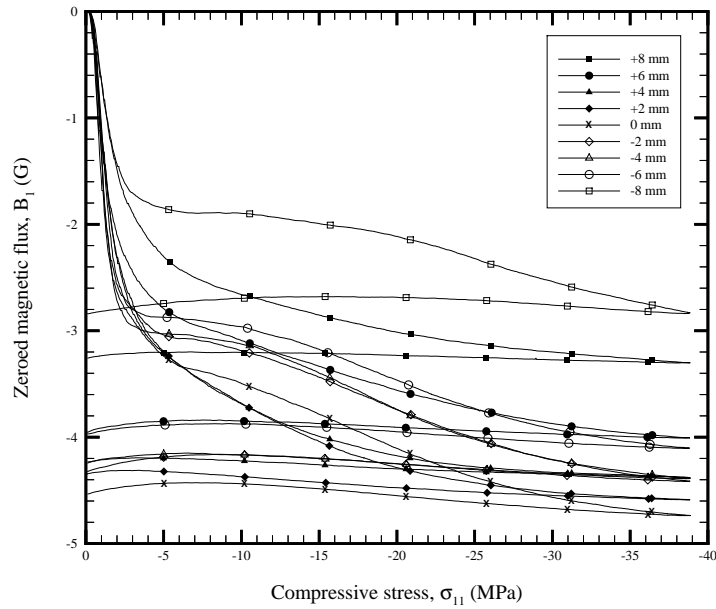
Figure A.2: Zeroed magnetic flux, B_1, over the gage length of pure Terfenol-D specimen, annealing flux of -800 G in 1–direction applied before testing at each position.
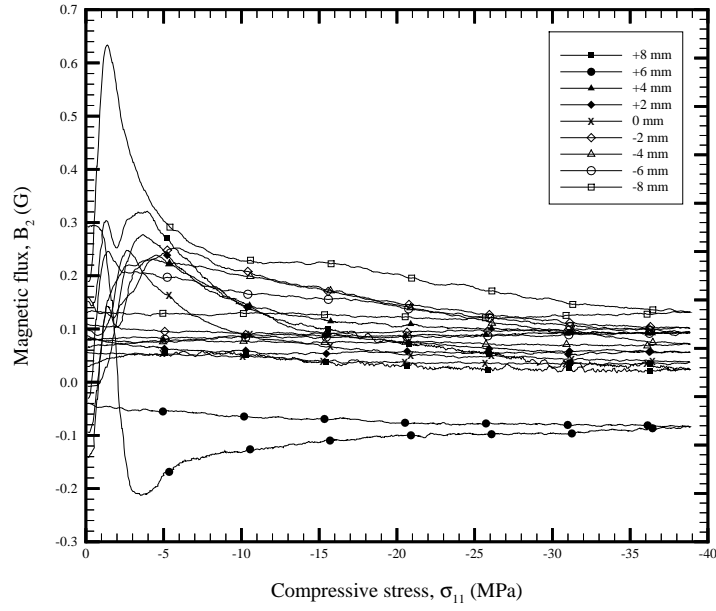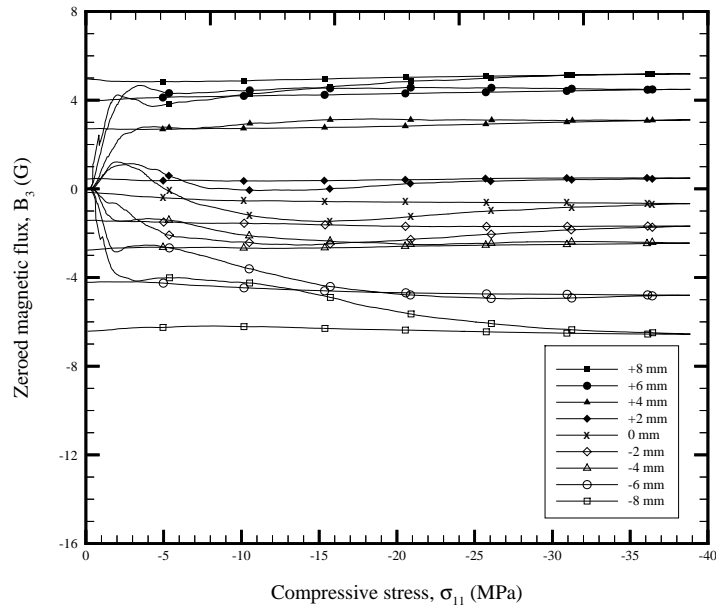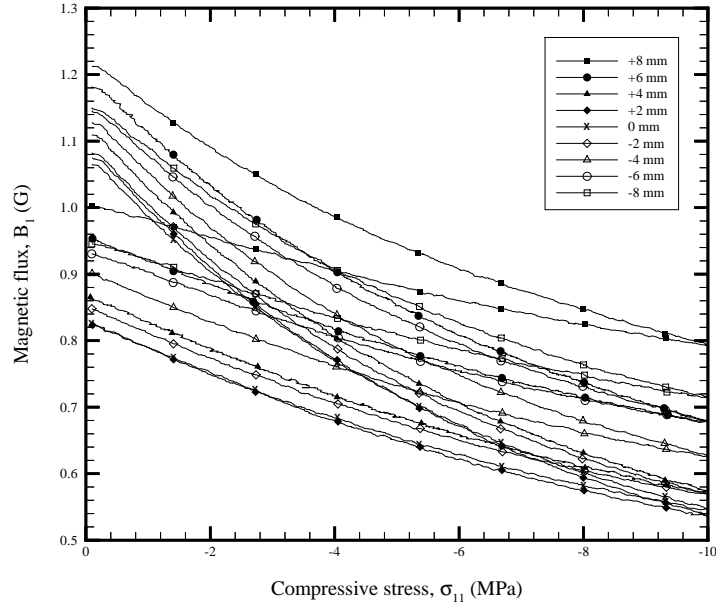
Figure A.3: Magnetic flux, B_2, over the gage length of pure Terfenol-D specimen, annealing flux of -800 G in 1–direction applied before testing at each position.
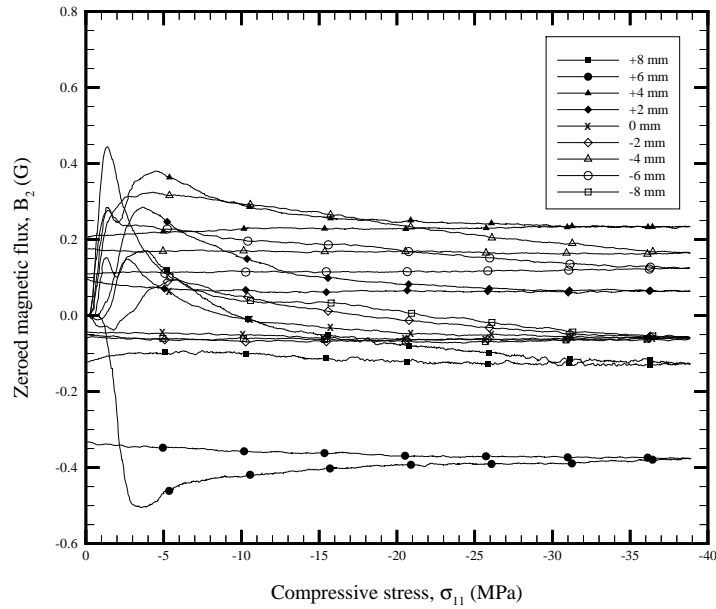
Figure A.4: Zeroed magnetic flux, B_2, over the gage length of pure Terfenol-D specimen, annealing flux of -800 G in 1–direction applied before testing at each position.
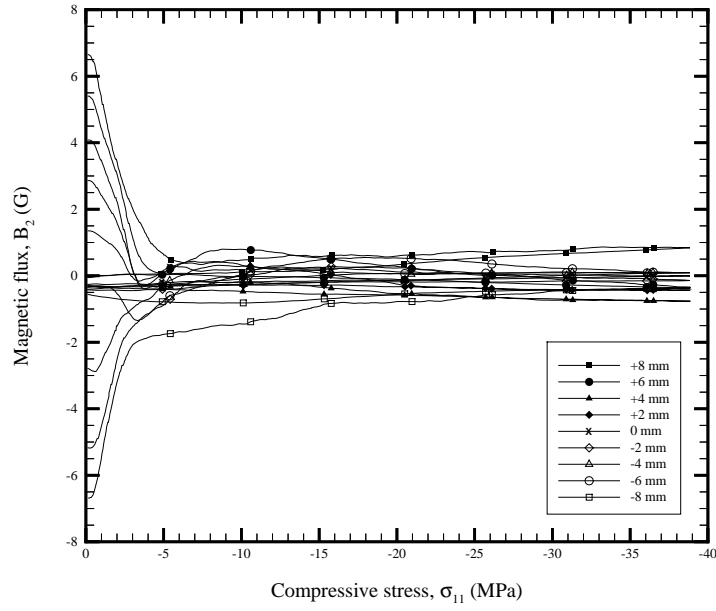
Figure A.5: Magnetic flux, B_2, over the gage length of pure Terfenol-D specimen, annealing flux of -800 G in 1–direction applied before testing at each position.
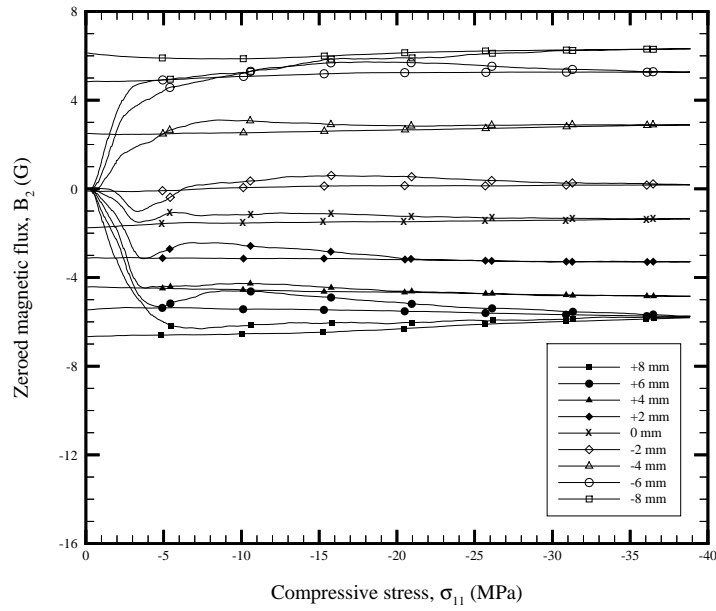
Figure A.6: Zeroed magnetic flux, B_2, over the gage length of pure Terfenol-D specimen, annealing flux of -800 G in 1–direction applied before testing at each position.
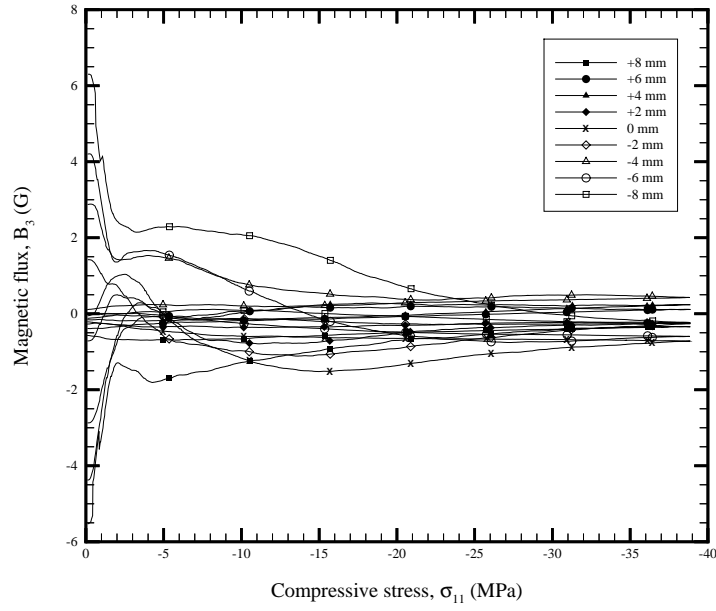
Figure A.7: Magnetic flux, B_3, over the gage length of pure Terfenol-D specimen, annealing flux of -800 G in 1–direction applied before testing at each position.

Figure A.8: Zeroed magnetic flux, B_3, over the gage length of pure Terfenol-D specimen, annealing flux of -800 G in 1–direction applied before testing at each position.
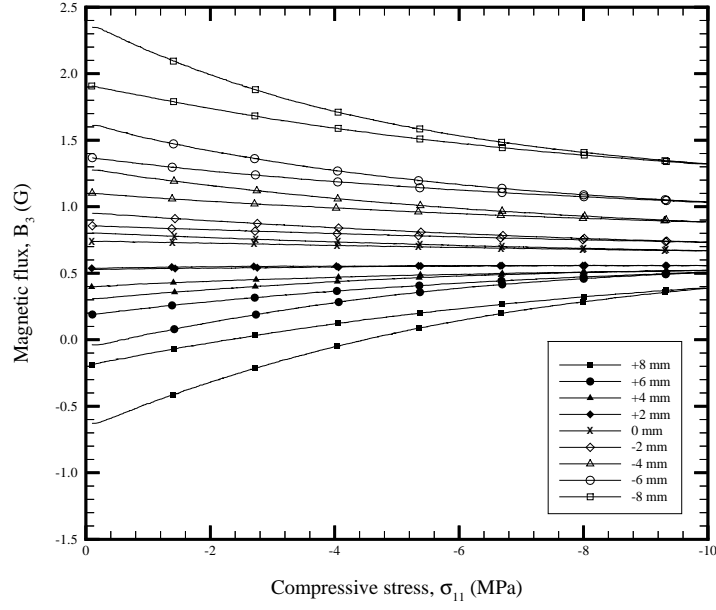
Figure A.9: Magnetic flux, B_1, over the gage length of $(1,1,1)$ Terfenol-D composite specimen, curing flux of -800 G, and annealing flux of -800 G applied before testing at each position.
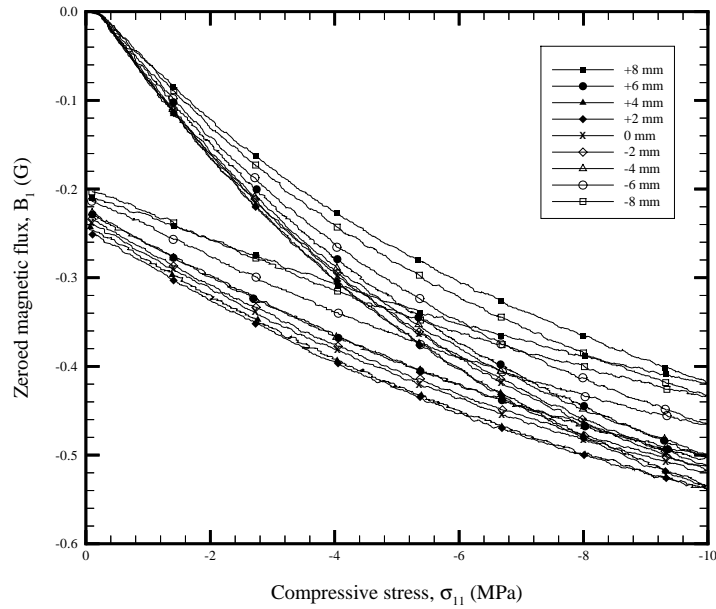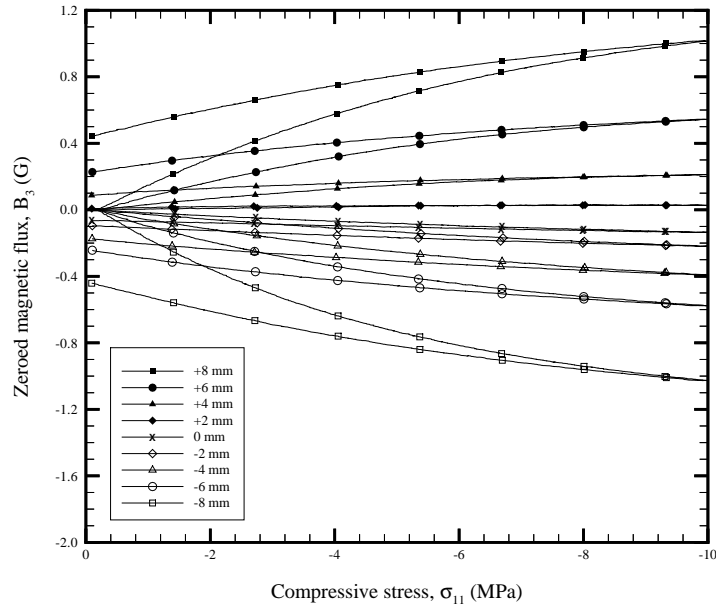

Figure A.10: Zeroed magnetic flux, B_1, over the gage length of $(1,1,1)$ Terfenol-D composite specimen, curing flux of -800 G, and annealing flux of -800 G applied before testing at each position.
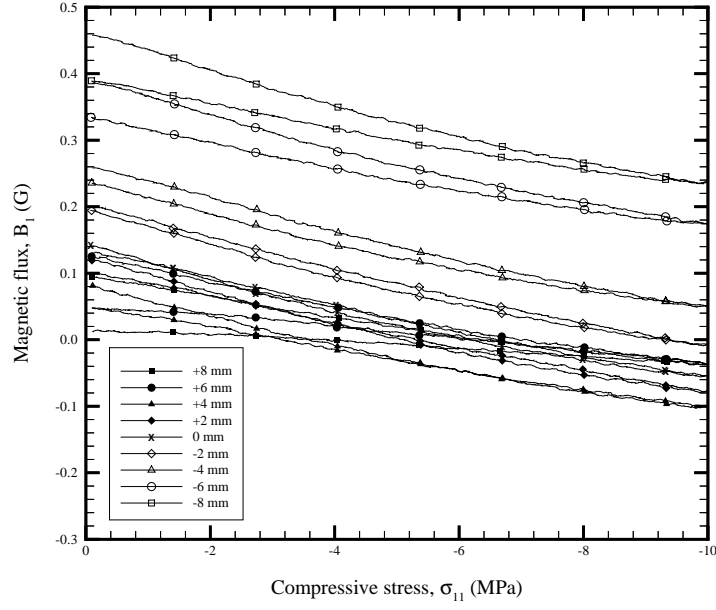
111
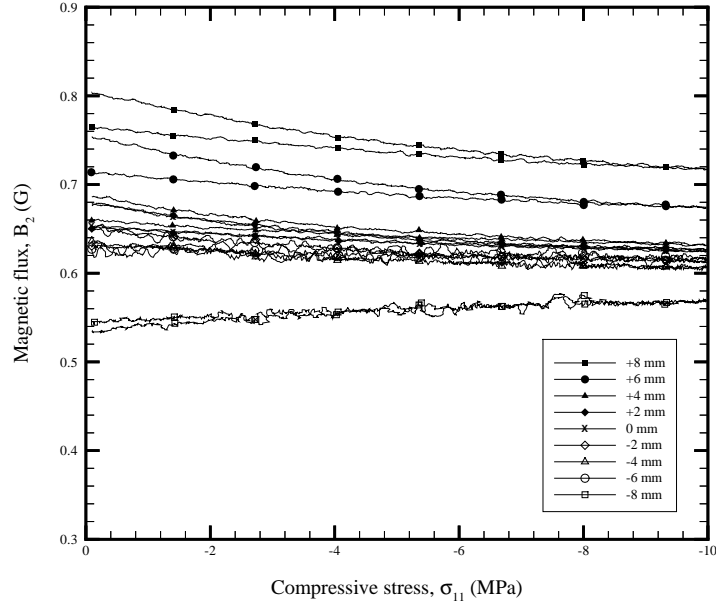
Figure A.11: Magnetic flux, B_2, over the gage length of (1,1,1) Terfenol-D composite specimen, curing flux of -800 G, and annealing flux of -800 G applied before testing at each position.
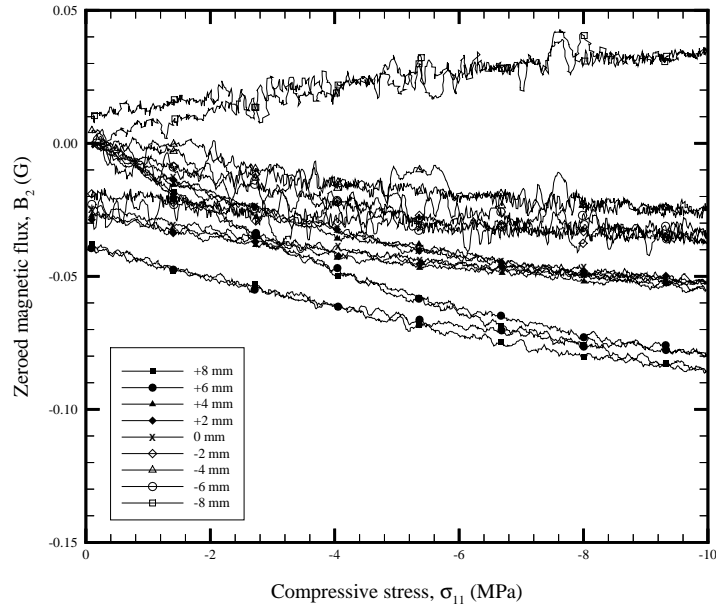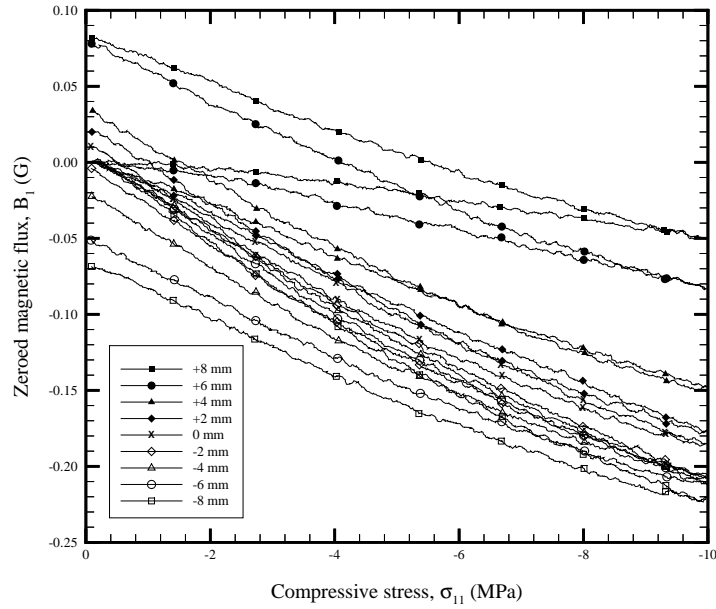

Figure A.12: Zeroed magnetic flux, B_2, over the gage length of (1,1,1) Terfenol-D composite specimen, curing flux of -800 G, and annealing flux of -800 G applied before testing at each position.
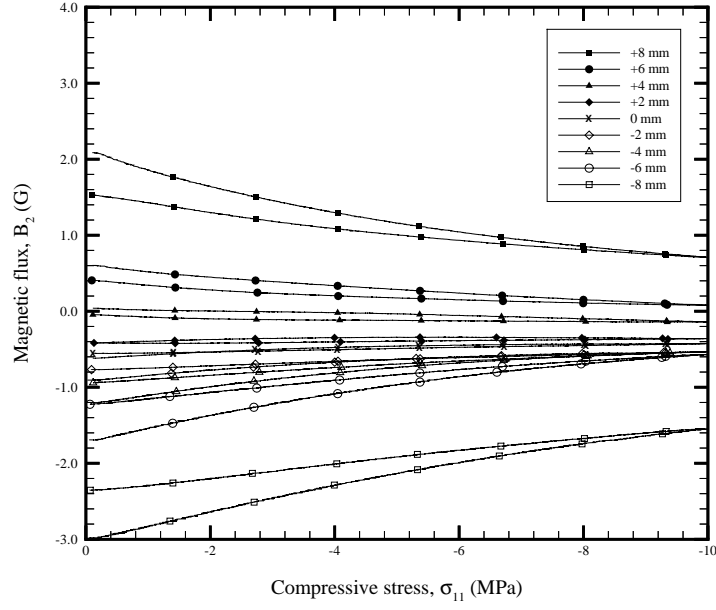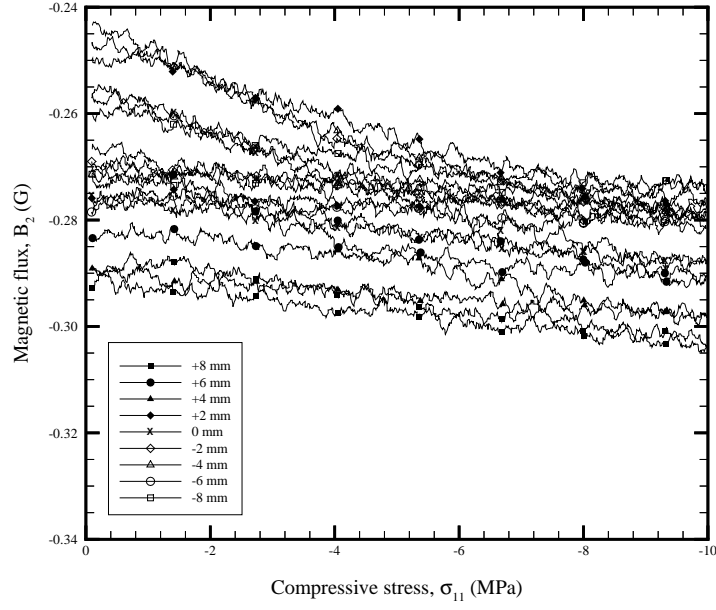
Figure A.13: Magnetic flux, B_2, over the gage length on the side face of $(1,1,1)$ Terfenol-D composite specimen, curing flux of -800 G, and annealing flux of -800 G applied before testing at each position.
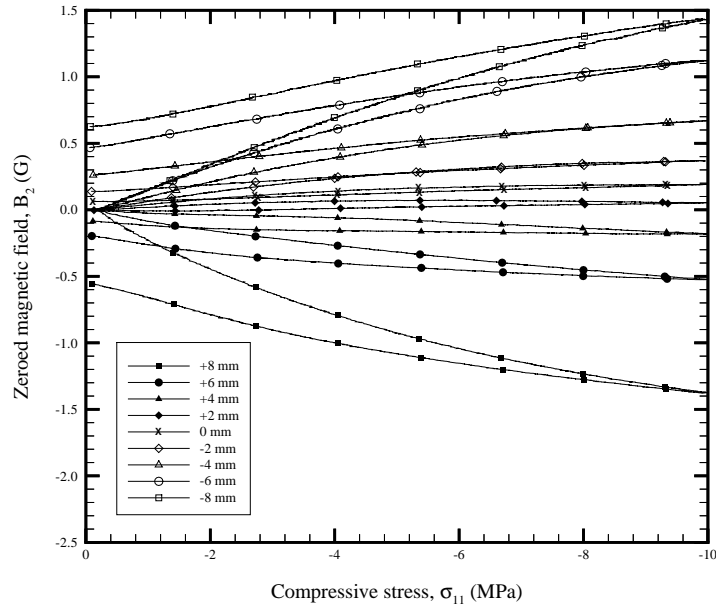
Figure A.14: Zeroed magnetic flux, B_2, over the gage length on the side face of $(1,1,1)$ Terfenol-D composite specimen, curing flux of -800 G, and annealing flux of -800 G applied before testing at each position.

Figure A.15: Magnetic flux, B_3, over the gage length of (1,1,1) Terfenol-D composite specimen, curing flux of -800 G, and annealing flux of -800 G applied before testing at each position.
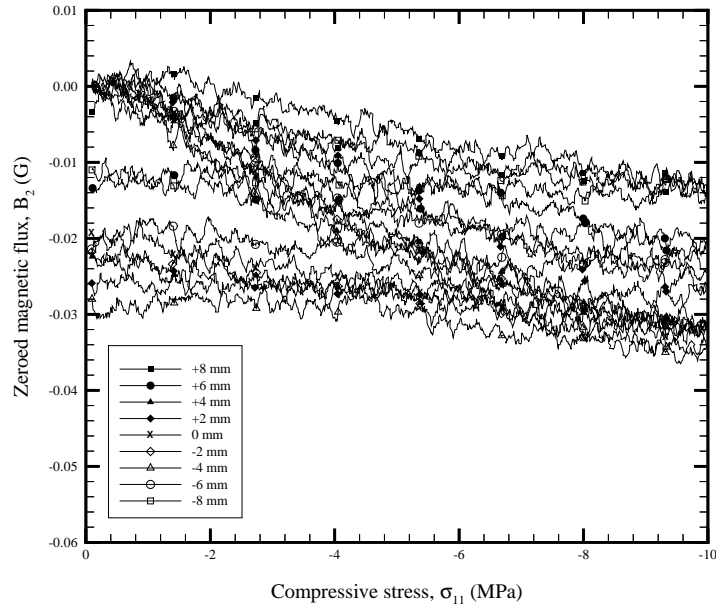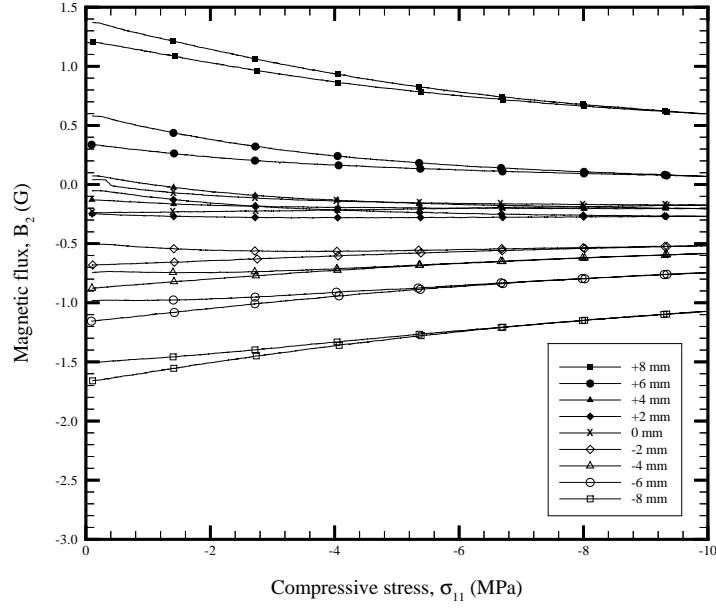

Figure A.16: Zeroed magnetic flux, B_3, over the gage length of (1,1,1) Terfenol-D composite specimen, curing flux of -800 G, and annealing flux of -800 G applied before testing at each position.

114

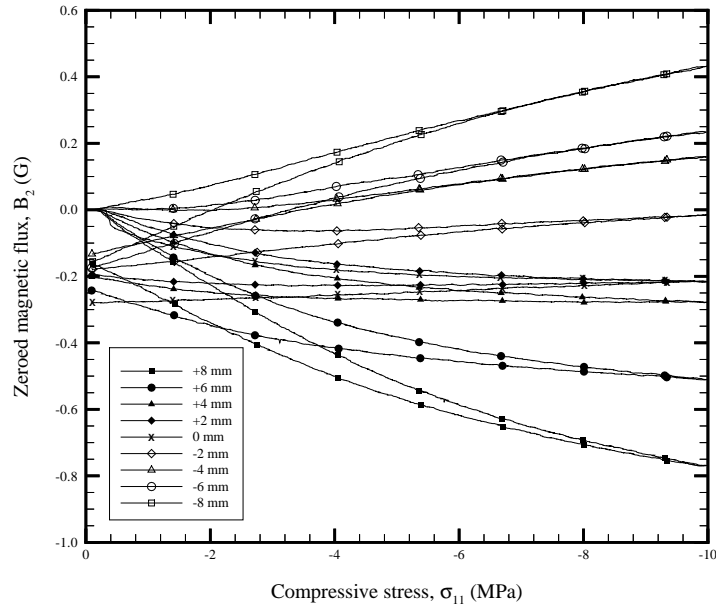Figure A.17: Magnetic flux, B_1, over the gage length of (1,3,1) Terfenol-D composite specimen, curing flux of -800 G, and annealing flux of -800 G applied before testing at each position.

Figure A.18: Zeroed magnetic flux, B_1, over the gage length of (1,3,1) Terfenol-D composite specimen, curing flux of -800 G, and annealing flux of -800 G applied before testing at each position.
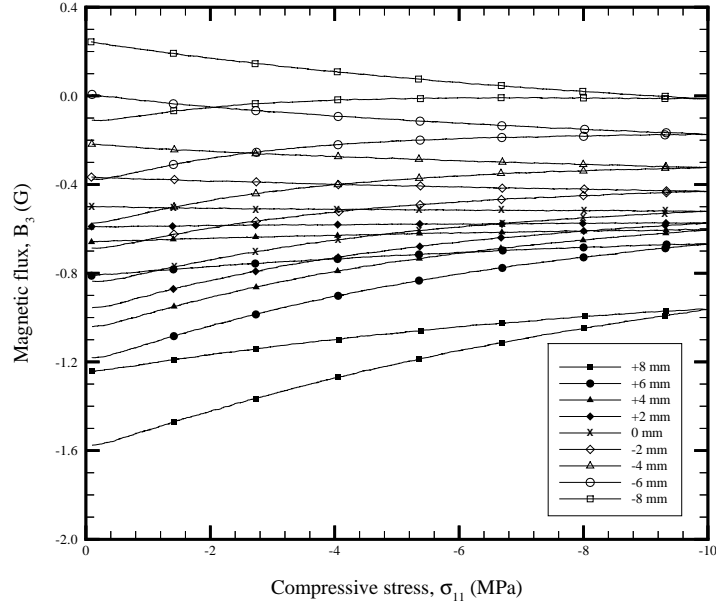
115

Figure A.19: Magnetic flux, B_2, over the gage length of (1,3,1) Terfenol-D composite specimen, curing flux of -800 G, and annealing flux of -800 G applied before testing at each position.
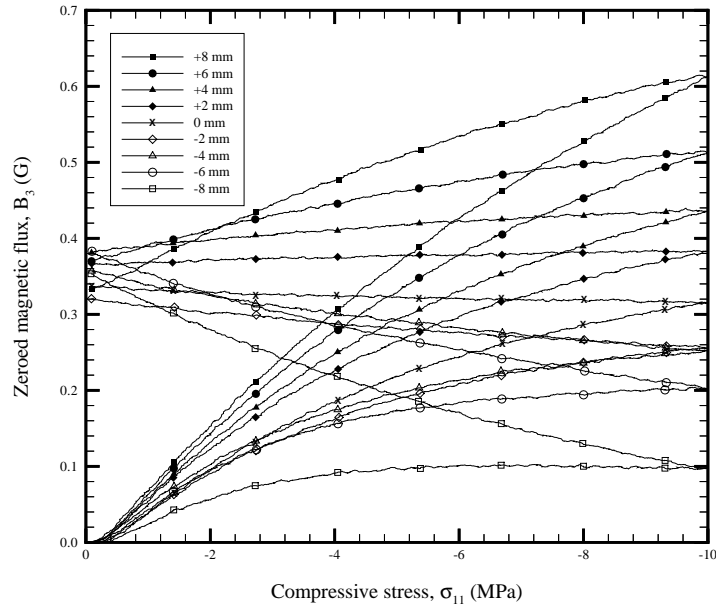

Figure A.20: Zeroed magnetic flux, B_2, over the gage length of (1,3,1) Terfenol-D composite specimen, curing flux of -800 G, and annealing flux of -800 G applied before testing at each position.

Figure A.21: Magnetic flux, B_2, over the gage length on the side face of (1,3,1) Terfenol-D composite specimen, curing flux of -800 G, and annealing flux of -800 G applied before testing at each position.

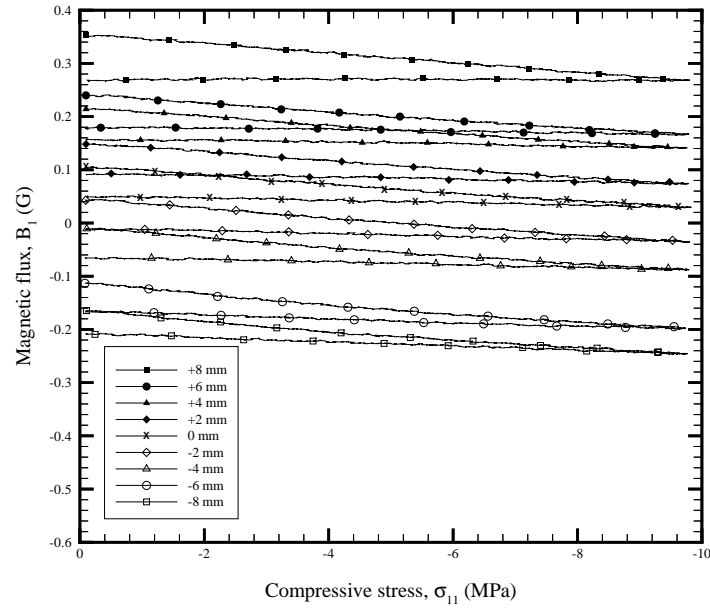Figure A.22: Zeroed magnetic flux, B_2, over the gage length on the side face of (1,3,1) Terfenol-D composite specimen, curing flux of -800 G, and annealing flux of -800 G applied before testing at each position.

117

Figure A.23: Magnetic flux, B_3, over the gage length of (1,3,1) Terfenol-D composite specimen, curing flux of -800 G, and annealing flux of -800 G applied before testing at each position.
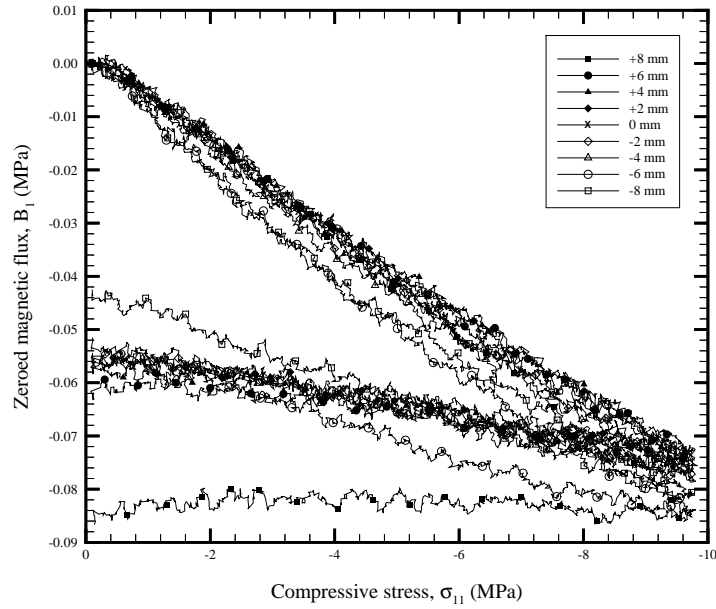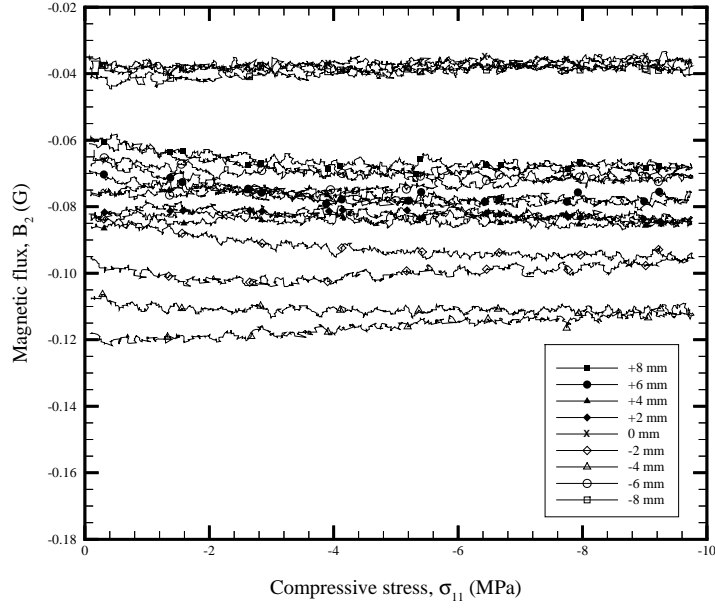

Figure A.24: Zeroed magnetic flux, B_3, over the gage length of (1,3,1) Terfenol-D composite specimen, curing flux of -800 G, and annealing flux of -800 G applied before testing at each position.

Figure A.25: Magnetic flux, B_1, over the gage length of (3,1,1) Terfenol-D composite specimen, curing flux of -800 G, and annealing flux of -800 G applied before testing at each position.
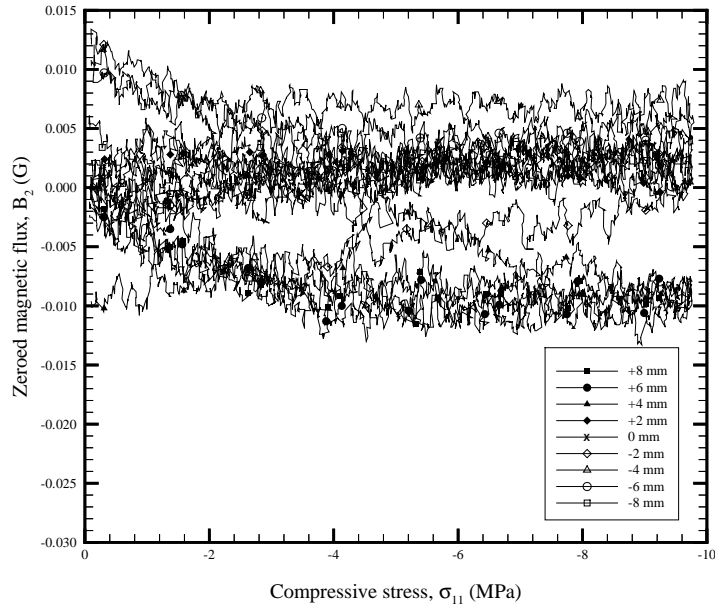

Figure A.26: Zeroed magnetic flux, B_1, over the gage length of (3,1,1) Terfenol-D composite specimen, curing flux of -800 G, and annealing flux of -800 G applied before testing at each position.
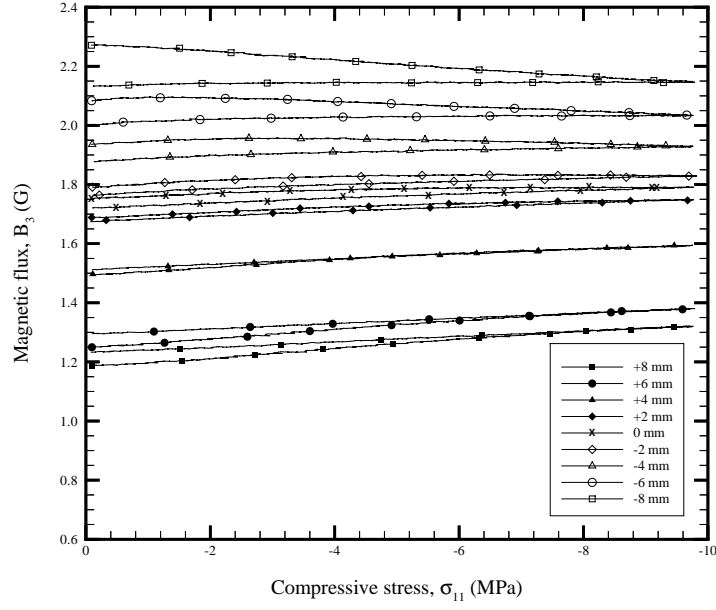
119

Figure A.27: Magnetic flux, B_2, over the gage length of (3,1,1) Terfenol-D composite specimen, curing flux of -800 G, and annealing flux of -800 G applied before testing at each position.

Figure A.28: Zeroed magnetic flux, B_2, over the gage length of (3,1,1) Terfenol-D composite specimen, curing flux of -800 G, and annealing flux of -800 G applied before testing at each position.
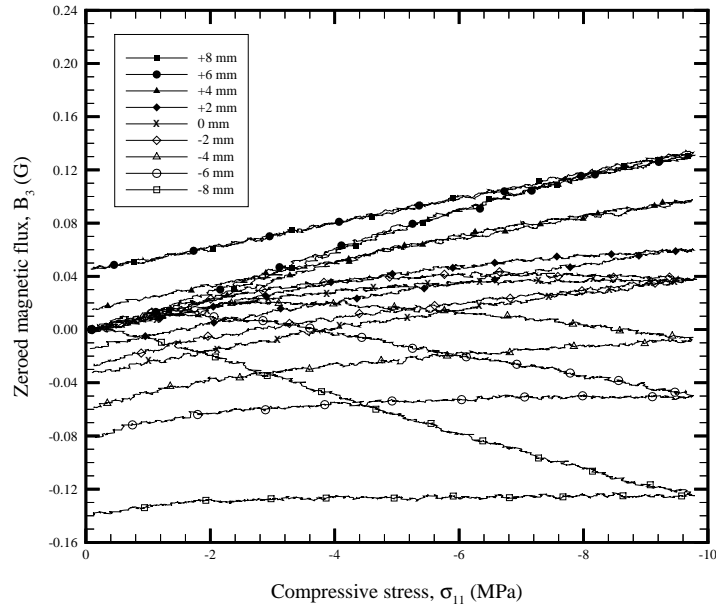
Figure A.29: Magnetic flux, B_3, over the gage length of (3,1,1) Terfenol-D composite specimen, curing flux of -800 G, and annealing flux of -800 G applied before testing at each position.
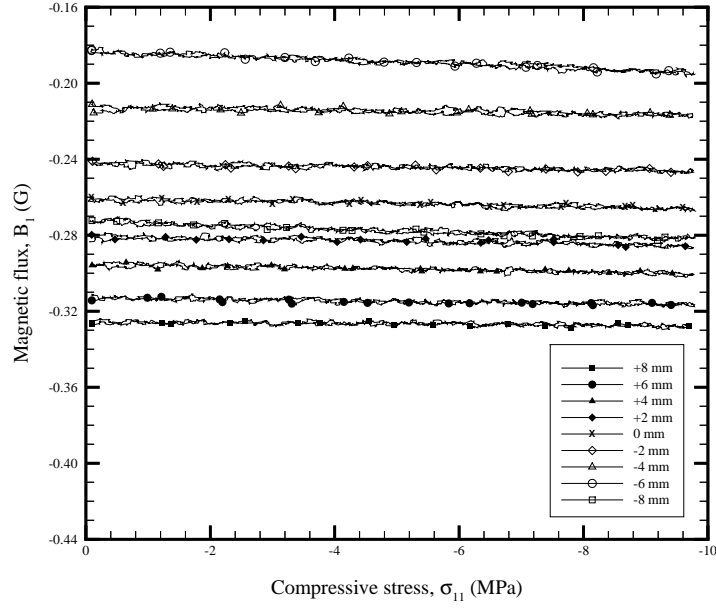

Figure A.30: Zeroed magnetic flux, B_3, over the gage length of (3,1,1) Terfenol-D composite specimen, curing flux of -800 G, and annealing flux of -800 G applied before testing at each position.

Figure A.31: Magnetic flux, B_1, over the gage length of (3,2,1) Terfenol-D composite specimen, curing flux of -800 G, and annealing flux of -800 G applied before testing at each position.
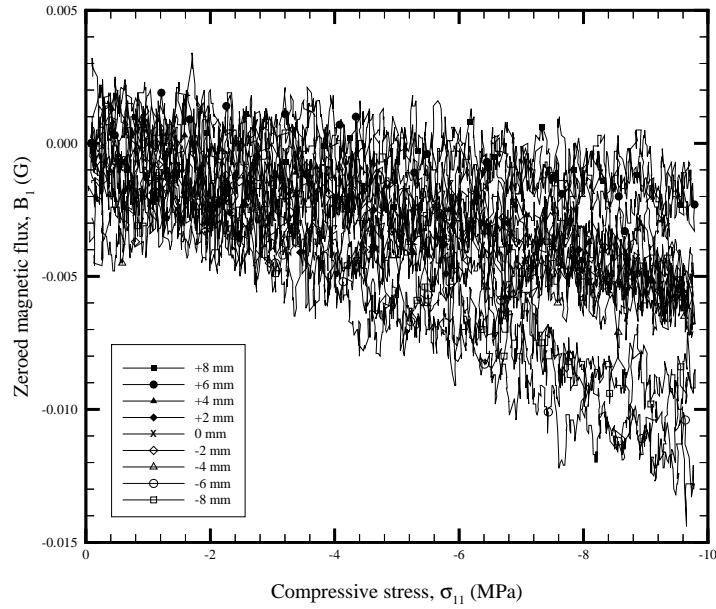

Figure A.32: Zeroed magnetic flux, B_1, over the gage length of (3,2,1) Terfenol-D composite specimen, curing flux of -800 G, and annealing flux of -800 G applied before testing at each position.
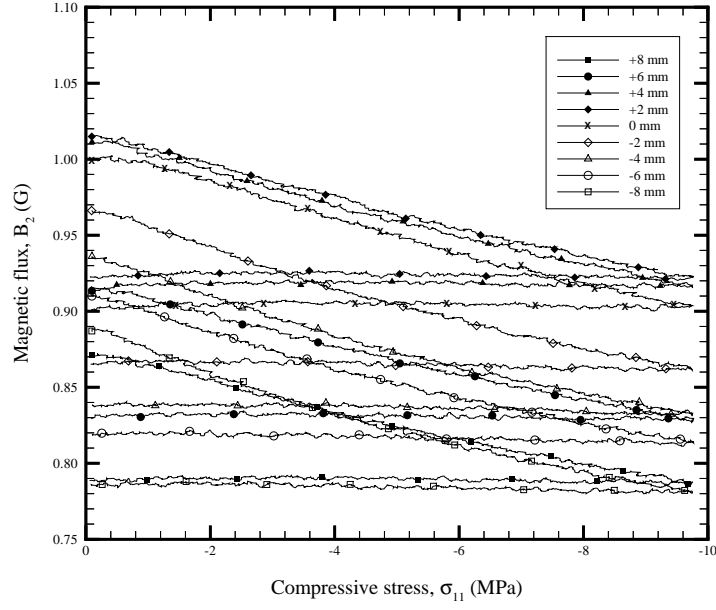
Figure A.33: Magnetic flux, B_2, over the gage length of (3,2,1) Terfenol-D composite specimen, curing flux of -800 G, and annealing flux of -800 G applied before testing at each position.
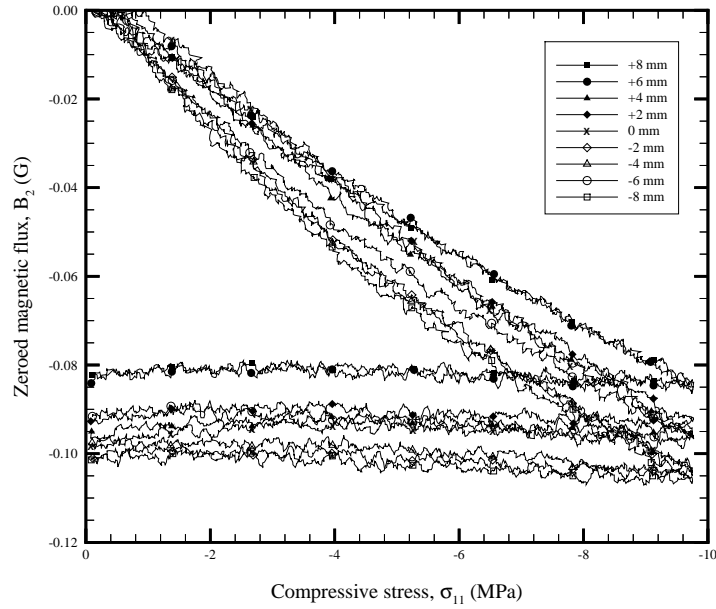

Figure A.34: Zeroed magnetic flux, B_2, over the gage length of (3,2,1) Terfenol-D composite specimen, curing flux of -800 G, and annealing flux of -800 G applied before testing at each position.

123

Figure A.35: Magnetic flux, B_3, over the gage length of (3,2,1) Terfenol-D composite specimen, curing flux of -800 G, and annealing flux of -800 G applied before testing at each position.
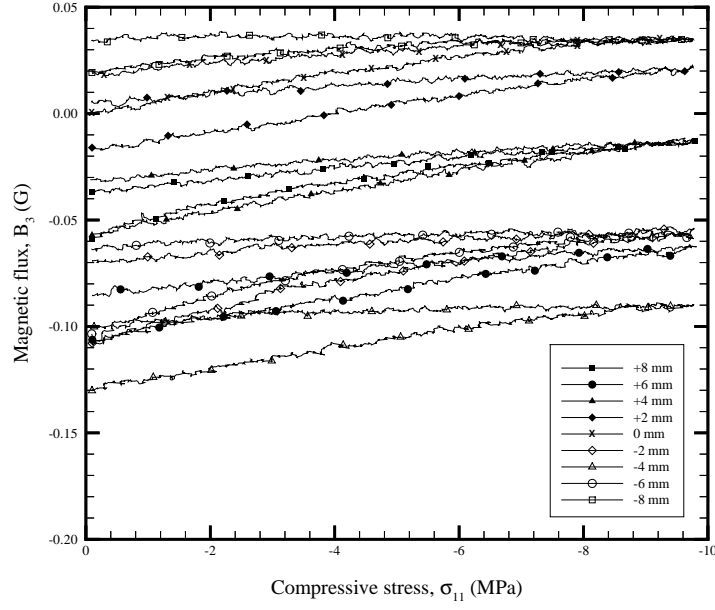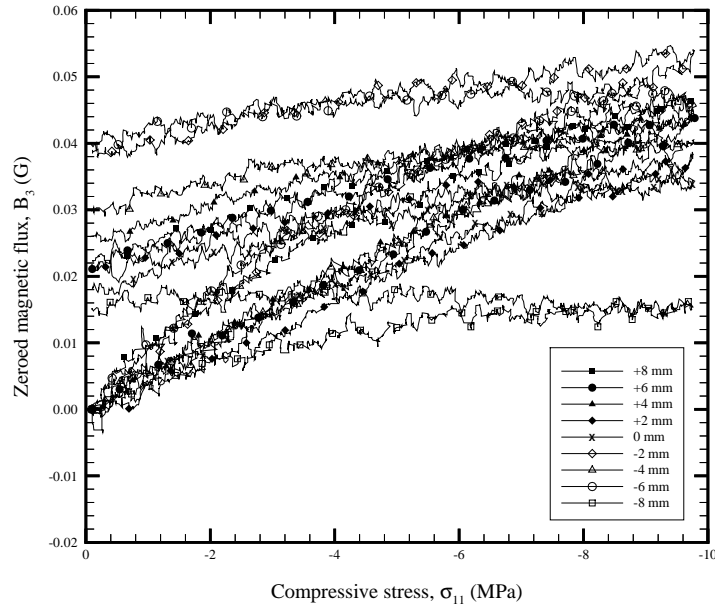

Figure A.36: Zeroed magnetic flux, B_3, over the gage length of (3,2,1) Terfenol-D composite specimen, curing flux of -800 G, and annealing flux of -800 G applied before testing at each position.
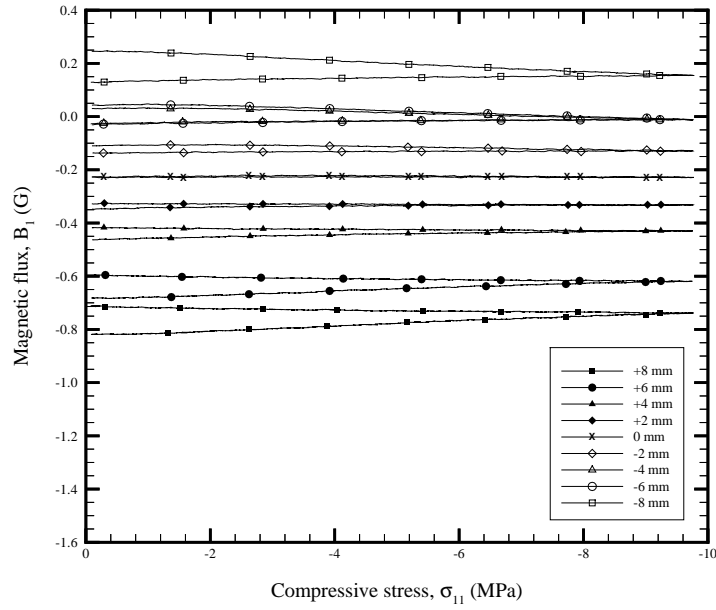
Figure A.37: Magnetic flux, B_1, over the gage length of (3,3,1) Terfenol-D composite specimen, curing flux of -800 G, and annealing flux of -800 G applied before testing at each position.

Figure A.38: Zeroed magnetic flux, B_1, over the gage length of (3,3,1) Terfenol-D composite specimen, curing flux of -800 G, and annealing flux of -800 G applied before testing at each position.

Figure A.39: Magnetic flux, B_2, over the gage length of (3,3,1) Terfenol-D composite specimen, curing flux of -800 G, and annealing flux of -800 G applied before testing at each position.
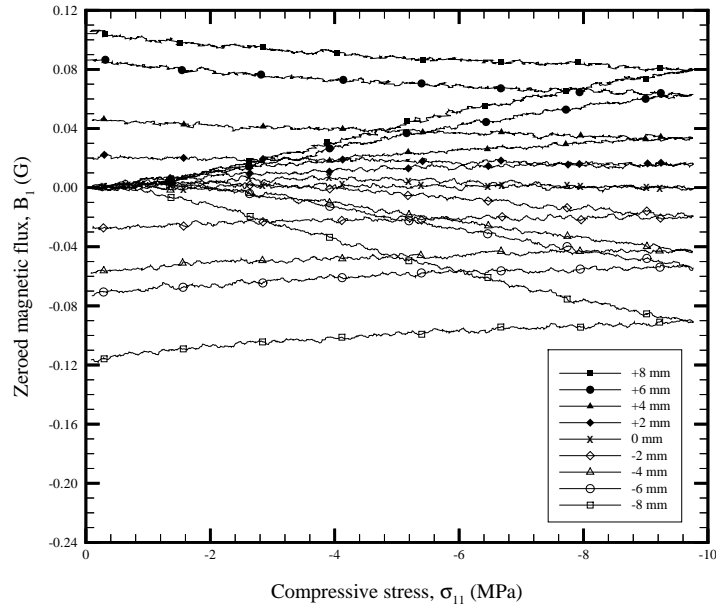

Figure A.40: Zeroed magnetic flux, B_2, over the gage length of (3,3,1) Terfenol-D composite specimen, curing flux of -800 G, and annealing flux of -800 G applied before testing at each position.
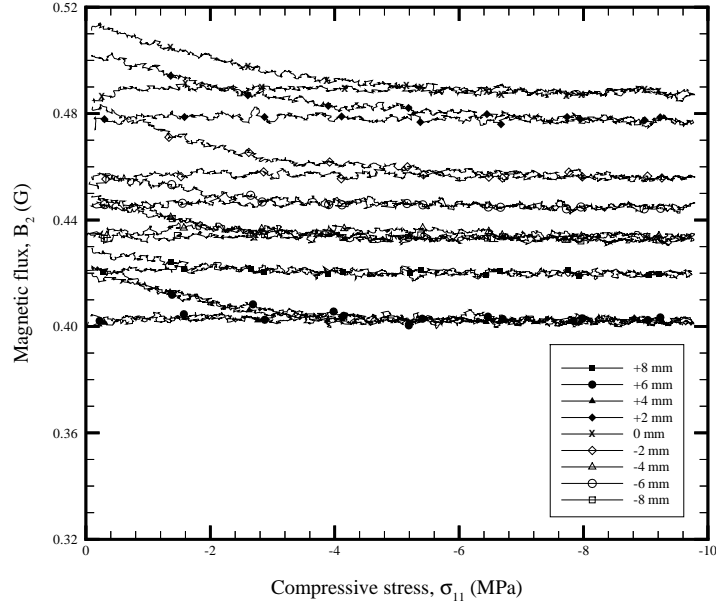
Figure A.41: Magnetic flux, B_3, over the gage length of (3,3,1) Terfenol-D composite specimen, curing flux of -800 G, and annealing flux of -800 G applied before testing at each position.

Figure A.42: Zeroed magnetic flux, B_3, over the gage length of (3,3,1) Terfenol-D composite specimen, curing flux of -800 G, and annealing flux of -800 G applied before testing at each position.
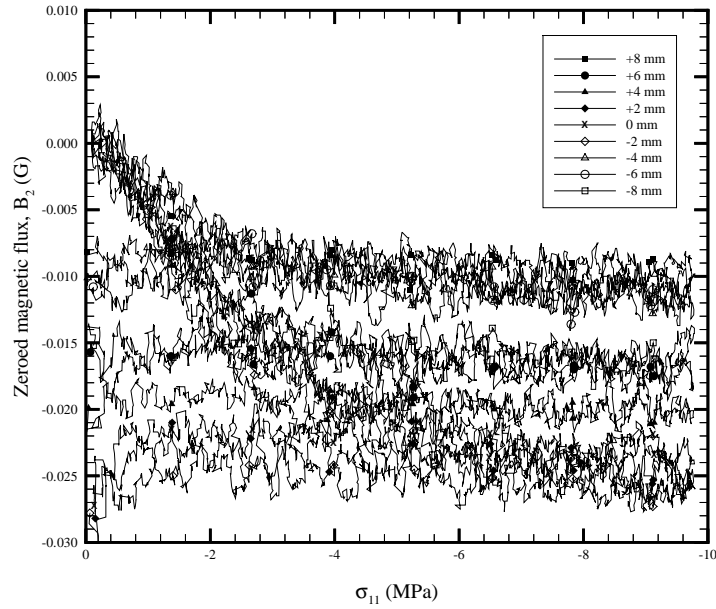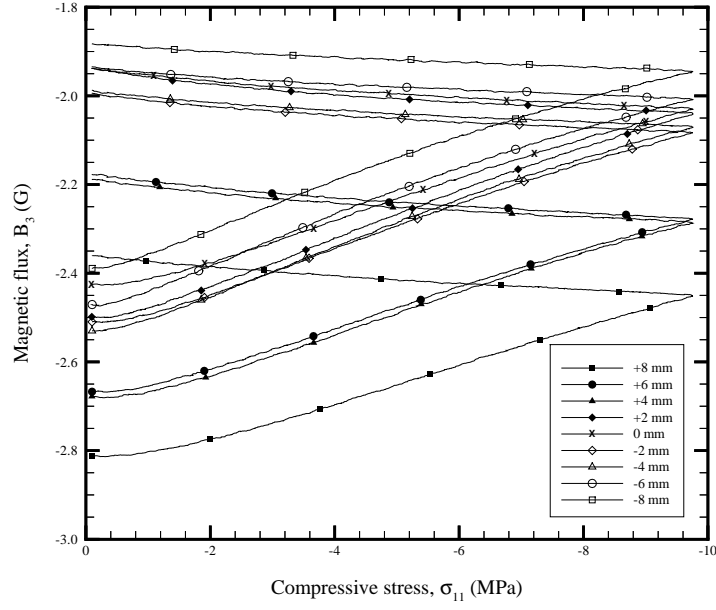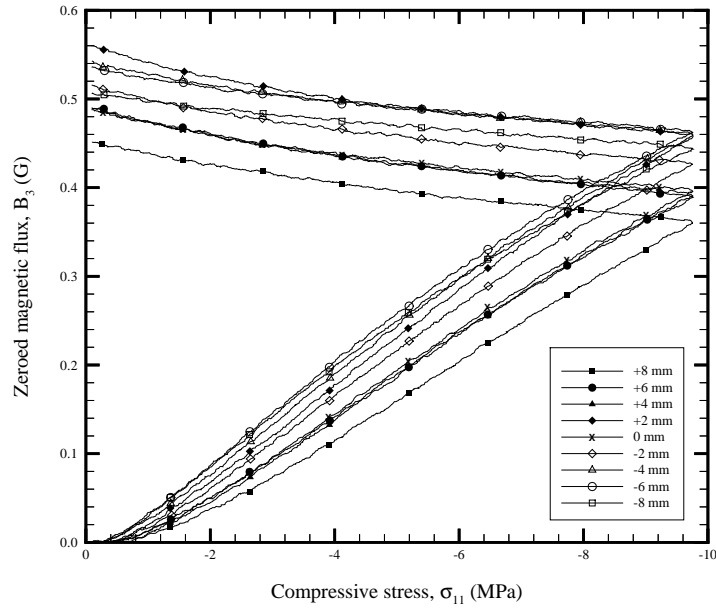
Appendix B

Cyclic testing results

Figure B.1: Cyclic magnetic response, B_1, of (1,1,1) Terfenol-D composite specimen, curing flux of -800 G, and annealing flux of -800 G applied before first cycle only.

Figure B.2: Cyclic magnetic response, B_1, of (1,1,1) Terfenol-D composite specimen, curing flux of -800 G, and annealing flux of -800 G applied before first cycle only.

Figure B.3: Cyclic magnetic response, B_1, of (1,1,1) Terfenol-D composite specimen, curing flux of -800 G, and annealing flux of -2600 G applied before first cycle only.

Figure B.4: Cyclic magnetic response, B_1, of (1,1,1) Terfenol-D composite specimen, curing flux of -800 G, and annealing flux of -2600 G applied before first cycle only.
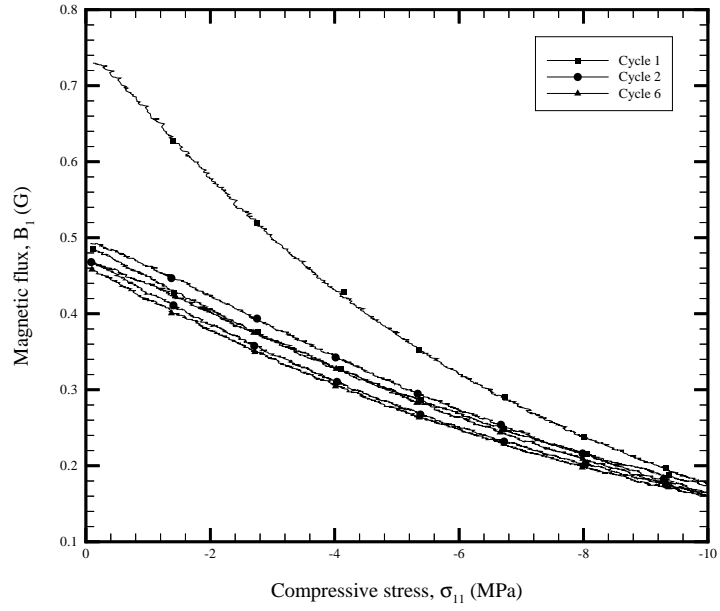
130

Figure B.5: Cyclic magnetic response, B_1, of $(1,1,1)$ Terfenol-D composite specimen, curing flux of -2600 G, and annealing flux of -800 G applied before first cycle only.
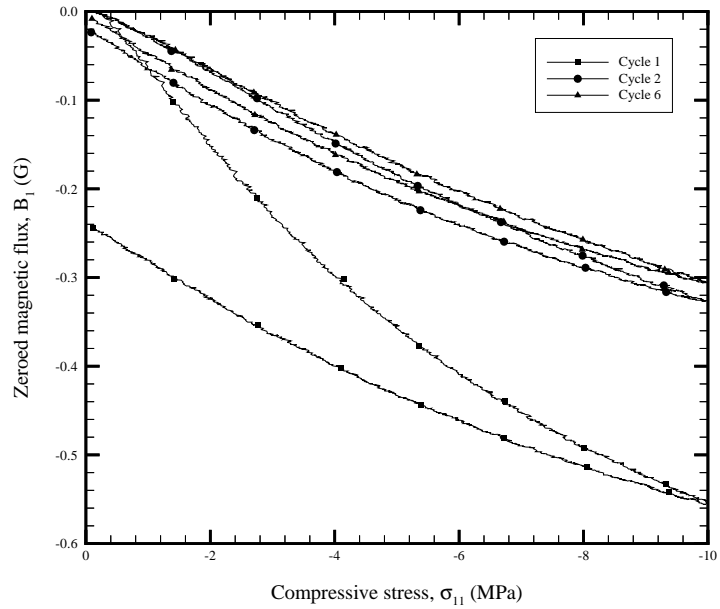

Figure B.6: Cyclic magnetic response, B_1, of $(1,1,1)$ Terfenol-D composite specimen, curing flux of -2600 G, and annealing flux of -800 G applied before first cycle only.
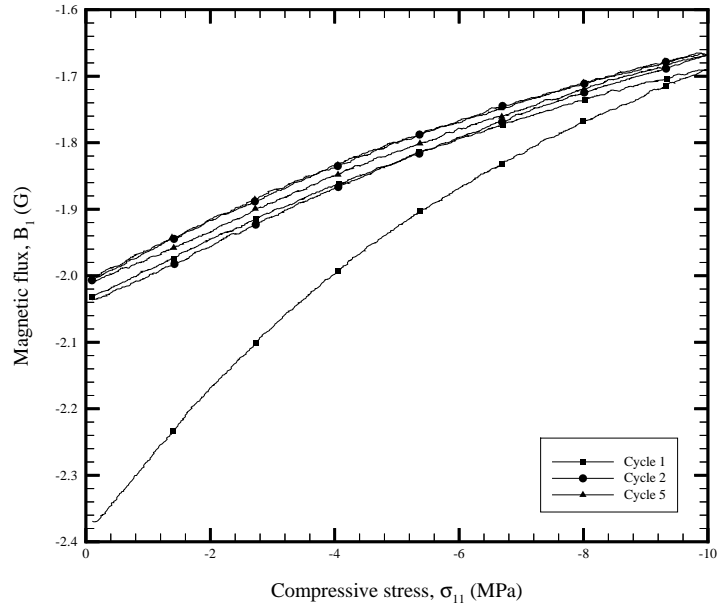
131

Figure B.7: Cyclic magnetic response, B_1, of (1,1,1) Terfenol-D composite specimen, curing flux of -2600 G, and annealing flux of -2600 G applied before first cycle only.
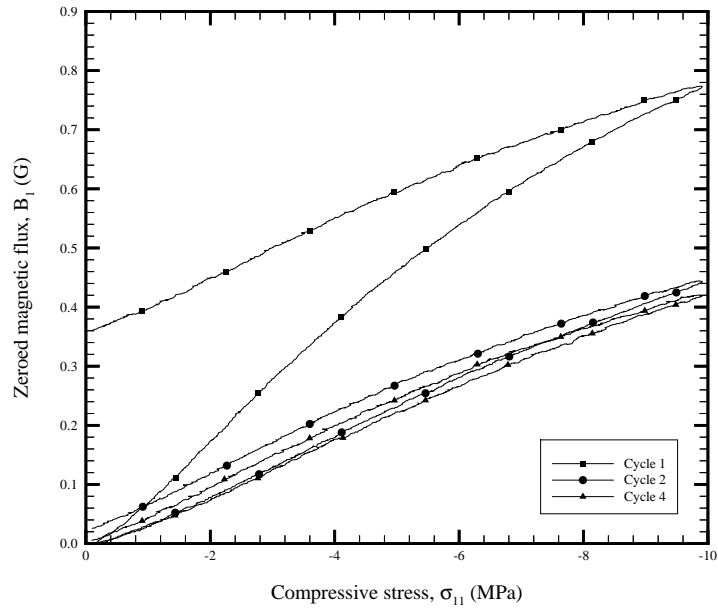
Figure B.8: Cyclic magnetic response, B_1, of (1,1,1) Terfenol-D composite specimen, curing flux of -2600 G, and annealing flux of -2600 G applied before first cycle only.
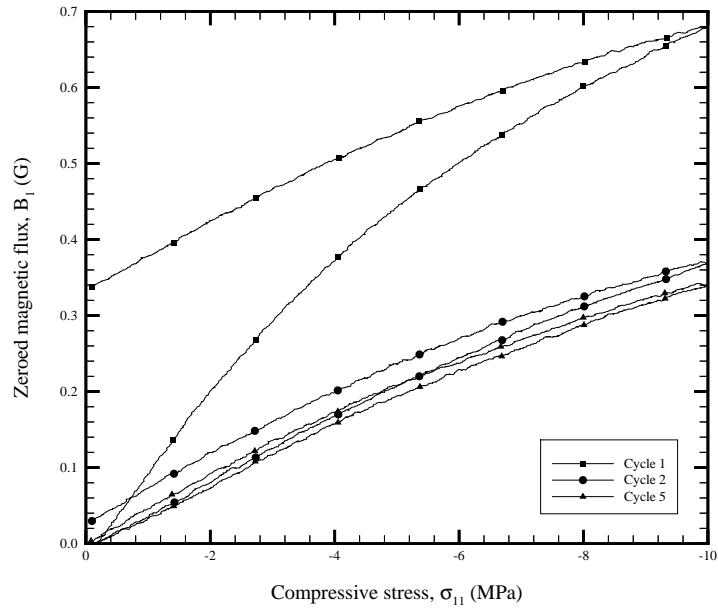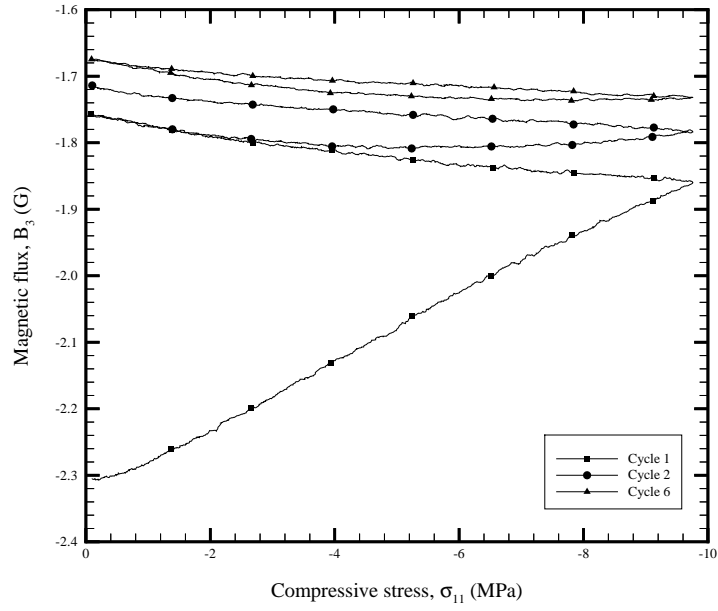
Figure B.9: Cyclic magnetic response, B_3, of (3,3,1) Terfenol-D composite specimen, curing flux of -800 G, and annealing flux of -800 G applied before first cycle only.
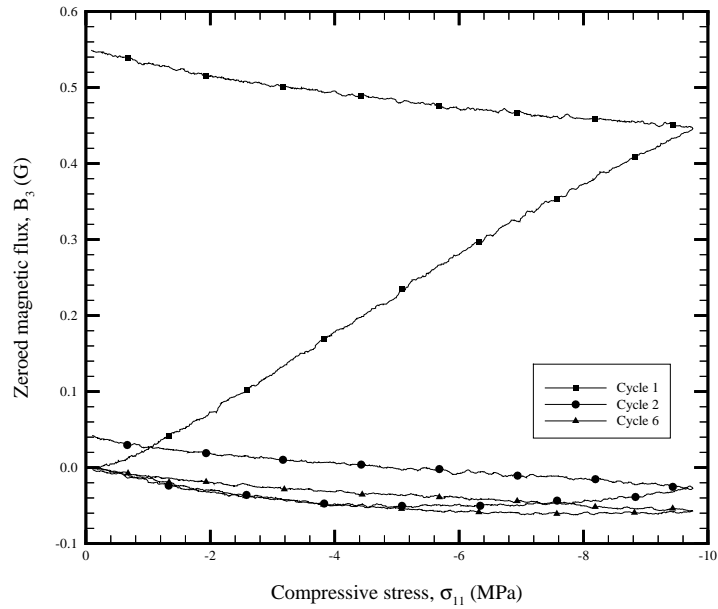
Figure B.10: Cyclic magnetic response, B_3, of (3,3,1) Terfenol-D composite specimen, curing flux of -800 G, and annealing flux of -800 G applied before first cycle only.
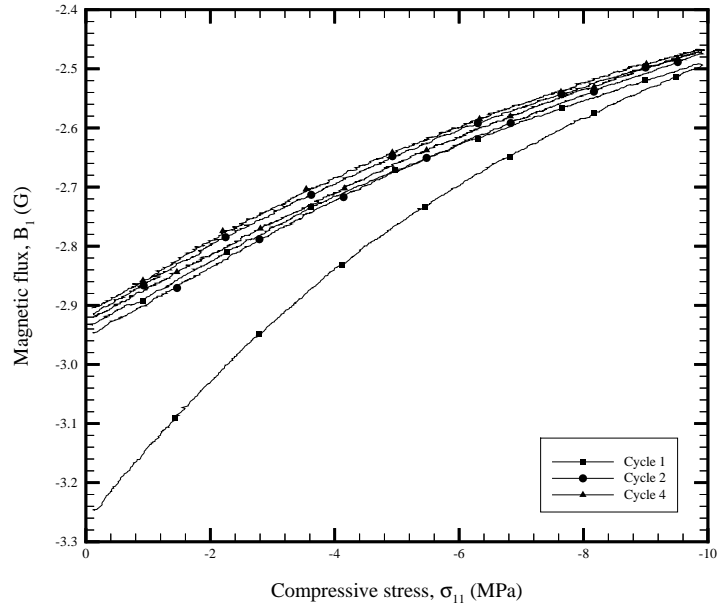
133
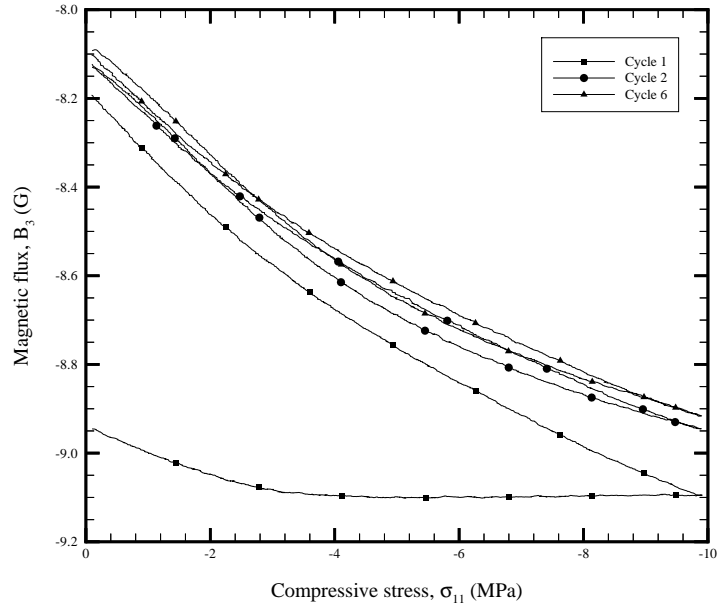
Figure B.11: Cyclic magnetic response, B_3, of (3,3,1) Terfenol-D composite specimen, curing flux of -2600 G, and annealing flux of -800 G applied before first cycle only.
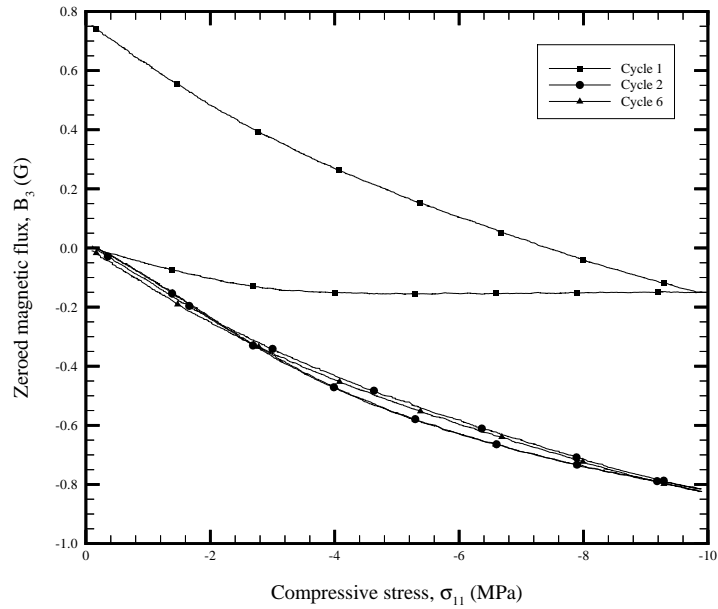
Figure B.12: Cyclic magnetic response, B_3, of (3,3,1) Terfenol-D composite specimen, curing flux of -2600 G, and annealing flux of -800 G applied before first cycle only.
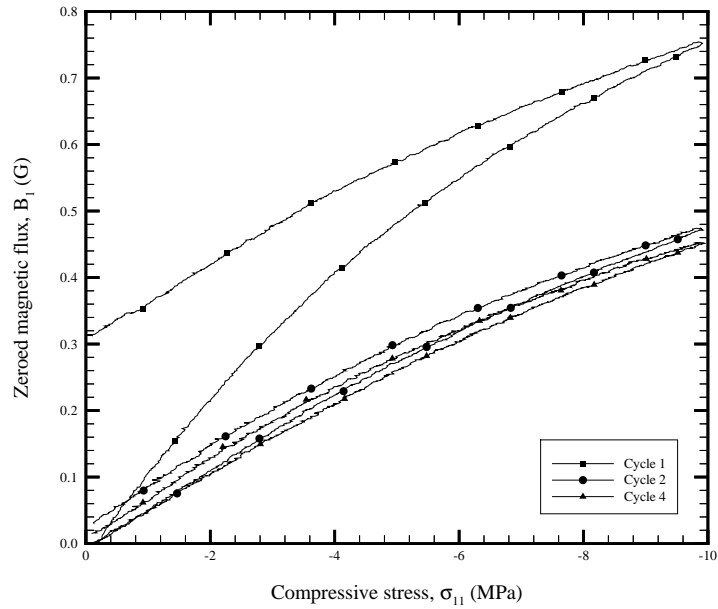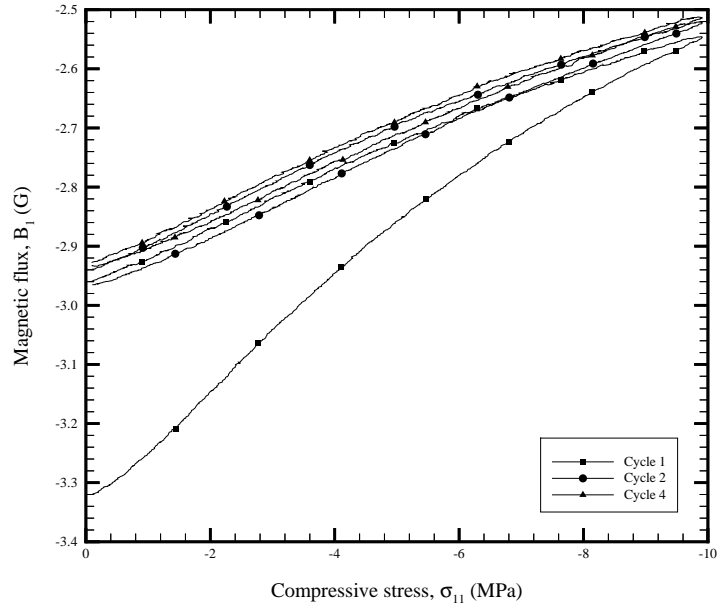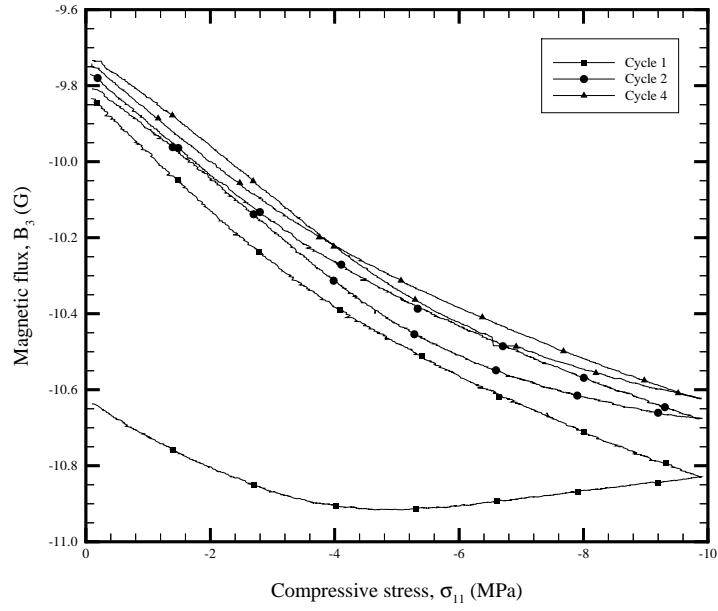
Figure B.13: Cyclic magnetic response, B_3, of (3,3,1) Terfenol-D composite specimen, curing flux of -2600 G, and annealing flux of -2600 G applied before first cycle only.
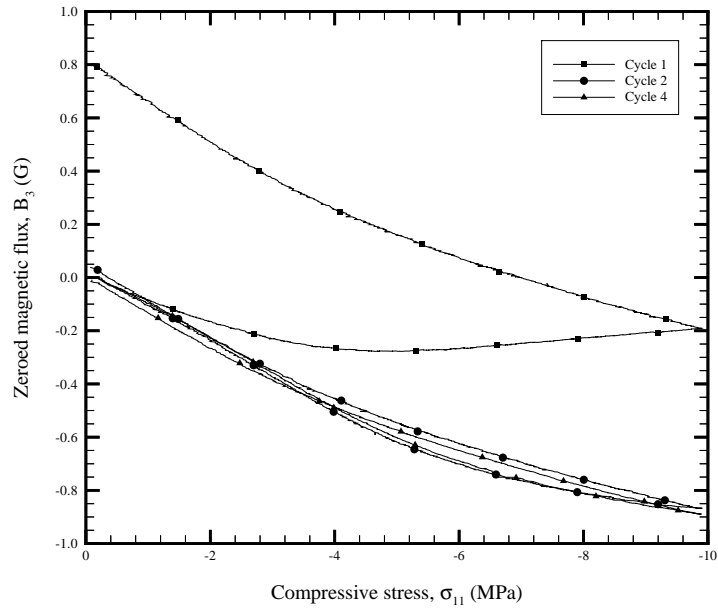
Figure B.14: Cyclic magnetic response, B_3, of (3,3,1) Terfenol-D composite specimen, curing flux of -2600 G, and annealing flux of -2600 G applied before first cycle only.

Appendix C

Sample input file for FEA

```
*HEADING, SPARSE
**
*NODE
      1,   0.000102848,              0.
      2,         0.0001,              0.
(remaining node list omitted)
**
**
*ELEMENT, TYPE=CAX8E, ELSET=ROD
   3601,   14789,   14626,   14621,   14784,   14790,   14627,
   14785,   14791
   3602,   14626,   14462,   14457,   14621,   14625,   14463,
   14619,   14627
(remaining element list omitted)
**
**
**
*ELEMENT, TYPE=CAX8E, ELSET=MATRIX
      1,       2,       3,     167,     166,       1,       5,
     165,       4
      2,     166,     167,     331,     330,     165,     275,
     329,     274
(remaining element list omitted)
**
**
**
** chain
**
*SOLID SECTION,
ELSET=CHAIN, MATERIAL=TERFENOL
         1.,
**
** matrix
**
*SOLID SECTION, ELSET=MATRIX, MATERIAL=POLYMER
         1.,
**
**
```

```
*MATERIAL, NAME=POLYMER
**
*ELASTIC, TYPE=ISO
     3.8E+9,        0.33
**
*PIEZOELECTRIC, TYPE=E
0.,0.,0.,0.,0.,0.,0.,0.,
0.,0.,0.,0.,0.,0.,0.,0.,
0.,0.
**
*DIELECTRIC, TYPE=ISO
12.56E-7
**
**
**
*MATERIAL, NAME=TERFENOL
**
*ELASTIC, TYPE=ISO
     5.E+10,        0.444
**
**
*PIEZOELECTRIC, TYPE=E
0.,0.,0.,0.74E-10,0.,0.,-0.74E-10,1.48E-10,
-0.74E-10,0.,0.,0.,0.,0.,0.,0.,
0.,0.74E-10
**
*DIELECTRIC, TYPE=ISO
6.28E-6
**
**
** noxdisp
**
*BOUNDARY, OP=NEW
      85, 1,,          0.
     220, 1,,          0.
(remaining nodes and boundary conditions omitted)
**
** potential
**
*BOUNDARY, OP=NEW
POTENTIA, 9,,          0.
**
** Step  1, Default Static Step
** LoadCase, Default
**
*STEP, AMPLITUDE=RAMP, PERTURBATION
Linear Static Analysis
** This load case is the default load case that always appears
**
*STATIC
**
*NSET, NSET=POTENTIA
        1,        2,        3,        6,        7,        9,       10,       12,
```

```
(remaining node set omitted)
**
**
*ELSET, ELSET=COMPRESS
        1,        91,       181,       271,       361,       451,       541,       631,
(remaining element set omitted)
**
**
** compress
**
*DLOAD, OP=NEW COMPRESS,
P1,        1.E+7
**
*RESTART, WRITE
**
*END STEP
```

References

[1] A. Bienkowski. The possibility of utilizing the magnetomechanical Villari effect in ferrite as stress transducer. *Journal of Magnetism and Magnetic Materials*, 83:411–412, 1990.

[2] F. Brouwers. Magnetostrictive tagging of composite materials for the purpose of structural health monitoring. Master's thesis, Department of Aeronautical and Astronautical Engineering, University of Illinois at Urbana-Champaign, 1998.

[3] T. Christman, A. Needleman, and S. Suresh. An experimental and numerical study of deformation in metal-ceramic composites. *Acta Metallurgica*, 37(11):3029–3050, 1989.

[4] A. E. Clark. Magnetostrictive rare earth-Fe_2 compounds. Chapter 7. In *Ferromagnetic Materials, Vol. 1,* ed., by, E., P., Wohlfarth, 1980.

[5] A. E. Clark, J. P. Teter, and O. D. McMasters. Magnetostriction "jumps" in twinned $Tb_{0.3}Dy_{0.7}Fe_{1.9}$. *Journal of Applied Physics*, 63(8):3910–3912, 1988.

[6] I. M. Daniel and O. Ishai. *Engineering mechanics of composite materials.* Oxford University Press, New York, 1994.

[7] M. J. Dapino, F. T. Calkins, A. B. Flatau, and D. L. Hall. Measured Terfenol-D material properties under varied applied magnetic field levels. In *Proceedings of SPIE Symposium on Smart Structures and Materials*, volume 2717, pages 697–708, 1996.

[8] M. Goodfriend. Material breakthrough spurs actuator design. *Machine Design*, 63(6):147–150, 1991.

[9] R. D. Greenough and M. Schulze. AC losses in grain oriented $Tb_{0.3}Dy_{0.7}Fe_{1.95}$. *IEEE Transactions on Magnetics*, 26(5):2586–2588, 1990.

[10] D. J. Griffiths. *Introduction to Electrodynamics*. Prentice-Hall, Englewood Cliffs, NJ, 2nd. edition, 1989.

[11] K. B. Hathaway and A. E. Clark. Magnetostrictive materials. *MRS Bulletin* (Materials Research Society), pages 34–41, April 1993.

[12] C. Hsueh and P. F. Becher. Residual thermal stresses in ceramic composites. Part I: with ellipsoidal inclusions. *Materials Science and Engineering*, A212:22–28, 1996.

[13] J. Hudson, S. C. Busbridge, and A. R. Piercy. Magnetomechanical coupling and elastic moduli of polymer-bonded Terfenol composites. *Journal of Applied Physics*, 83(11):7255–7257, 1998.

[14] D. C. Jiles. The development of highly magnetostrictive rare earth-iron alloys. *Journal of Physics D: Applied Physics*, 27:1–11, 1994.

[15] M. R. Jolly, J. D. Carlson, B. C. Munoz, and T. A. Bullions. The magnetoviscoelastic response of elastomer composites consisting of ferrous particles embedded in a polymer matrix. *Journal of Intelligent Material Systems and Structures*, 7:613–622, November 1996.

[16] B. Jones and C. Liang. Magnetostriction: revealing the unknown. *IEEE AES Systems Magazine*, 3-6, March 1996.

[17] J. Kaleta, S. Tumanski, and J. Zebracki. Magnetoresistors as a tool for invesitgating the mechanical properties of ferromagnetic materials. *Journal of Magnetism and Magnetic Materials*, 160:199–200, 1996.

[18] J. Kaleta and J. Zebracki. Application of the Villari effect in a fatigue examination of nickel. *Fatigue and Fracture of Engineering Materials and Structures*, 19(12):1435–1443, 1996.

[19] K. S. Kannan and A. Dasgupta. Finite element modeling of multi-functional composites with embedded magnetostrictive devices. *Adaptive Structures and Composite Materials: Analysis and Application*, AD-Vol. 45/MD-Vol.54:21–28, 1994.

[20] M. B. Moffett, A. E. Clark, M. Wun-Fogle, J. Linberg, J. P. Teter, and E. A. McLaughlin. Characterization of Terfenol-D for magnetostrictive transducers. *Journal of the Acoustical Society of America*, 89(3):1448–1455, 1991.

[21] C. J. Murray. Magnetostrictive rods aid transducer, actuator design. *Design News*, pages 140–141, June 1988.

[22] Institute of Electrical and Electronics Engineers. IEEE standard on magnetostrictive materials. (IEEE Std. 319-1990), 1990.

[23] Institutute of Electrical and Electronics Engineers. IEEE standard on piezoelectricity. (IEEE Std. 176-1978), 1978.

[24] M. Pan, D. J. Green, and J. R. Hellmann. Residual stress in composites with coated particles. *Journal of Composite Materials*, 31(10):1046–1059, 1997.

[25] F. E. Pinkerton, T. W. Capehart, J. F. Herbst, E. G. Brewer, and C. B. Murphy. Magnetostrictive $SmFe_2$/metal composites. *Applied Physics Letters*, 70(19):2601–2603, 1997.

[26] E. M. Purcell. *Electricity and magnetism*. McGraw-Hill Publishing Company, New York, 1985.

[27] R. Quattrone, J. Berman, and S. R. White. Self-monitoring structures containing magnetostrictive composites. In *Proceedings from the 21st Army Science Conference*, pages 21–26, Norfolk, VA, June 15-17 1998.

[28] F. Rodriguez. *Principles of Polymer Systems*. Hemisphere Publishing Corporation, Washington, 1982.

[29] C. A. Rogers, S. W. Zhou, and Z. Chaudhry. An embedded particle tagging tecnique for in-field non-destructive evaluation. Technical report, USACERL, November 1994.

[30] L. Sandlund, M. Fahlander, T. Cedell, A. E. Clark, J. B. Restorff, and M. Wun-Fogle. Magnetostriction, elastic moduli, and coupling factors of composite Terfenol-D. *Journal of Applied Physics*, 75(10):5656–5658, 1994.

[31] M. A. Stone, I. F. Schwartz, and H. D. Chandler. Residual stresses associated with post-cure shrinkage in GRP tubes. *Composites Science and Technology*, 57(1):47–54, 1997.

[32] E. Tremolet de Lacheisserie. *Magnetostriction: theory and applications of magnetoelasticity*. CRC Press, Inc., Boca Raton, FL, 1993.

[33] S. R. White. Health monitoring and repair of smart composite materials. In *Proceedings of the First Korea-U.S. Workshop on Composite Materials*, pages 1–11, Seoul, Korea, Sept. 7-11 1998. Seoul National University.

[34] S. R. White and Y. K. Kim. Process-induced residual stress analysis of AS4/3501-6 composite material. *Mechanics of Composite Materials and Structures*, 5:153–186, 1998.

[35] S. R. White, J. Li, and J. Hommema. Smart materials for infrastructure applications. Technical report, USACERL Contract No. DACA88-97-K-0001/P00001, December 1998.

[36] S.R. White and R.G. Albers. Magnetostrictive tagging of composite materials for structural health monitoring. Technical report, USACERL Contract No. DACA88-95-D-0004-01, February 1996.

143